Investigation into Time-of-Flight Detectors for Use with LYCCA at FAIR

Lianne Marie Scruton

A thesis submitted for the degree of

Doctor of Philosophy

University of York

Department of Physics

June 2013

Abstract

The LYCCA (Lund-York-Cologne-CAlorimeter) array is a core device in the upcoming HISPEC (High-resolution In-beam SPECtroscopy) campaign that will take place at the FAIR (Facility for Anti-Proton and Ion Research) facility. LYCCA consists of a number of position, energy and timing detectors that aim to track and uniquely identify the fragments generated after the secondary target. Two time-of-flight options are currently proposed for LYCCA, fast plastic scintillators and large-area diamond detectors, both of which have shown to possess excellent timing properties. This thesis presents an in-depth analysis into the performance of LYCCA-0, and uses data from the first LYCCA commissioning experiment to directly compare the two timing options in order to determine which option is best for future LYCCA experiments. This thesis also focuses upon the development of the large-area diamond timing option, and in particular, establishes whether it is feasible to create a large-area detector whilst still maintaining the good timing resolution observed for smaller area detectors.

The developmental work was undertaken in the form of two optimisation experiments. An initial timing resolution of 103 ps was achieved from the first of these experiments, whilst the second experiment demonstrated that increasing the diamond detector's capacitance lengthens the rise time of the current signal from the detector, causing the timing resolution to deteriorate. Analysis of the commissioning experiment showed that LYCCA was able to uniquely identify the fragments after the secondary target using the fast plastic scintillator timing option, and a timing resolution of 51 ps was obtained for each scintillator. The diamond detector option performed less well, achieving a timing resolution of 193 ps. This poor resolution is attributed, amongst other reasons, to parasitic capacitances generated by long cables present between the detector and the preamplifiers. As it would be difficult to eliminate these long cables without a considerable re-design of the signal processing arrangements for LYCCA, it has been decided that the ToF measurements for the final LYCCA device should be undertaken using the fast plastic scintillators [1].

For my parents, Ann and Bob ...

Contents

List of Figures

List of Tables

Acknowledgements

Firstly, I would like to thank my supervisor, Prof Mike "Bling"Bentley for all of the help, advice and praise he has given throughout my PhD and in the years before when I was just a mere undergraduate. His guidance has been invaluable, and without him, this thesis would not exist. Thanks Mike, it's been a laugh!

I would also like to thank Nara Singh for all of the help he provided during the first few years of my PhD, especially during much of the analysis presented in this thesis. When it comes to the GSI analysis, I must also thank my LYCCA collaborators, such as Robert and Edana, who wrote the new code for the PreSPEC campaign, as well as other collaborators such as Dirk, Pavel, Andreas and Jan who helped us bring the LYCCA-0 array together for the commissioning experiment.

I am also very grateful of the help I have received from both Annika Lohstroh and Fabio Schirru from the University of Surrey. Annika was always there to (cheerily) answer my many questions about diamond, and Fabio's fabrication skills were instrumental in this project.

Back in York, there are a great number of other people I wish to thank for making the time I have spent in the Nuclear Group fun and (surprisingly) productive. Thank you to Christian, whose stats course forced me to learn ROOT, and to Paul for sorting me out when what I thought I'd learnt about ROOT turned out to be wrong. I must also thank my fellow students, both past and present, for the advice and banter they have given to me in the past three and three-quarter years, especially Jack for looking over my thesis for me, as well as Phil and James for answering many of my questions over the years. To all of you, I have just one thing to say: Pub?

Finally, I must say the biggest thank you to those I care about the most, my parents and my fiancé Steve. My mum and dad's endless support and encouragement is the reason that I am where I am today and for that, I am forever grateful, thank you. I also want to thank Steve for knowing just what to say to me when I got stressed or annoyed during my PhD, you've been amazing.

Declaration

This thesis has been submitted for the degree of Doctor of Philosophy in accordance with the regulations of the University of York. The work presented in this thesis has not been sumitted for any other degree or qualification. I declare that the work here is my own, and where other sources of information have been used, they are clearly marked and referenced.

CHAPTER 1

Introduction

Ion beam technology at fragmentation facilities has advanced tremendously over recent years, and with this advancement comes the ability to produce more exotic nuclei and further probe current nuclear models at the extremes of existence. The promise of more intense and higher purity beams is very encouraging, however it could be redundant if the technology required to identify the many nuclei produced in the fragmentation reactions fails to keep up with the beam line advancements.

Each nucleus of interest often has to be clearly distinguished from other nuclei of similar mass if one is to be sure that the nuclear property being measured correlates to the desired nucleus. In some cases, this identification can be done using large spectrographs like the S800 at the National Superconducting Cyclotron Laboratory (NSCL) [2]. This spectrograph uses extremely large magnets to separate the different fragments in a beam and therefore requires a large amount of space. Unfortunately, very few ion beam facilities are able to accommodate such large equipment, and as a result, other means of identifying nuclei produced at the secondary target have to be developed. Reducing the distance over which the nuclei can be identified naturally increases the uncertainty on the measurement. To overcome this problem, it is essential that the detectors used to identify the nuclei are state of the art and are able to achieve high-resolution measurements.

One future facility that requires such high-resolution detectors for fragment identification is the Facility for Anti-proton and Ion Research (FAIR), which is currently

under construction at Gesellschaft für Schwerionenforschung (GSI) in Germany. The NUSTAR (NUclear Structure, Astrophysics and Reactions) collaboration plans to undertake a campaign of experiments, known as the HISPEC (High-resolution In-beam SPECtroscopy) project, which aims to use high-resolution gamma-ray spectroscopy to study the radical changes in nuclear structure that are predicted in extremely neutron or proton rich nuclei [3].

1.1 HISPEC

HISPEC is a natural continuation of the successful RISING (Rare ISotope INvestigations at GSI) campaign, which performed both in-beam and stopped-beam experiments with high-resolution gamma-ray spectroscopy using radioactive beams from the FRS (FRagment Separator) at GSI between 2003 and 2010 [4].

The in-beam experiments implemented within HISPEC will use energies of around 100 MeV/u, and provide information about the medium spin structure and transition probabilities of exotic nuclei, as well as the evolution of the shell structure such as the shell closure around N = Z = 50 and nuclear shapes of these nuclei [5].

HISPEC aims to answer fundamental questions such as where does the neutron-dripline lie? Do new forms of collective motion occur in nuclei far from stability? Are the symmetries seen in near-stable nuclei also present in nuclei close to the driplines?[6]. Single step Coulomb excitation and fragmentation reactions will be employed using thick (a few 100 mg/cm^2) targets to answer these fundamental questions, along with devices such as plungers for precise lifetime measurements, and a H_2 gas target for (p,p') experiments.

HISPEC, along with the DESPEC (Decay SPECtroscopy) project, will be located in the Low Energy Cave situated at the end of the low energy branch of the Super-FRS fragment separator at FAIR. This fragment separator is an upgrade to the FRS (FRagment Separator) that is currently in use at GSI, and aims to produce cleaner, more intense secondary beams and increase the transmission of fragments to experimental areas with the aid of superconducting coils [7]. The Super-FRS will be constructed over the next few years.

Gamma-ray spectroscopy during the HISPEC campaign will be undertaken using the next-generation Ge-detector array, AGATA (Advanced GAmma Tracking Array), which will surround the secondary target. The final AGATA array will be a 4π array, consisting of 180 high purity Ge crystals. Each crystal has 6-fold sector-wise segmentation, as well as 6-fold longitudinal segmentation, which allows

Compton scattering events that occur within the crystal to be tracked, and the full scattering path can be reconstructed. This results in high efficiency and a good spectral response from the detector [8].

The reaction products that are formed at, or after, the secondary target need to be tracked and identified on an event-by-event basis so that accurate information about their velocity, position and direction of travel can be used to complement the good-quality data from AGATA. This will be done using an array of position, energy and time-of-flight (ToF) detectors that make up the LYCCA (Lund-York-Cologne-CAlorimeter) array. LYCCA is required to uniquely identify light nuclei, $A \approx 20$ for energies up to 200 MeV/u, and heavier nuclei, up to $A = 200$ with energies of around 100 MeV/u. For nuclei above $A = 100$, it may be necessary to place LYCCA at the focal plane of a magnetic spectrometer so that the additional momentum dispersion provided by the spectrometer aids the particle identification [9].

It will also be possible to combine the HISPEC and DESPEC setups to perform recoil-decay tagging experiments. This technique requires the detection of prompt radiation at the secondary target, followed by the detection of the decay products by the DESPEC setup [10].

1.2 LYCCA

The design of LYCCA is based on that of CATE (CAlorimeter TElescope), a $\Delta E - E$ telescope that was used for charged-particle identification during the RISING campaign. CATE was designed to measure the charge, Z, of a particle through energy loss measurements in Double-Sided Silicon-Strip Detectors (DSSSDs) and determine the mass of the particle by measuring its residual energy in CsI crystals [11]. Unfortunately, energy straggling in the thick secondary targets led to uncertainties in the velocity of the charged particles, making unique mass measurements impossible [10]. The LYCCA design still uses both DSSSDs and CsI detectors for energy loss and residual energy measurements, but ToF detectors have also been introduced into the design to significantly reduce these velocity uncertainties.

ToF measurements are made between a start timing detector, placed just behind the secondary target, and a stop detector, placed immediately ahead of the DSSSD and CsI detectors approximately 4 m downstream of the target. The stop timing detector, DSSSDs and CsI detectors form a modular wall that can be arranged into a number of configurations to best suit the requirements of the experiment. This

wall shall be made up of 26 modules, each measuring 6 x 6 cm^2.

Two different types of timing detector were proposed to measure the ToF of particles through LYCCA, large-area polycrystalline diamond detectors and fast plastic scintillators. The fast plastic scintillators will use 32 photomultiplier tubes (PMTs) to simultaneously measure the scintillation light generated by a traversing particle and, as a result, are able to achieve excellent timing resolution. Difficulties may arise, however, when trying to produce modular plastic scintillators as part of the timing wall, as development tests have shown the best performing scintillators are currently circular [12]. The scintillators are also found to be rate limited.

The diamond detectors will be constructed using CVD (Chemical Vapour Deposition) polycrystalline diamond wafers. This material has shown to have excellent timing properties in the past, however, diamond detectors usually measure no more than 10 x 10 mm^2, and have never been implemented on the scale required for LYCCA. Using diamond detectors to make up the timing wall is therefore a challenging task and a large amount of developmental will be required to fabricate such large detectors whilst still ensuring that a good timing resolution can be achieved.

1.3 Scope of the Project

The developmental work behind the manufacture of large-area diamond detectors shall be presented in this thesis in the form of two optimisation experiments. This work will concentrate on testing and optimising the fast electronics to be used in conjunction with the diamond detectors, as well as studying how the material used to make the detector contacts, and the size of these contacts, affects the timing properties of the detector.

The first prototype of LYCCA, known as LYCCA-0, was commissioned in a campaign of experiments between September 2010 and May 2011. The first of these commissioning experiments used both timing options simultaneously so that a comparison between their performance could be made. Further details about this commissioning experiment shall also be presented in this thesis, along with an in-depth analysis of the commissioning data. From this analysis, a decision as to which timing option is best for the final LYCCA array shall be made.

Results from the commissioning experiment combined with those from the optimisation experiments will be able to provide an insight into the feasibility of producing a timing wall of polycrystalline diamond detectors that are able to achieve a sub-100 ps timing resolution.

1.4 LYCCA Simulation Package

The motivation for this work stems from simulations of the LYCCA array produced by M.J.Taylor [13]. The simulations model a typical HISPEC experiment, incorporating the fragment generation, fragment selection and the response from the LYCCA detectors into one simulation code. Initially, a two-step fragmentation reaction, identical to a reaction used in a previous RISING experiment, was simulated. This reaction used a ^{58}Ni beam onto a ^{9}Be target, producing ^{55}Ni fragments that were selected and impinged upon a ^{9}Be secondary target before passing through the CATE ΔE-E detectors. A comparison between the simulated energy loss versus residual energy plot, and a plot generated by the data collected by CATE during the RISING campaign can be seen in Figure 1.1. Both the experimental and simulated data show that, although fragments are distinguishable by their charge, different isotopes of the same species of fragment cannot be separated.

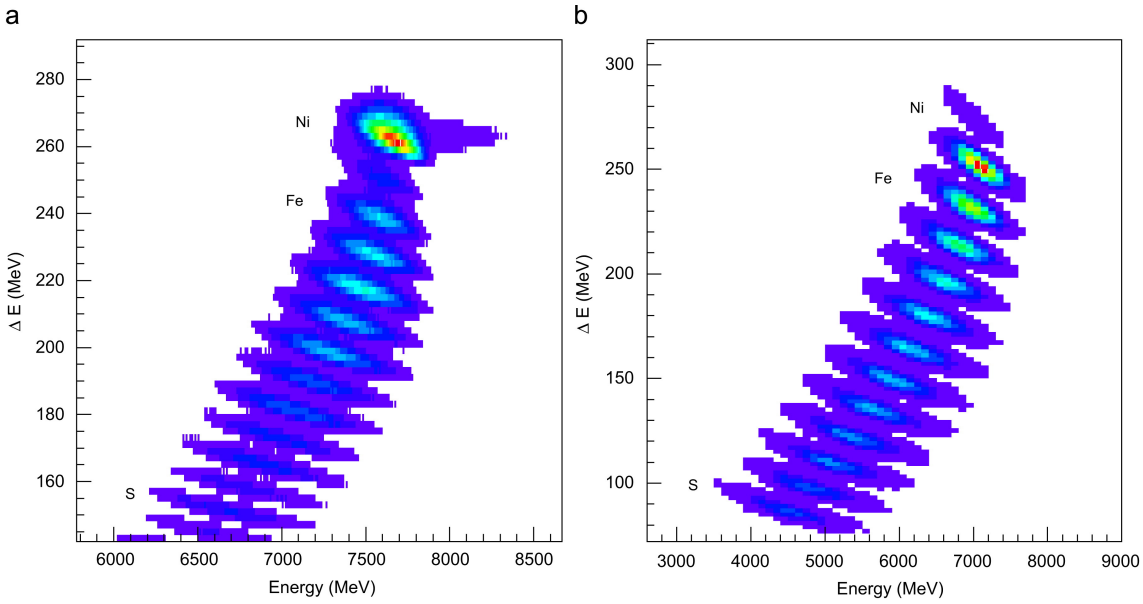

Figure 1.1: A comparison between the energy loss versus residual energy plots from (a) experimental data obtained by CATE during a RISING experiment and (b) simulated data for the same reaction. [13]

The LYCCA-0 detector geometries, including both diamond and fast plastic timing options, were then integrated into the simulation by defining their sizes, position and material properties using GEANT4. An investigation into fragment identification using energy and ToF measurements was undertaken using different ToF flight paths and detector resolutions.

Figure 1.2 shows the simulated ToF versus energy plots obtained for Fe fragments, assuming a full-width-half-maximum (FWHM) energy resolution of 1 % for the CsI detectors, and a FWHM timing resolution of 100 ps and 50 ps (Figures 1.2a and 1.2b respectively) for the diamond detectors. The simulation used a flight path of 3.4 m, the same as that expected to be used in LYCCA experiments. Although some distinction between the isotopes in the identification plots can be observed with a timing resolution of 100 ps, a clear improvement in the isotope separation is seen when the timing resolution is decreased to 50 ps.

These simulations help to determine the minimum acceptable energy and timing resolution values required for unique fragment identification. If one is to distinguish between neighbouring isotopes for fragments around $A = 50$, an energy resolution of 1 % (FWHM) is required for the CsI detectors, and a timing resolution of at least 100 ps (FWHM), and preferably 50 ps (FWHM) is desirable for the timing detectors. The purpose of the work presented in this thesis is to determine the feasibility of this aim for both diamond and plastic ToF options under realistic experimental conditions.

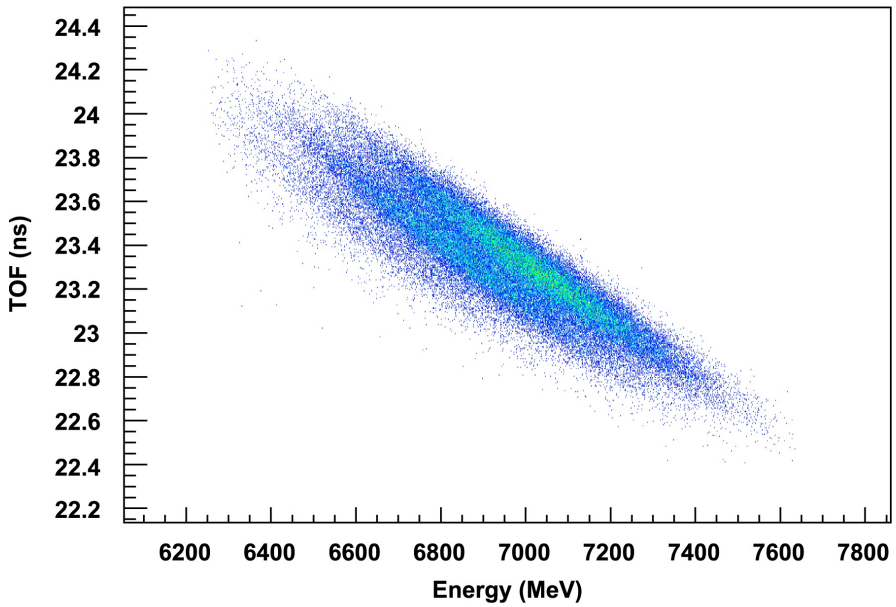

(a) 100 ps (FWHM)

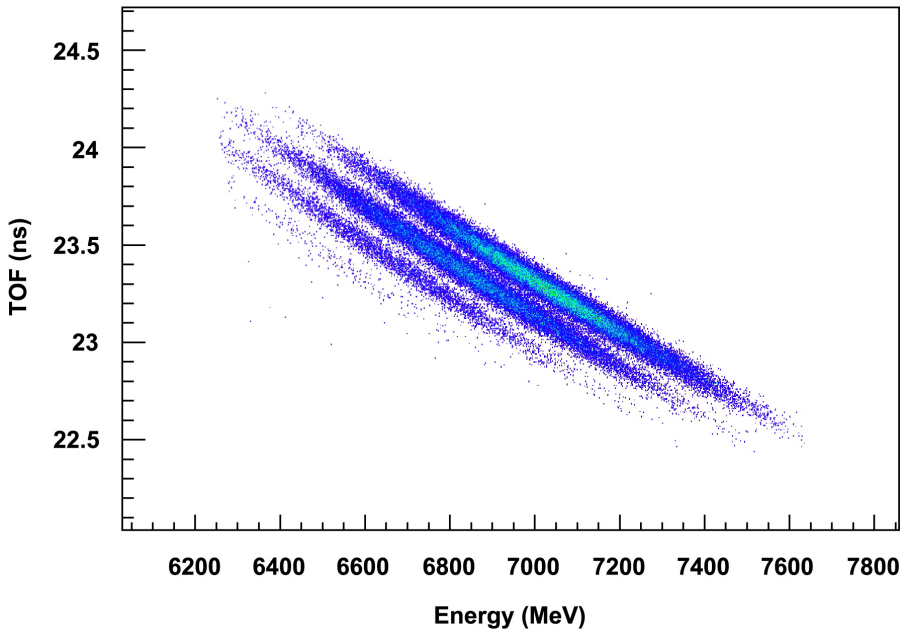

(b) 50 ps (FWHM)

Figure 1.2: Simulated ToF versus E plots for Fe fragments, created assuming an energy resolution of 1 % (FWHM) for the CsI detectors and a timing resolution of (a) 100 ps (FWHM) and (b) 50 ps (FHWM) for the diamond detectors. Some separation between the different can isotopes can be seen with a resolution of 100 ps, however, this separation is much improved when a resolution of 50 ps is assumed.

CHAPTER 2

Diamond as a Timing Detector

2.1 Previous Work with Diamond Detectors

As production methods have improved and the unique properties of diamond have become better understood over the past decade, the use of diamond for particle detection has grown in popularity. Diamond has a high tolerance to radiation due to its well-known hardness, making it an ideal candidate as a beam monitor in high intensity, hostile radiation environments such as inside the Compact Muon Solenoid (CMS) at the Large Hadron Collider (LHC) [14]. The fact that diamond has a near-tissue equivalence, i.e., diamond has a similar mean atomic number to tissue (Z = 6 for diamond, Z = 7.5 for human tissue) also makes it an attractive material for use in X-ray dosimeters [15].

A large proportion of recent research into diamond detectors has focused upon exploiting the fast electron and hole mobilities within the material to create fast timing detectors with very good timing resolutions. A lot of this research has been performed by a group at GSI, led by E Berdermann, who have been involved in collaborations such as NoRHDia (Novel Radiation Hard CVD Diamond Detector for Hadron Physics), HADES (High Acceptance Di-Electron Spectrometer) and FOPI (FOur PI), all of which use diamond detectors for time-of-flight measurements [16, 17, 18]. Recently, this group has come to concentrate their research on trying to

obtain the best possible timing resolution from the diamond detectors for minimum-ionising particles (MIP) such as protons and light nuclei, which deposit very little energy within the detectors.

Another member of the GSI group, M Ciobanu, has recently written a review article that summarises their most recent experimental results, as well as providing a detailed theoretical approach to the signal generation from a diamond detector, which is outlined in Section 2.5 [19]. This article emphasises the importance of detector capacitance and signal-to-noise ratio (S/N) on the timing resolution of the diamond detectors for both single-crystal diamond detectors (scDD) and polycrystalline diamond detectors (pcDD). Tables 2.1 and 2.2 give an overview of the detector properties and timing results from the review article, where C_{DE} is the estimated detector capacitance, calculated from the area, thickness and relative permittivity of the detector, and C_{DM} is the measured detector capacitance, which also includes stray capacitances from the input of the preamplifier. All timing resolutions in Table 2.2 are given as full-width-half-maximum (FWHM) values.

Ion: Type, Energy	**Dimensions (mm^3)**	**Pad Area (mm^2)**	C_{DE} **(pF)**	C_{DM} **(pF)**
p **@** 1.25 GeV	4 x 4 x 0.5	1.69	0.165	1.2
p **@** 3.5 GeV	4.7 x 4.7 x 0.5	1.46	0.142	1.5
^{6}Li **@** 1.8 AGeV	4 x 4 x 0.4	1.69	0.2	3.3
^{6}Li **@** 1.8 AGeV	3.5 x 3.5 x 0.05	1.43	1.4	2.5
^{27}Al **@** 2.0 AGeV	10 x 10 x 0.5	52.8	5.1	6.8
^{58}Ni **@** 1.9 AGeV	20 x 20 x 0.15	23.8	7.7	9.2
^{181}Ta **@** 1.0 AGeV	10 x 10 x 0.5	52.8	5.1	6.8

Table 2.1: Dimensions and capacitance details of diamond detectors tested by the GSI group. Based on tables from [19].

From a LYCCA point of view, the most important results from the tables above are those for polycrystalline diamond with heavy ions. These show that a timing resolution of less than 100 ps is achievable using polycrystalline diamond, which satisfies the requirements for a LYCCA ToF system (see Section 1.4). This point is supported further by experimental results from A Stolz *et al.* [20], who obtained a timing resolution of 49 ps (FWHM) using two single-crystal diamond detectors, measuring 3.5 mm in diameter, with a 87 MeV/u ^{78}Kr beam.

It should be noted that, for the vast majority of diamond detectors tested in the past, the detectors have measured no more than 10 mm x 10 mm, a great deal smaller than the 60 mm x 60 mm start detector required for this project. In fact, results

Ion: Type, Energy	Crystal Type	Energy Loss (MeV)	Resolution (ps)
p @ 1.25 GeV	scDD	0.32	712
p @ 3.5 GeV	scDD	0.30	275
^{6}Li @ 1.8 AGeV	scDD	2.24	129
^{6}Li @ 1.8 AGeV	scDD	0.28	75
^{27}Al @ 2.0 AGeV	pcDD	52.9	66
^{58}Ni @ 1.9 AGeV	pcDD	75.1	106
^{181}Ta @ 1.0 AGeV	pcDD	1962	52

Table 2.2: Timing resolution results for both single-crystal and polycrystalline detectors, along with the energy deposition within the diamond for each test. All timing resolutions are FWHM values. Details of the dimensions of detectors used in these experiements are listed in Table 2.1. Based on tables from [19]

from tables 2.1 and 2.2 suggest that increasing the detector size above 10 mm x 10 mm worsens the timing resolution. This emphasises the expected difficulties with building a diamond detector of this size, whilst still maintaining a timing resolution of less than 100 ps.

2.2 Material Properties of Diamond

Diamond is unique in many ways, not only is it one of the hardest substances, but it also has the highest known thermal conductivity, a very low dielectric constant and, as previously mentioned, fast electron and hole mobilities. It is the last of these which is of most interest when considering diamond as a timing detector. Further details of the properties of diamond and the electron and hole transport from a solid-state perspective are given in this section.

2.2.1 Diamond Lattice and Structure

The crystal structure of any semiconductor is described as a diamond crystal-structure, which may also be described as two interlaced face-centred-cubic structures, offset by $(\frac{1}{4}, \frac{1}{4}, \frac{1}{4})$, as is displayed in Figure 2.1. The single *2s* electron orbital and three *2p* electron orbitals found in each carbon atom of diamond mix together to form four sp^3 hybrid orbitals. Each of these orbitals are then able to bond with one other sp^3 hybrid orbital found in neighbouring atoms to create four covalent bonds in a distinctive tetrahedral shape [21]. The relatively small size of the carbon atoms (the smallest of any semiconductor material) means that they are able to get

much closer to one another before experiencing any repulsion, resulting in short and extremely strong covalent bonds. It is the strength of these bonds that gives rise to the extreme radiation hardness of diamond, as a large amount of energy is required to remove or shift a carbon atom from its place in the crystal lattice.

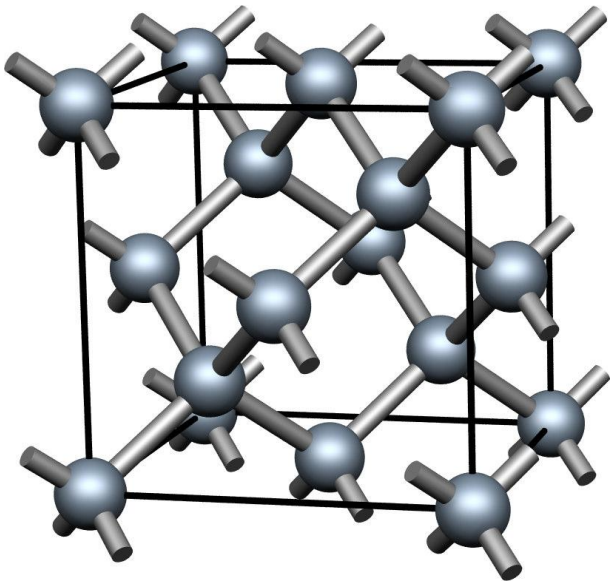

Figure 2.1: Schematic diagram showing the diamond structure of any semiconductor material. Each carbon atom is covalently bonded to its four nearest neighbours, forming a strong tetrahedral shape. [22]

2.2.1.1 Energy Bands and Band Gaps

When electrons are brought together in a crystal, they arrange themselves into bands of energy, separated by regions of forbidden energy values known as band gaps. These forbidden regions come about due to the interaction of the electron wavefunctions with those of the positive ion cores of the crystal lattice. A material is described as being a semiconductor if the band gap, E_g between the filled valence band and the empty conduction band is small enough to allow electrons to be excited across the band gap into the conduction band at relatively low temperatures. Using only this definition, diamond cannot strictly be described as a semiconductor, because its band gap of 5.48 eV is greater than typical thermal energies. However, diamond still displays many of the electronic characteristics of a semiconductor, and is therefore usually thought of as a wide band gap semiconductor rather than an insulator.

The energy of an electron at any point in the crystal lattice can be calculated by

solving the Schrödinger equation, which describes a free electron perturbed by the periodic potential of the lattice cores:

$$\left[-\frac{\hbar^2}{2m}\nabla^2 + V(\mathbf{r})\right]\phi_{\mathbf{k}}(\mathbf{r}) = E_{\mathbf{k}}\phi_{\mathbf{k}}(\mathbf{r}) \tag{2.1}$$

where the wavefunction of the electron, $\phi_{\mathbf{k}}(\mathbf{r})$, according to Bloch's theorem, is of the form:

$$\phi_{\mathbf{k}}(\mathbf{r}) = e^{i\mathbf{k}\mathbf{r}}U_n(\mathbf{k},\mathbf{r}) \tag{2.2}$$

Here, $U_n(\mathbf{k},\mathbf{r})$ describes a periodic function associated with the electron wave vector, $\mathbf{k}$, which results from the periodic nature of the crystal lattice.

The energy band-structure of diamond, calculated with the aid of equation 2.1, is shown in Figure 2.2a. Both the valence band and the conduction band are made up of four sub-bands, the energies of which vary with $\mathbf{k}$ across the crystal lattice. The symbols found on the x-axis represent certain $\mathbf{k}$ states that are found at symmetry points in the crystal or describe lines of symmetry, as can be seen in 2.2b. The energy band-gap is defined as the energy between the highest point of the valence band and the lowest point of the conduction band, indicated by red crosses in Figure 2.2a. As the figure shows, these instances do not occur at the same point in the crystal structure. This phenomenon is known as an indirect band-gap, and requires the absorption of a photon with an energy equal to the energy of the band gap plus that of a phonon needed for wavevector conservation, in order to be overcome [23].

2.2.2 Charge Carrier Transport

When an electron is excited across the band gap into the conduction band, a positively-charged vacancy is left in the valence band, known as a hole. If an electric field is applied across the crystal lattice, not only does this encourage the excited electron in the conduction band to move in the opposite direction to the electric field, but it also encourages an electron in the valence band to move into the hole left by the excited electron. A second electron then moves into the hole left by the previous electron, and this continues. Rather then focusing upon the successive movement of the electrons in the valence band, it is much easier to track the movement of the hole left behind by these electrons, which travels in the same direction as the electric field. It is, therefore, possible to say that current in a semiconductor is carried by both electrons and holes [25].

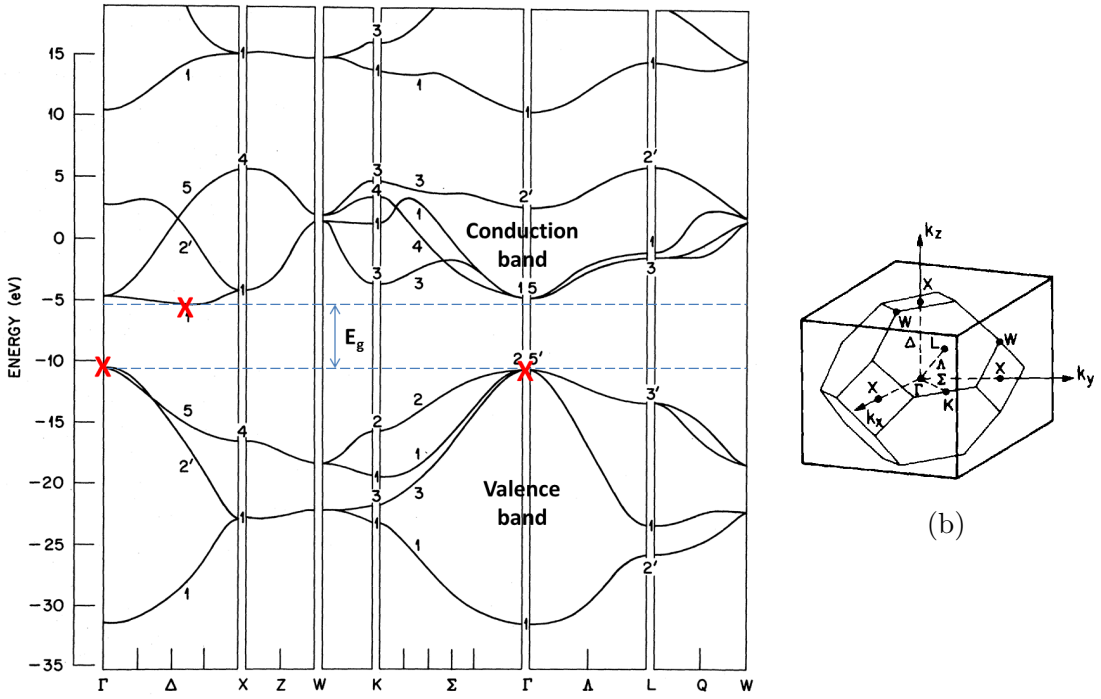

(a) (b)

Figure 2.2: (a) The energy band-structure of diamond, which shows the sub-band configuration of the valence band and the conduction band across the wave vector states, and the lines of symmetry in the diamond lattice. The lowest point of the conduction band, and the highest point of the valence band (indicated by red crosses) do not align, leading to an indirect band gap with a magnitude of 5.48 eV. (b) The symmetry lines and symmetry points of the diamond crystal lattice shown within a Wigner-Seitz cell. The symbols shown in this diagram are adopted from group theory. [24]

One of the most important factors to consider when trying to produce a fast timing detector is the velocity of the charge carriers travelling through the semiconductor crystal. The charge carrier velocity is highly dependent upon the electron and hole mobilities and the saturation field of the semiconductor, which in turn, are highly dependent upon the effective mass of the charge carriers, as well as phonon scattering in the crystal. These points are outlined below.

2.2.2.1 Effective Mass

The motion of electrons and holes through the crystal lattice is affected by the ion cores. With this in mind, it is useful to introduce a concept known as the effective mass of the electron and hole, which can take different values at different states in

the crystal. The effective mass is not a measure of the rest mass of the electron, instead, it describes how the charge carriers accelerate in the electric field under the influence of the ion cores, i.e, what the mass of a similarly behaving charge carrier would be, in the same electric field, if the ion cores were not present.

The effective mass, m^* is defined as:

$$\frac{1}{m^*} = \frac{1}{\hbar^2}\frac{d^2E}{dk^2} \tag{2.3}$$

From this equation, it is clear that m^* is directly related to the curvature of the energy bands. The energy bands in diamond are able to curve in either an upward or downward manner, producing positive or negative values of $\frac{d^2\mathbf{E}}{d\mathbf{k}^2}$, and subsequently, positive or negative values of m^*. A negative m^* value is found near the top of an energy band, and arises from the fact that the electron transfers more momentum to the crystal lattice than it receives from the electric field whilst travelling from state $\mathbf{k}$ to state $\mathbf{k} + \Delta\mathbf{k}$ [23].

2.2.2.2 Charge Carrier Mobilities

The electron and hole mobilities, μ_e and μ_h respectively, are intrinsic properties of a material and are defined as the magnitude of the charge-carrier drift velocity per unit electric field [23] in low electric field situations. Mobilities in a semiconductor such as diamond are found to be highly dependent upon the effective mass of a charge carrier, as well as the temperature, and are found to vary as:

$$\mu \propto (m^*)^{-\frac{5}{2}} T^{-\frac{3}{2}} \tag{2.4}$$

The inverse dependence on m^* seems intuitive, as a lower mass object object will have greater acceleration under the influence of an external force than an object with a higher mass. When comparing typical effective masses for electrons and holes in the same crystal, electrons are nearly always found to have a lower effective mass than holes, and consequently, the electron mobility is usually greater than the hole mobility.

The temperature dependence is related to acoustic phonon scattering in the crystal. At any non-zero temperature, the atoms found in a crystal vibrate about their lattice positions. Neighbouring atoms are able to vibrate either acoustically, where the atoms vibrate in phase with one another with a relatively slow frequency, or optically, which describes vibrations that are perfectly out of phase and have a much higher frequency. It is often advantageous to quantise these lattice vibrations

into phonons with an energy equal to hf, where f is the frequency of the vibrations.

During a phonon-scattering event, electrons either emit or absorb a phonon, causing them to lose energy as they traverse the crystal lattice. The low frequency and low energy of acoustic phonons means that, at low temperatures and electric-field strengths, these phonons dominate the scattering process, and hence, greatly affect the motion of the charge carriers through the semiconductor. As the temperature of the semiconductor increases, more acoustic phonons are found within the lattice, increasing the number of scattering events in the crystal and reducing the mobility of the charge carriers [26].

The electron and hole mobilities of natural diamond ($\mu_e = 1800 cm^2 V^{-1} s^{-1}$ and $\mu_h = 1200 cm^2 V^{-1} s^{-1}$ [23]) are similar in magnitude, and are relatively high compared with other measurements made for similar semiconductors. In fact, recent investigations made by Isberg *et al.* have measured mobilities of $\mu_e = 4500 cm^2 V^{-1} s^{-1}$ and $\mu_h = 3800 cm^2 V^{-1} s^{-1}$ for synthetic single-crystal diamond, which are significantly greater than any other semiconductor material [27].

2.2.2.3 Saturation Velocity

In high electric field environments, a large amount of energy is supplied to the charge carriers by the electric field, allowing the emission of more energetic optical phonons. Above a certain electric-field strength, the amount of energy transferred to the charge carriers from the electric field balances the amount of energy released by phonon emission, and the electric field is unable to accelerate the charge carriers any further [24]. The velocity of the charge carriers at this point is known as the saturation velocity.

Typical optical phonon energies are found to be very high in diamond due to the strong covalent bonding between the carbon atoms, which allows a much larger electric field to act on the charge carriers before saturation is reached. This, combined with the relatively high charge-carrier mobilities in diamond means that diamond has one of the highest saturation velocities of any semiconductor.

2.2.3 Defects and Grain Boundaries

The velocity of the charge carriers in diamond is not only affected by the effective mass and phonon scattering, but also the number of impurities and defects found in the crystal. During the growth of the diamond crystal, some carbon atoms in the crystal lattice may be replaced by other contaminants such as nitrogen or boron,

and some lattice points may even be left vacant. The crystal may also contain dislocations, which can appear when a plane of atoms is terminated before reaching the edge of the crystal, as well as an array of other possible defects.

The presence of these defects causes a difference in the Coulomb interaction compared with that of the periodic interaction usually found in the crystal lattice, and as a result, introduces additional centres for the charge carriers to scatter from [26]. As was described earlier, an increase in scattering leads to a reduction in carrier mobilities and velocities, which is not ideal for obtaining a good timing resolution. It is, therefore, necessary to restrict the number of impurities and defects formed during the diamond growing process.

Polycrystalline structures are made up of many small crystallites, or grains, which are oriented in a random manner, as can be seen in Figure 2.3. Each grain is separated by a grain boundary, which, as with any defect, increases scattering and limits the mobility of the charge carriers. Unfortunately, due to the size requirements of the LYCCA diamond detectors, polycrystalline diamond had to be used rather than single-crystal diamond. This reduces the velocity of the charge carriers, and possibly worsens the timing resolution, but does allow the production of large area diamond detectors to be feasible. The typical grain sizes found in the diamond samples used for the LYCCA project were of the order of 100μm.

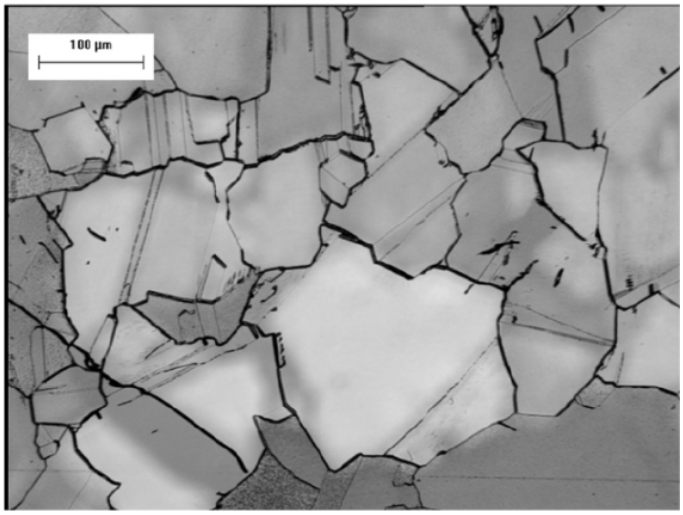

Figure 2.3: Optical microscope image of a polycrystalline diamond sample. The crystallites, or grains, are randomly oriented and separated by grain boundaries. Grain sizes are typically around 100 μm. Adapted from [28].

2.3 Diamond as a Semiconductor Detector

Whilst the previous section gave an insight into how charge carriers travel through a semiconductor crystal such as diamond, the following section will focus on charge carrier generation, as well as comparing the performance of diamond detectors with other semiconductor detectors.

2.3.1 Interactions with Heavy Charged Particles

When a heavy charged particle enters a diamond detector, it is possible for the particle to interact with the carbon atoms by either Rutherford scattering, whereby the projectile interacts with the nucleus of the atom, or via the Coulomb interaction between the projectile and the electrons of the carbon atom. As the nucleus of an atom takes up only around 10^{-15} of the atom's volume, Rutherford scattering occurs only rarely, and the response of a detector to heavy charged particles is dominated by the Coulomb interaction [29].

As the charged particle passes through the diamond material, it interacts with many nearby electrons, causing the electrons to feel an impulse from the attractive Coulomb force [30]. If the path of the charged particle passes particularly close to an electron, the energy transferred from the particle to the electron may be enough to create an electron-hole (e-h) pair in a process known as ionisation. Without the presence of an electric field, these electrons and holes would recombine to create neutral atoms, but, as was described in the previous section, applying an electric field across the detector suppresses this recombination, causing the electrons and holes to travel in opposite directions.

The number of e-h pairs created within the detector material is directly related to the energy lost by the charged particle as it passes through the detector. The rate of energy loss of a charged projectile through any absorber can be described using the Bethe formula, which is found to be inversely proportional to the energy of the projectile. This dependence seems reasonable as a low-energy particle moves more slowly through the detector, and therefore spends more time in the vicinity of a given electron in the detector material. This allows the charged particle to impart a greater impulse on the electron, which subsequently leads to a larger energy transfer from the projectile, and an increase in the energy loss rate. The rate of energy loss also varies roughly as the square of the projectile's charge. This dependence arises from the fact that the Coulomb force acting between the charged particle and

an electron in the detector increases as the particle charge increases, once again allowing more energy to be transferred to the electron.

2.3.2 Comparing Semiconductor Detectors

The difference in behaviour between diamond detectors and other widely-used semiconductor detectors, such as Si and Ge, can largely be attributed to diamond's wide band gap. Thermal energies alone are enough to generate e-h pairs in typical semiconductors, leading to a significant charge-carrier density in both the valence and the conduction band before any ionisation by incoming particles occurs. The current produced by these thermal e-h pairs, known as leakage current, can often swamp the signal current produced by charged particle interactions.

To counteract this problem, Si detectors use electron and hole dopants to form a pn-junction, which causes the thermal electrons to diffuse toward the additional holes found in the p-type material, and the thermal holes to diffuse toward the additional electrons found in the n-type material, creating a region of low charge-carrier density at the centre of the junction. The leakage current can be reduced to just a few μA by reverse biasing the pn-junction, which further decreases the charge-carrier density in this region. It is also possible to minimise the leakage current in a detector by cooling the material down to just a few Kelvin, thereby decreasing the thermal energy of the detector to below the energy required to create an e-h pair. This technique is commonly used when operating Ge detectors.

Diamond's large band gap means that, even at room temperature and without the presence of a pn-junction, the leakage current in a diamond detector is typically less than 10 nA, and allows any signal formed by heavy charged particles to be easily detectable. This makes fabricating and operating a diamond detector more straightforward than a Si or Ge detector.

Although a wide band gap may be useful for providing low leakage currents in diamond detectors, it also means that fewer e-h pairs are created in the path of a charged particle as it passes through the detector. This leads to diamond detectors producing signals of lower amplitude when compared with signals from a Si detector. Although the timing resolution of a detector is mainly dependent upon the rise time of a signal, which should have very little dependence on the pulse height, it can be difficult to pick out the rising edge of a signal if the pulse height is just above the noise level. This should not be an issue when using the diamond detectors as part of the LYCCA array at GSI, as the secondary beams should deposit a few hundred

MeV in the detectors, creating a signal with a pulse height that is well above the noise.

2.3.3 Trapping and Polarisation Fields

A polarisation field is a phenomenon that affects polycrystalline diamond detectors more than most other semiconductors. Grain boundaries, impurities and intra-grain defects can all act as charge-carrier traps by introducing additional energy levels within the band gap of diamond. When a charge carrier travelling under the influence of an electric field encounters one of these traps, it becomes captured and fails to contribute further to the signal current, as is visualised schematically in Figure 2.4. A shallow trap is one in which the additional energy levels are found close to the conduction or valence band, and a trapped charge carrier can usually be excited out of the trap by thermal energies [30].

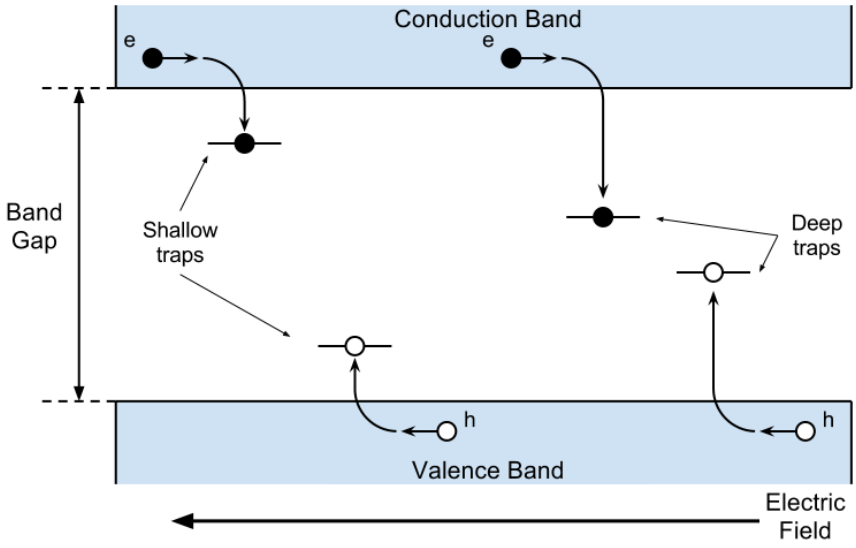

Figure 2.4: Diagram showing how energy levels created by defects and grain boundaries in polycrystalline diamond can cause both shallow and deep traps for electrons and holes. Charge carriers can be excited out of shallow holes by thermal energies.

Deep trapping can also occur if additional energy levels are situated toward the centre of the band gap, and require a large amount of energy to escape from. As a result, charge carriers can spend an appreciable amount of time in deep traps, which, due to the presence of the electric field, can lead to a build-up of trapped electrons and hole close to their corresponding electrodes. As can be seen in Figure 2.5, the charge generated by this build-up creates a polarisation field which acts to

oppose the externally applied electric field, effectively reducing the strength of the field [31]. As a consequence, the velocity of the charge carriers is decreased, which limits the timing resolution of a polycrystalline diamond detector.

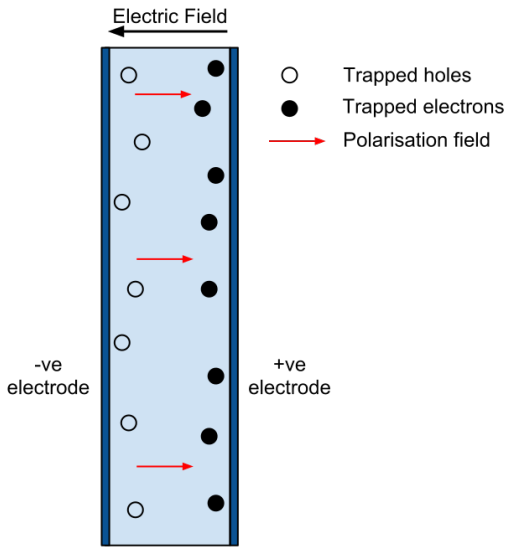

Figure 2.5: Schematic diagram showing the formation of a polarisation field. Electrons and holes are trapped as they travel toward their corresponding electrodes, creating regions of similar charge which generates the polarisation field.

A trapped electron is also far more likely to encounter a passing hole, or vice versa, causing a recombination event. This then eliminates both the electron and hole from contributing to the final signal current, reducing the height of the signal. For single-crystal diamond, a lack of grain boundaries means that nearly all of the charge carriers created in an ionisation event are collected at the detector electrodes, leading to a charge collection efficiency (CCE) of around 1. The CCE for polycrystalline diamond is usually between 0.1 and 0.6 [19], depending upon grain size, which significantly affects the amplitude of the detector signal. This only becomes an issue in high noise environments or with minimally-ionising particles, where the signal is difficult to distinguish above the noise.

2.4 Construction of Diamond Detectors

As was discussed in Section 2.3.2, the general construction of a diamond detector is relatively simple when compared with a Si or Ge detector. However, if the best possible timing resolution is to be achieved from a large area diamond detector,

as is aim for this project, the task becomes more challenging. The low CCE of polycrystalline diamond means that the type and quality of the contact used for the detector electrodes becomes more important. Details about the fabrication of the detector, diamond wafer and the contacts are given below.

2.4.1 Diamond Detector Construction

A diamond detector consists of a diamond wafer sandwiched between two metallic electrodes on the top and bottom faces. A bias is placed between the two electrodes, with a voltage of 0 V on the bottom electrode, known as the ground pad, and voltages of a few hundred volts on the top electrode. This bias instigates the motion of charge carriers within the diamond, which induces a current signal on both electrodes, the height of which depends upon the velocity and abundance of the charge carriers. Attached to these electrodes are gold bonding wires, which carry the signal between the diamond wafer and the printed circuit board (PCB). From the PCB, the signal is sent to a preamplifier, which is specially designed for fast, high-frequency signals.

One of the major design requirements for the LYCCA ToF start detector was that it had to cover the entire secondary target, an area of 60 x 60 mm^2. It was, therefore, decided to use polycrystalline diamond wafers measuring 20 x 20 mm^2, the largest available from Diamond Detectors Limited (DDL) at the time of purchase, so that nine wafers could be arranged on a PCB to cover the full 60 x 60 cm^2 area. A thickness of 0.3 mm was chosen for the diamond wafers to ensure that any charged particles passing through the detector deposited sufficient energy to generate a signal above the noise level, but wasn't too thick to cause straggling or nuclear reactions to occur frequently inside the detector.

A number of PCBs were tested whilst developing the diamond detectors in order to find the most important features for producing the best possible timing resolution from the detector. In one of the first detector tests undertaken, which is not described in this thesis, it was found that the impedance of the PCB must match that of the cables and preamplifier, otherwise signal reflections occur at the connection points between the detector components. The frequency of these reflections were similar in magnitude to the rise time of the signal, which added unwanted jitter to the signal measurements and significantly worsened the timing resolution. Other factors were also considered when designing the PCB for the diamond detectors, such as the distance needed between signal tracks to prevent breakdown on the PCB, and the PCB grounding method.

2.4.2 CVD Mechanism

Chemical vapour deposition (CVD) is a fairly new advancement in the synthesis of diamond, and has proven to have many advantages over the traditional high temperature/high pressure (HT/HP) method. CVD allows the reproducible growth of diamond crystals with few impurities and defects and, most importantly for the LYCCA project, also allows larger samples to be grown.

In CVD, carbon atoms from a dissociated hydrocarbon gas are deposited onto the surface of a solid substrate. One example of the CVD process is shown in Figure 2.6. A gas, usually CH_4, is fed through an activation area in order to heat the gas, as well as produce methyl radicals and hydrogen ions that are able to interact with the surface of the substrate. A number of methods can be used to activate the gas, although the most common are thermal techniques, such as a hot filament or a flame, or electrical discharge, such as microwaves or RF. The precursor gas is often diluted in hydrogen to encourage the growth of diamond rather than graphite, and temperatures of greater than 700 °C are used to prevent the growth of amorphous carbon [32].

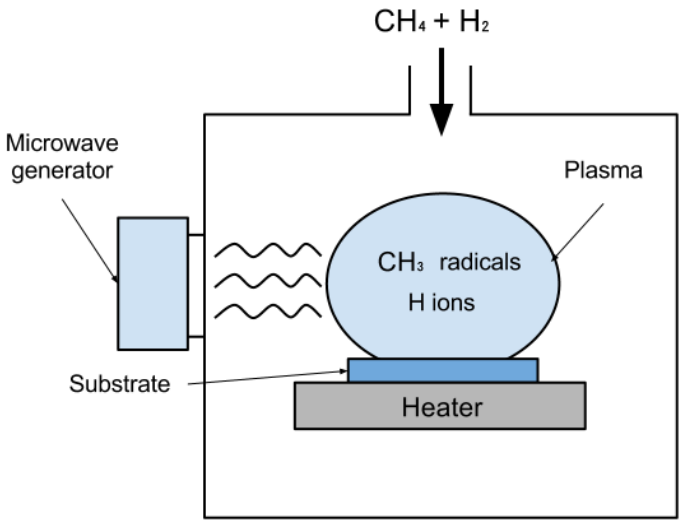

Figure 2.6: Schematic illustration showing the procedure for chemical vapour deposition (CVD). For this example, microwaves are used to activate the gases, however, other methods such as a hot filament and a combustion flame can also be used, as described in the text. Adapted from [32]

The choice of substrate can greatly influence the diamond growth. When forming single-crystal diamond, a substrate of either natural or synthetic diamond is used,

whereas a non-diamond substrate is used when growing polycrystalline diamond [33]. This non-diamond substrate needs to have a melting point greater than the temperature of the growth process, as well as a thermal expansion coefficient comparable to that of diamond [32]. Once growth on the substrate surface has begun, it continues in a columnar manner upwards from the substrate. Grain sizes are found to increase with distance from the substrate surface, meaning the best quality CVD diamond for timing purposes should be cut away from the top of the diamond film after a considerable growing period.

In order to stop the CVD growth process, the very top layer of CVD diamond has to be terminated with another element to prevent the dangling bonds from forming any further sp^3 bonds with the methyl radicals. Usually, either hydrogen or oxygen gas is used to terminate the diamond wafer.

2.4.3 Contact Fabrication

The majority of the detector contacts were fabricated at the University of Surrey, with whom the University of York were in close collaboration throughout the project. Although a range of different metals were used during the optimisation experiments and the LYCCA-0 commissioning, the fabrication of these contacts followed the same procedure each time. The diamond wafers were first cleaned in solutions of aqua regia, acetone and isopropanol to remove any residue which may affect the cohesion between diamond and contact. The metal was then deposited directly onto the surface of the diamond wafer using a Turbo Sputter Coater and a shadow mask to define the size and shape of the contacts. In some cases, such as the deposition of Au, it was necessary to use photolithography to create the contact, due to the nature of the metal [34].

Three different shadow masks were used during contact fabrication, the patterns of which can be seen in Figure 2.7 (top). The ground-pad pattern shown in this figure was applied to the bottom face of all diamond wafers used throughout the project. The four-strip pattern of Pattern 1 was deposited onto the top face of the diamond wafers used during the Texas A & M optimisation experiment and the commissioning run at GSI, whereas Pattern 2 was used when fabricating the contacts for the Birmingham optimisation experiment. A second fabrication method, developed by DDL, was also used during the Birmingham experiment. Rather than depositing the metal directly onto the diamond surface, a thin layer of diamond-like carbon was applied between the diamond and the metal contact, which improved

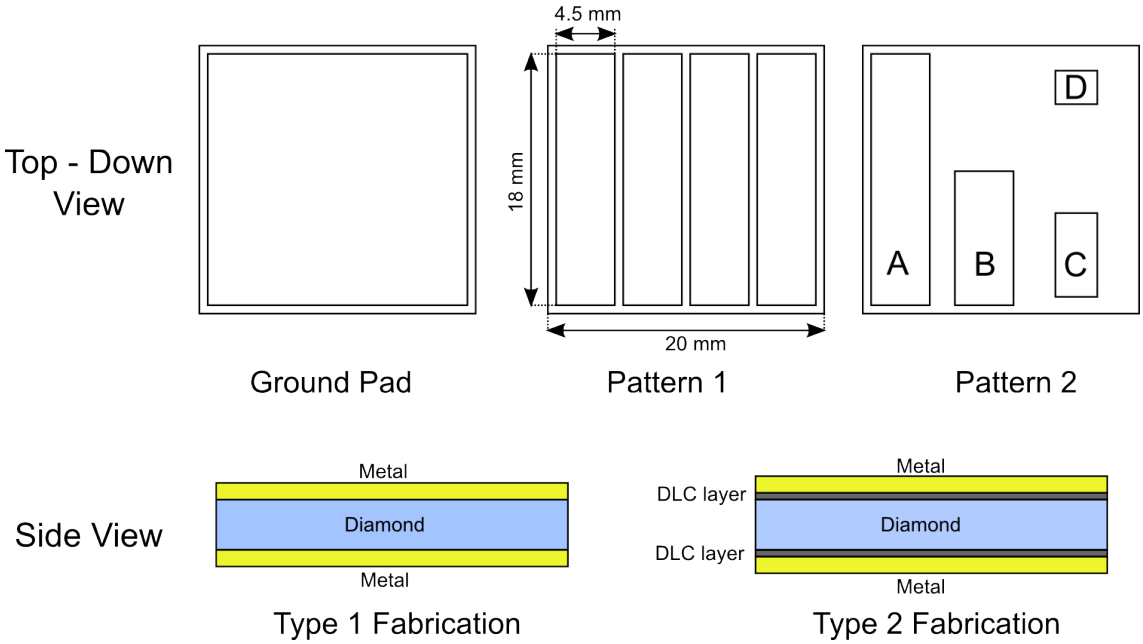

Figure 2.7: Diagram showing the pattern of the contact pads used during the optimisation experiments and LYCCA-0 commissioning, as well as the two types of contact fabrication used. The ground-pad pattern was fabricated onto the bottom of every diamond wafer used, whereas either pattern 1 or pattern 2 was deposited onto the top surface of the wafer.

the charge collection by forming an ohmic contact with the diamond and metal interfaces (see Figure 2.7 (bottom)).

2.4.3.1 Ohmic and Schottky Contacts

When a metal comes into contact with a semiconductor such as diamond, the Fermi energy levels, i.e., the energy at which the probability of finding an electron is exactly one half, of the two materials form an equilibrium. In the case of an intrinsic semiconductor, for example, the Fermi level is situated at the centre of the band gap. In order for equilibrium to occur, the energy bands within the semiconductor are often required to bend, and it is the nature of this band bending which determines whether an ohmic or a Schottky contact is formed between the two interfaces.

A hydrogen terminated diamond wafer is found to have a highly conductive layer near its surface, which results in p-type properties at the diamond surface [35, 36]. When this is the case, it is necessary to focus on the movement of the holes, i.e., the majority charge carrier.

A Schottky contact is formed if the work function, ϕ_m, of the metal is less

than that of the semiconductor, ϕ_s. As can be seen in Figure 2.8a, when the two materials first make contact, diamond has the lower Fermi energy level. Holes in diamond are able to lower their energy by flowing into the conduction band of the metal, increasing the energy of the Fermi level in diamond until it becomes equal to that of the metal. This causes downward band bending in the diamond (see Figure 2.8b), generating a potential barrier, V_B which holes in the diamond have to overcome in order to pass into the metal [25].

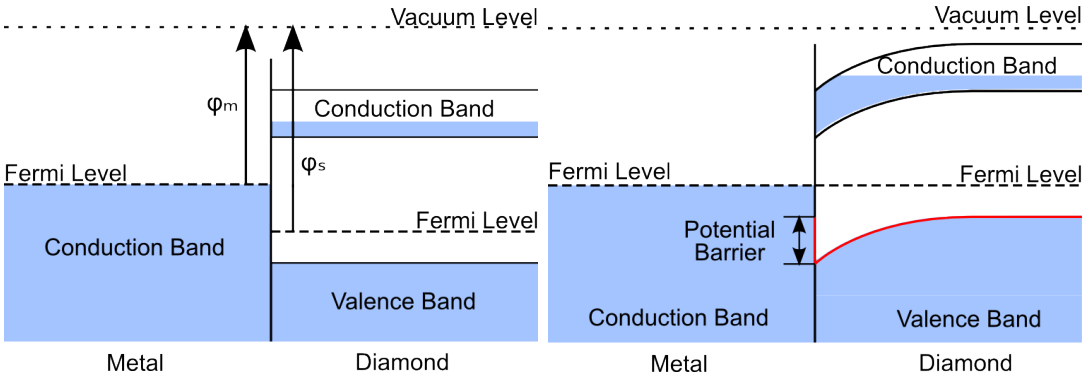

(a) Just after contact (b) Once equilibrium has been established

Figure 2.8: Schematic diagrams showing the energy levels of a Schottky contact (a) just after contact has been made, where the Fermi level of the semiconductor is lower than that of the metal, and (b) after holes from the semiconductor have flowed into the metal and equilibrium has been established. A potential barrier (red) is created from the downward bending energy bands in diamond, hindering the movement of the holes from diamond into the metal. Based on [37]

Conversely, an ohmic contact can be created if ϕ_m is large. In this case, the Fermi level in the metal is at a lower energy than the Fermi level in the diamond, encouraging holes in the metal to flow into the valence band of the semiconductor, increasing the Fermi level of the metal. The energy levels in diamond bend upwards as a result of this, and charge carriers in each material can readily exchange with one another.

Although the vast majority of semiconductor-metal interfaces are known to be Schottky in nature, the Schottky barriers formed between diamond and metals such as Au, Ti and Pt are found to be low, and are often considered to act as ohmic contacts. Aluminium, on the other hand, has a lower work function than the afore mentioned metals, and therefore creates a larger Schottky barrier. When constructing a detector, it is best to collect as many charge carriers at the electrode as possible, and hence, ohmic contacts are preferred over Schottky contacts.

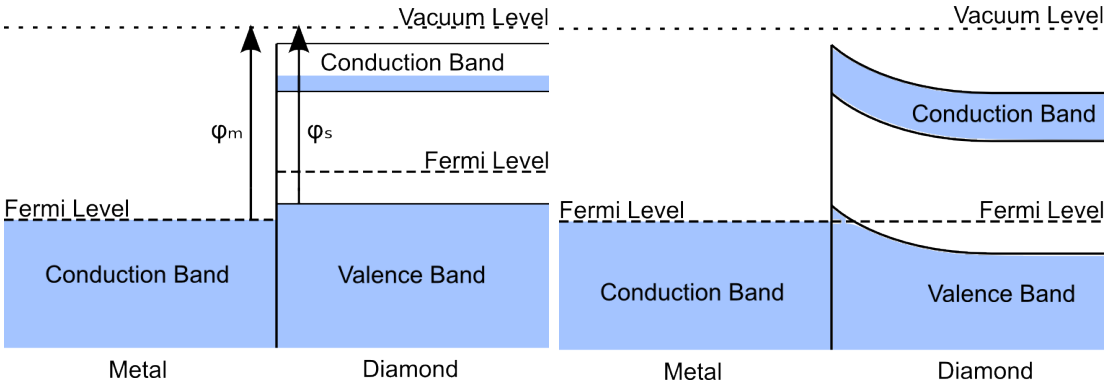

(a) Just after contact (b) Once equilibrium has been established

Figure 2.9: Schematic diagrams showing the energy levels of an ohmic contact (a) just after contact has been made, where the Fermi level of the metal is lower than that of diamond, and (b) after holes from the metal have flowed into the valence band of the semiconductor and equilibrium has been established. The upward curvature of the energy bands in diamond allows charge carriers in both materials to exchange without any hindrance. Based on [38]

2.4.3.2 Diamond-Like Carbon

Diamond-like carbon (DLC) is an amorphous carbon material made up of a mixture of sp^2 and sp^3 bonding. The use of diamond-like carbon as an ohmic contact for diamond detectors was developed and patented by DDL. When forming an ohmic contact with metals such as Au and Ti, the cohesion between diamond and the metal can often be poor, causing gaps to form between the two interfaces which worsens the charge collection efficiency and reduces the reliability of the contact. DLC has proven to cohere more strongly with the diamond surface due to the similarities between the structures of diamond and DLC. When a DLC layer is placed between diamond and metal surfaces, a greater proportion of sp^3 bonded atoms are formed close to the diamond interface, and a large number of sp^2 bonded atoms are found close to the metal interface. This is done to ensure good adhesion to both surfaces, which helps to increase the lifetime of the diamond detector.

If a very thin layer ($\sim$3 nm) of DLC is deposited between the diamond surface and metal surface, the DLC can act as a quantum mechanical tunnel by allowing the wavefunctions in each material to overlap. This enhances the flow of charge carriers between the metal and semiconductor and increases the CCE at the electrodes [39].

2.5 Signal Generation

The signal generated on the detector electrodes by the charge carriers within the diamond can be described in terms of both charge variations and current variations with time. Whether the charge signal or the current signal is extracted depends upon the information required from the diamond detector. This section will illustrate the differences between the two signals, and explain which signal is best for use with timing detectors.

2.5.1 Formation of the Pulse Shape

When charge carriers are generated within the diamond material by ionising charged particles, they begin to move under the influence of the applied bias. This induces a charge on the contacts of the detector, which continues to build until the motion of the charge carriers ceases, either by collection at the contact, or by becoming trapped. The time taken for this motion to end is known as the charge transit time. The dotted lines shown in Figure 2.10 demonstrate how the build-up of induced charge on the electrodes varies with time. The rise time of this charge signal, defined here as the time taken for a signal to rise from 10% to 90 % of its maximum height, is equivalent to the charge transit time.

The full rise time of the charge signal from the detector contains contributions from the electron, as well as the slower moving hole. Figure 2.10 shows these contributions from an e-h pair generated halfway between the detector contacts, and an e-h pair created close to the positively charged electrode. In the latter case, the hole is required to traverse the full thickness of the diamond wafer, and the rise time becomes dominated by the collection time of the hole. The difference between electron and hole mobilities creates a dependence on the interaction position within the diamond wafer, and introduces a variation in the rise time of the signal.

Once all charge carrier motion has stopped, the charge that has built up on the detector electrode decays in the same manner as a discharging capacitor. The area under the resultant signal pulse corresponds to the total charge collected at the electrodes.

As soon as charge starts to build on the detector electrodes, a current begins to flow in the detector circuit, and continues to flow until charge carrier motion ceases. Ideally, the current variation through the detector circuit with time should replicate the schematic diagram shown in red in Figure 2.11(b), where both the rise

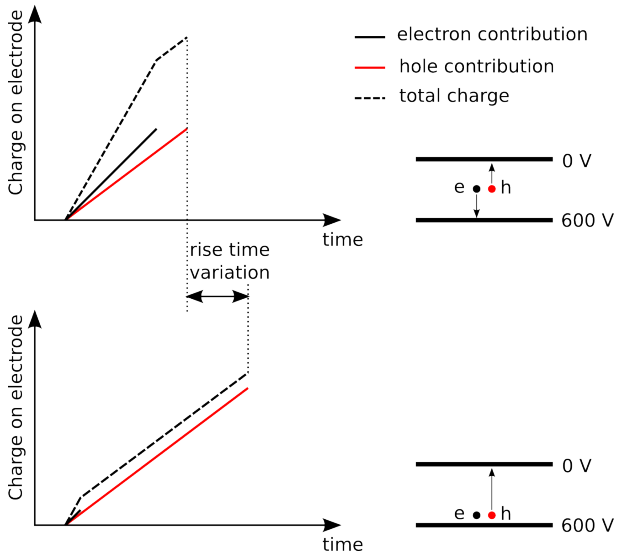

Figure 2.10: Schematic diagrams showing contributions to total rise time made by electrons and holes as they travel toward their respective electrodes. The top diagram shows an example where the e-h pair is generated halfway between the electrodes. The bottom diagram shows an example where the e-h pair is generated close to the positive electrode, and the rise time is dominated by the collection time of the hole. This position dependence brings about a rise time variation.

time and decay of the current pulse should be instantaneous. However, the intrinsic capacitance of the diamond detector affects how the current flows in the detector circuit, and gives the current pulse a characteristic rise time and an exponential decay, as illustrated in black in Figure 2.11(b).

Unlike the charge pulse, the rise time of the current pulse is not affected by charge carrier motion, and therefore does not suffer from rise time variation caused by dependence of the interaction position within the diamond wafer. Instead, the rise time is only dependent upon the capacitance of the detector circuit, and the charge transit time that defined the rise time of the charge signal in fact defines the width of the current pulse, because current only flows when the charge carriers are in motion.

Investigations into the charge transit times undertaken by Pomorski *et al.* in reference [40] indicate that typical charge transit times range between 5 ns and 20 ns for single-crystal diamond wafers that were 300 μm to 500 μm thick. Results from this reference also show that the transit time increased with decreasing charge collection efficiency, which suggests that the charge transit time through polycrystalline diamond will be considerably greater than 20 ns.

Similar results using the Transient-Current Technique (TCT) for single-crystal

diamond were obtained by Pernegger *et al.* [41], and can be seen in Figure 2.12. The left-hand and right-hand plots show the current pulses acquired when holes and electrons respectively are required to traverse the full thickness of the diamond wafer. Each pulse in the two plots was measured using a different detector bias, with the highest biases producing the largest signals. The decrease in current from the holes and the increase in current from the electrons that can be seen in these signals was attributed to an accumulation of negative space-charge within the diamond.

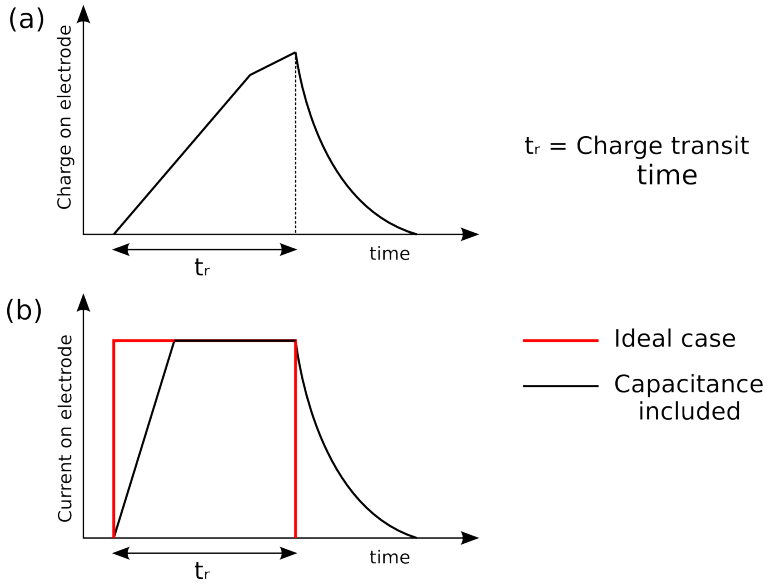

Figure 2.11: Schematic diagrams showing (a) the variation in induced charge on the detector electrodes and (b) the variation in current in an ideal scenario (red) and when the detector capacitance is taken into account (black). The charge transit time helps to define the rise time of the charge signal, whereas for the current pulse, it characterises the width of the signal.

A comparison between the charge signal induced on the electrodes and the resulting current signal can be seen in Figure 2.11. These schematic diagrams indicate that the rise time of the current signal is superior to that of the charge signal for the purposes of timing measurement, as not only is it faster but also contains less variation from pulse to pulse.

The pulse height of the current signal is determined by the rate at which charge is induced upon the detector electrodes. Effectively, this means that charge carriers travelling with a greater velocity will generate a larger signal than slower moving charge carriers. The high charge-carrier saturation velocities found in diamond are therefore advantageous when making timing measurements from the current signals of a diamond detector, as high amplitude pulses serve to improve the S/N ratio and,

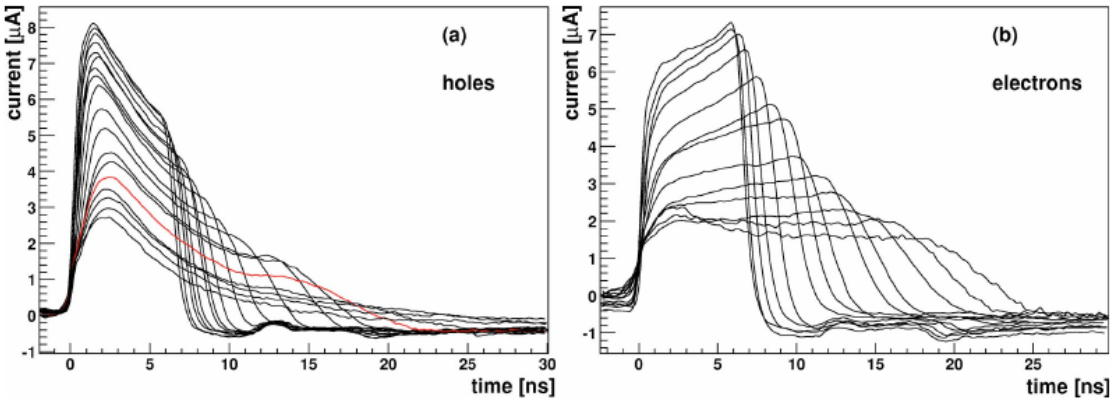

Figure 2.12: Current pulses from a single-crystal diamond detector obtained by H Pernegger et al. [41] using TCT. The left-hand plot shows the current pulses acquired when holes traversed the full thickness of the detector, whereas the right-hand plot shows the same for electrons. Different detector biases were to measure the current signals, and the largest signals seen in these plots represent those measured using the highest biases.

consequently, the timing resolution of the detectors.

2.5.1.1 Plasma Time

If a large number of e-h pairs are generated within a small area of the diamond wafer, as is possible from interactions with heavy charged particles, a plasma-like cloud of charge is created, which shields the charge inside the cloud from the applied bias. Only e-h pairs found toward the outside of the cloud feel the influence of the bias and begin to move toward their respective electrodes, exposing e-h pairs found closer to the centre of the cloud to the external electric field [30]. This delay in motion of charge carriers at the centre of the plasma cloud, known as the plasma time, causes the rise time of both the charge and the current signal to lengthen.

The fast electron and hole mobilities in diamond mean that the shielding charge carriers on the outside of the plasma cloud are able to disperse more readily than charge carriers in other semiconductors such as Si, and as a result, the plasma time associated with diamond is found to be less than other semiconductors [42].

2.5.2 Pre-Amplification

The signal from any semiconductor detector is so small that amplification of the signal, by means of a preamplifier, is essential before any pulse processing with a discriminator can occur. However, it is important to choose the correct type of

preamplifier for use with fast detectors such as diamond, as the wrong choice can increase the rise time of the pulse and introduce a significant amount of noise into the detector system, causing a deterioration of the timing resolution.

As the current signal from a diamond detector produces a faster and more consistent rise time than the charge signal, current-sensitive preamplifiers are generally employed for fast timing measurements. In a current-sensitive preamplifier, the current is converted into a voltage pulse using the resistance across the input terminal, R_i, which is then amplified and sent to the output terminal.

Diamond Broadband Amplifiers (DBAs) (see Figure 2.13a), specially designed by the GSI group for use with diamond, were used throughout all testing of the detectors. These preamplifiers not only provided the current-sensitive amplification required, but also a means of biasing the detectors. A circuit diagram of the DBA, which models the detector as a current generator with a capacitance, C_D, can be seen in Figure 2.13b. The bias, V_b, is applied via the 10 kΩ resistor, R_b, using a high voltage supply [18].

The DBAs have a bandwidth of 0.03 - 2.3 GHz, which means they are able to cope with pulse widths of less than 10 ns, which is typical for signals from diamond detectors [43]. If a preamplifier with a bandwidth lower than this were to be used with the diamond detectors, only lower frequency pulses could be detected by the preamplifier, i.e., those with a slower rise time and larger pulse width, which would significantly lengthen the rise time of the output signal. This would render the fast rise time of the diamond detector irrelevant, and worsen the timing resolution of the system. On the other hand, choosing a preamplifier with a rise time that is much faster than the rise time of the detector introduces additional noise into the system caused by the unnecessarily high bandwidth, once again, degrading the timing resolution [44]. It is therefore important to choose a bandwidth that is of the same order as the frequency of the signals to retain the resolution of the diamond detector.

2.5.2.1 Effects of Noise and Capacitance

Noise is a very important consideration when trying to get the best out of a timing system, as any noise found on the output of the preamplifier signal will generate signal jitter at the threshold of the discriminator (see Section 2.5.4). If the thermal noise generated in the detector circuit is expressed as a current, i_{nR_i}, as in Figure 2.13b, the noise voltage, V_n, this generates at the input of the preamplifier depends

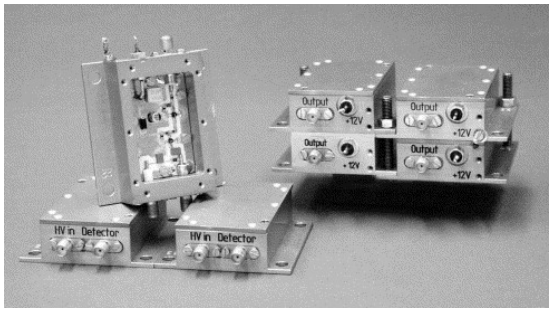

(a)

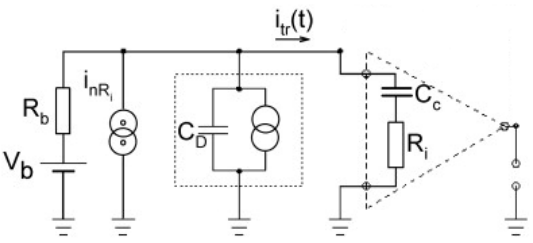

(b)

Figure 2.13: The Diamond Broadband Amplifiers shown in (a) photographic form, and (b) as a circuit diagram, which models the diamond detector as a current generator with a capacitance, C_D. The bias part of the DBA is represented by the bias circuit (V_b, R_b), the broadband amplifier by the coupling capacitor and input resistor, C_c and R_i, and the thermal noise associated with the preamplifier is shown as i_{nR_i}. Adapted from [18].

upon the impedance, Z_i, of the detector circuit. This impedance arises from the parallel connection of R_i and C_D, as well as any parasitic capacitances, C_p, that may be present in the cables and connections of the detector setup.

A detailed analysis of the effects of noise on the timing resolution of a diamond detector has been undertaken by Ciobanu *et al.* [19], and is outlined below.

If the current density of the noise at the input of the preamplifier of bandwidth, Δf, is given by $\frac{i_{nR_i}}{\Delta f}$, then the noise voltage can be expressed as:

$$V_n^2(f) = \frac{i_{nR_i}^2}{\Delta f} \cdot |Z_i(f)|^2 = \frac{i_{nR_i}^2}{\Delta f} \frac{R_i^2}{1 + f^2/f_s^2} \tag{2.5}$$

where f_s is the cut-off frequency given by $f_s = 1/2\pi R_i(C_D + C_p)$.

By integrating over all possible frequency values from 0 to ∞, and taking into account that the noise power, $i_{nR_i}^2 R_i$, can be written in terms of the temperature and the Boltzmann constant, T and k, so that $i_{nR_i}^2 R_i = 4kT\Delta f$, the noise voltage can also be expressed as:

$$V_n^2 = \frac{i_{nR_i}^2}{\Delta f} \cdot R_i^2 \cdot f_s \cdot \frac{\pi}{2} = \frac{kT}{(C_D + C_p)} \tag{2.6}$$

In order to obtain an expression which shows how the noise effects the timing resolution, σ_t, of a timing measurement, one has to consider the point at which the output signal from the preamplifier crosses the threshold of the discriminator, and the noise present on the slope of the signal, dv/dt, when this occurs. This can

generally be written as:

$$\sigma_t = \frac{\sigma_n}{dv/dt} \tag{2.7}$$

where σ_n is the noise dispersion in Volts, which can be assumed to equal the noise voltage, V_n.

If one were to rewrite equation 2.7 to allow for any affects the preamplifier has on the rise time of the signal, a more detailed expression for the timing resolution can be given:

$$\sigma_t = \frac{\sqrt{kT \cdot (C_D + C_p)}}{2.28 \cdot Q_{col} \cdot BW_A} \tag{2.8}$$

where Q_{col} is the charge collected by the diamond detector, and BW_A is the frequency bandwidth of the preamplifier. Further details of the derivation of this equation can be found in [19].

The bandwidth dependence on the noise contribution that was mentioned previously in this section can be seen mathematically in equation 2.8, but most importantly, this equation emphasises the importance of the total capacitance of the detector setup. Reducing the detector capacitance by, for example, electrically segmenting the contact to effectively create a capacitor with a smaller plate area can greatly reduce the noise associated with the signal from the preamplifier, and significantly improve the timing resolution. It is also important to keep the parasitic capacitances to a minimum by restricting the cable length between the detector and the preamplifier.

2.5.3 Signal Attenuation

The choice of cable to be used between the diamond detector and the preamplifier is an important one, not only because of the implications from the parasitic capacitances in the cable, but also because of the attenuation and distortion of the pulse shape becomes substantial at high frequencies and must be controlled to ensure that the fast rise time of the signal does not become degraded.

All cables experience some type of signal loss caused by leakage through the dielectric or resistance in the central conductor metal but this loss is exaggerated for high-frequency signals like those from a diamond detector. It is therefore necessary to choose cables with very low attenuation values at 1 GHz, the frequency of a typical pulse from a diamond detector, and try to minimise the length of the cable

used between detector and preamplifier.

The cables chosen for use at both optimisation experiments as well as LYCCA-0 commissioning were RG-316 coaxial cables, which had an attenuation of 93.8 dB/100 m at 1GHz, the lowest attenuation value available for a flexible coaxial cable. This means that a signal with a pulse height of 500 mV is attenuated to around 450 mV after 1 m of RG-316 cable. The output height, V_{out}, of an attenuated signal can be calculated using the following equation:

$$A = 20 \log \left(\frac{V_{in}}{V_{out}} \right) \tag{2.9}$$

where A is the attenuation over the length of cable and V_{in} is the pulse height of the input signal.

2.5.4 Signal Walk and Jitter

The digital time that enters the data stream, known as the pick-off time, is determined from the leading edge of a logic pulse created by a discriminator. This logic pulse is generated when the rising edge of the output signal from the preamplifier crosses the threshold level of the discriminator, which can either be at a fixed voltage or a fixed fraction of the total pulse height, depending upon the type of discriminator used (see sections 3.1.3.1 and 3.1.3.2 for more details). Signal fluctuations and variations between signals at the threshold level introduce two sources of uncertainty into the pick-off time that are described as signal walk and jitter.

Signal walk can arise from variation in the amplitude or rise time of the amplified signals. For diamond detectors, the rise times are found to be fairly consistent, however, due to the polycrystalline structure of the diamond wafers, the amplitude of a signal is rarely the same from pulse to pulse. If two coincident pulses of equal rise time but differing pulse height were to enter a discriminator using a fixed voltage threshold level, the pulse with the greater amplitude would reach the threshold voltage before the lower amplitude pulse, generating an earlier logic pulse [45]. This difference in the logic pulse generation is the signal walk, as is shown schematically in Figure 2.14. Signal walk associated with diamond detectors can be minimised by using single-crystal diamond wafers, as they produce signals that are much more uniform in amplitude, but this is not feasible for a large area detector such as the one required for LYCCA. Fortunately, the time difference between two pulses of different amplitudes is still small if the signal rise times are as fast as those of a diamond detector.

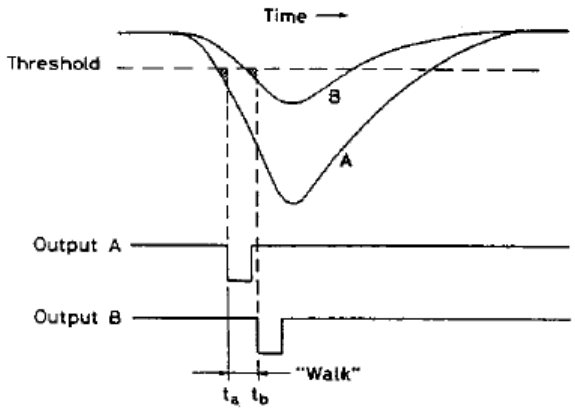

Figure 2.14: Schematic diagram showing the signal walk associated with two coincident pulses of equal rise time but differing pulse height. A discriminator using a fixed voltage threshold is shown. [45]

Noise and statistical fluctuations on signals entering a discriminator mean that two coincident signals with identical rise times and pulse heights may not generate a logic pulse at exactly the same time. This effect is known as jitter and can be seen in Figure 2.15. Jitter may be caused by noise from electrical components in the detector circuit or the preamplifier, as was mentioned in Section 2.5.2.1, or it may arise from the diamond detector itself. The quantum nature of the charge carriers in the detector means that any statistical variation in the number of electrons and holes collected can be seen on the output signal of the detector. This is only the case for low amplitude signals where few charge carriers are produced in the diamond detector.

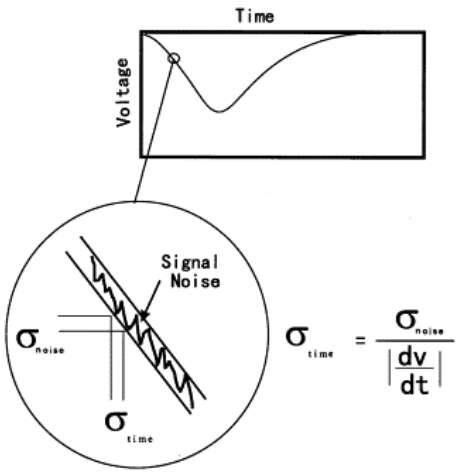

Figure 2.15: Diagram showing jitter about the discriminator threshold level, which arises from noise and statistical fluctuations on a signal. [46]

It is important to be aware of what aspects of the detector setup, including the detector signal, cables and electrical components, contribute to the jitter and walk of a signal, and optimise these as much as possible. The best timing resolution can only be acquired when these aspects are under control.

CHAPTER 3

Detector Optimisation Experiments

As with every development project, it was necessary to undertake a number of optimisation experiments in order to fully understand how the detector responded in certain situations. The optimisation tests for the diamond detectors focused on obtaining the best possible timing resolution by varying factors such as the detector capacitance and contact material, as well as other electronic considerations like bias, signal discrimination methods and cabling. These optimisation experiments took place at two facilities, the Cyclotron Institute at Texas A & M University (TAMU) and the Nuffield Cyclotron at the University of Birmingham.

3.1 Experiments at Texas A & M University

3.1.1 Beam Selection

The MARS (Momentum Achromat Recoil Spectrometer) separator, situated at the Cyclotron Institute at TAMU, was used to filter recoils generated at the MARS target chamber in order to produce a secondary beam [47]. An Electron Cyclotron Resonance (ECR) ion source injects highly charged heavy ions into the K500 cyclotron which can accelerate fully stripped N=Z ions up to 80 MeV/u [48].

Before entering MARS, the accelerated heavy ions are extracted from the K500 and hit a cryogenically cooled gas target. Transfer reactions using inverse kinematics occur within the gas target, generating a large number of different recoils. Stripper foils and degraders can be placed before and after the gas target to adjust the energy of the recoils to the required beam energy.

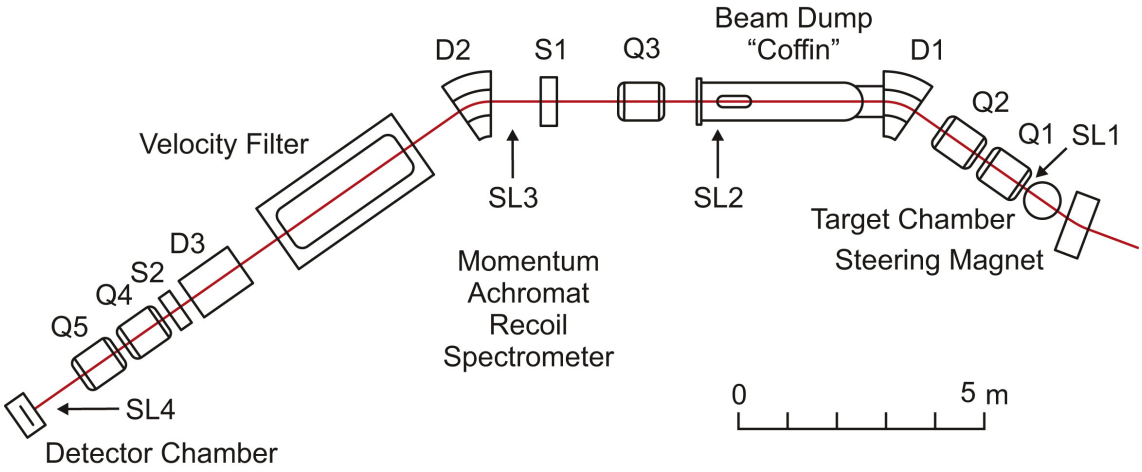

Figure 3.1: Schematic layout of MARS showing dipole, quadrupole and sextupole magnets (D,Q,S respectively), and slits indicated by SL [49].

MARS uses a combination of dipole, quadrupole and sextupole magnets to disperse, select and refocus the recoils to create a secondary beam with as few contaminants as possible. A schematic diagram of MARS can be seen in Figure 3.1. The combination of quadrupole and dipole magnets allows an achromatic beam with the same p/q ratio to enter the velocity filter, which uses perpendicular electric and magnetic fields to select the desired recoil. From this point, the beam is focused and can then be used for secondary reactions.

3.1.2 Experimental Setup

The diamond detectors were mounted in a vacuum chamber at the end of MARS so that the secondary beam hit the centre of the diamond wafers. As can be seen from the schematic diagram in Figure 3.2a, two diamond detectors were positioned 14.5 mm apart in a transmission geometry so that the beam could pass through the first detector and stop in the second detector. Secondary beams of 33.5 MeV/u ^{40} Ar and 20.8 MeV/u ^{20}Ne were chosen to imitate the kind of energy deposition expected from experiments at GSI, whilst being sufficiently different from one another to observe any effects energy deposition may have on the timing resolution. Energies of 610

MeV and 730 MeV were deposited in the front and back detectors respectively for the ^{40}Ar beam, whereas the ^{20}Ne beam deposited lower energies of 367 MeV and 49 MeV in the front and back detectors respectively. All energy loss calculations were made using the ATIMA code [50].

As can be seen in Figure 3.2b, each of the detector PCBs contained two 20 mm x 20 mm x 0.3 mm polycrystalline diamond wafers, the topmost of which had an Al contact whilst the lower wafer had a Au contact. Different contacts were used to compare the performance of the contact material under the same experimental conditions. The beam could be focused onto the centre of either wafer by adjusting the height of the detector mount using Al blocks.

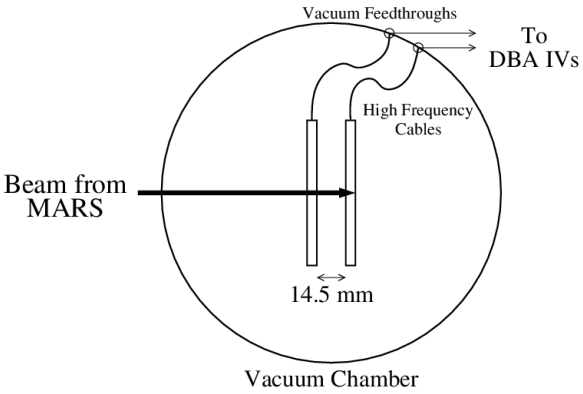

(a) Schematic diagram showing the experimental setup for tests at TAMU.

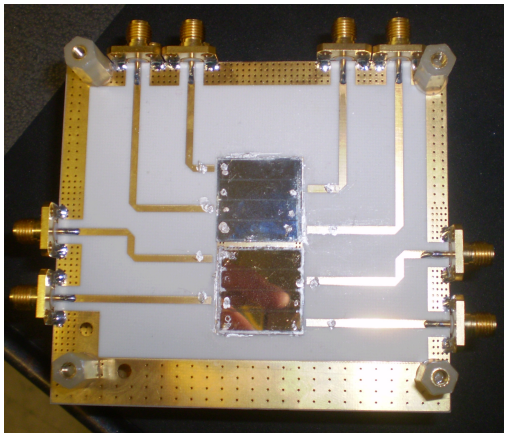

(b) The diamond detectors were positioned in a transmission geometry with two diamond wafers attached to each detector.

Figure 3.2: Experimental setup at TAMU

The contacts were segmented into four 18 mm x 5 mm strips (see section 2.4.3 for more details), each with its own impedance-matched track on the specially designed, two-layer PCBs. Both the PCBs and the cables used in the TAMU setup were chosen to cope with the fast, high frequency signals that are produced by the diamond detectors.

The coaxial cables used to carry the signals from the PCB to the vacuum feedthroughs and then to the DBA IV preamplifiers have low attenuation (93.8 dB at 1 GHz) compared with most other coaxial cables, which means that the signal loses as little height as possible before it reaches the DBAs to be amplified. This is particularly important for polycrystalline diamond as trapping in the grain boundaries means that the charge collection efficiency is greatly reduced, which has

a direct impact on the height of the current signal.

3.1.3 Setup of Electronics

Along with observing how the energy deposition and contact metallisation affects the timing resolution of the diamond detectors, one of the main reasons behind testing the detectors at TAMU was to become more familiar with the electronics used to process the timing signals. Signal discrimination methods and detector biases were varied to observe the effect this had on the timing resolution. The TAMU tests were also the first opportunity to use the Caen V1290A TDC (Time to Digital Converter)[51] with the diamond detectors.

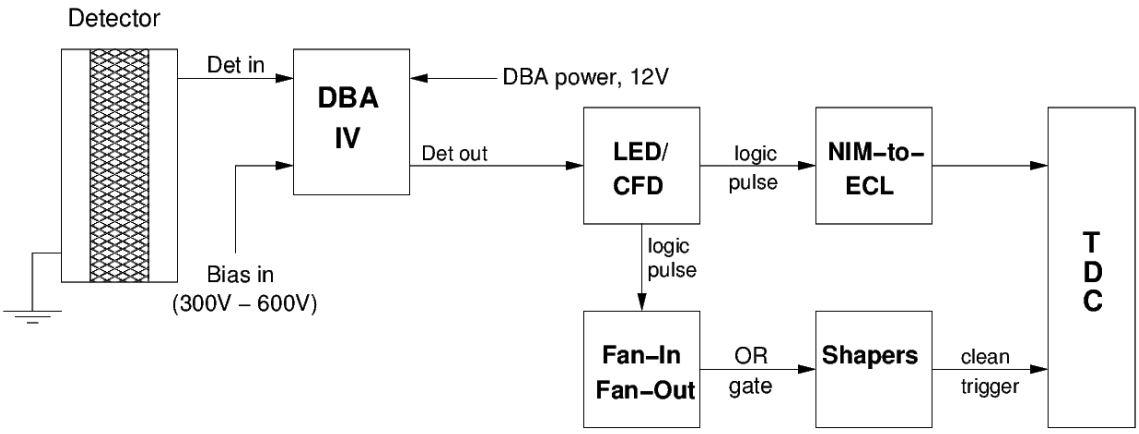

Figure 3.3: Schematic diagram of the electronic setup used to process the timing signal after the DBA IV preamplifiers

A schematic diagram showing the setup of the timing electronics used at TAMU is shown in Figure 3.3. Variable high voltage (HV) supplies were connected to the bias input of each DBA preamplifier, which supplied voltages of between 300 V and 600 V across each strip of the detectors. These voltages were changed manually between experimental runs. The power supplied to the DBAs to operate them also determined the gain of the preamplifiers. For the TAMU tests, and all other experiments undertaken using the diamond detectors, an operating voltage of 12 V was used, which produced the maximum possible gain of 50 dB.

The amplified signals were then sent to either a leading edge discriminator (LED) or a constant fraction discriminator (CFD) in order to produce a fast logic pulse (see sections 3.1.3.1 and 3.1.3.2). This logic pulse was then converted from the NIM (Nuclear Instrumentation Module) standard into an ECL (Emitter-Coupled Logic) signal, which could be read in by the TDC. A second copy of the NIM logic

pulse from the discriminators was also sent to a Fan-In Fan-Out module which created an OR gate of all discriminator channels. In order to obtain a clean trigger for the TDC, this OR gate signal was shaped and delayed by a number of other modules before reaching the trigger input of the TDC and initiating data collection.

3.1.3.1 Leading Edge Discrimination

A leading edge discriminator reads in the analogue voltage pulse and compares this pulse with a threshold voltage that has been set by the user. When the leading edge of the input pulse reaches this threshold value, the discriminator generates a logic pulse, which only ends when the trailing edge of the input pulse reaches a voltage below the threshold voltage [52].

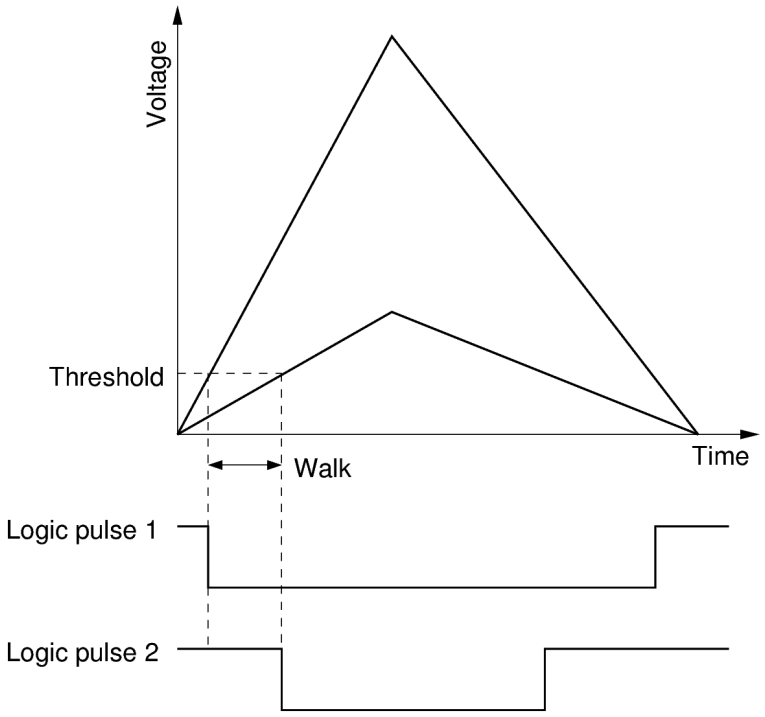

Figure 3.4: Operation of a leading edge discriminator. Signal walk is introduced for different pulse heights, and can be reduced by lowering the threshold to just above the noise.

The sharp leading edge of this logic pulse defines the arrival time of the input pulse, making the arrival time completely dependent upon when the input pulse crosses the threshold. This can become problematic if the input pulse has a variation in signal height, as it introduces signal walk into the timing measurement. In order to reduce this effect as much as possible, the threshold voltage is set to just

above the noise level so that the signal walk (see section 2.5.4) is reduced, but without generating spurious timing measurements when noise crosses the discriminator threshold. The operation of a leading edge discriminator is illustrated in Figure 3.4.

The noise level during the majority of the TAMU experiment was found to be 30 mV, so LED thresholds of 30 mV, 40 mV and 50 mV were used in separate runs to ascertain whether the threshold setting influenced the timing resolution of the diamond detectors.

3.1.3.2 Constant Fraction Discrimination

Constant fraction discrimination should eliminate any signal walk associated with signal height variation by setting the voltage threshold at a particular fraction of the signal height, rather than a constant voltage value. The logic pulse in a constant fraction discriminator is constructed using the algorithm as demonstrated in Figure 3.5.

The input pulse is divided into two parts. The first part is inverted and attenuated to a fraction, f, of the original pulse height, whereas the second part is delayed by a time t_D. The optimum t_D is given as the time taken for the pulse height to increase from the fraction, f, to its full peak height. Combining these two signals results in the bi-polar constant-fraction pulse with a zero-crossing point at a particular fraction of the original pulse height. If every input pulse is attenuated and delayed by the same amount, this zero-crossing point should always correspond to the same fraction, f, of the pulse height. The CFD forms the logic pulse at the zero-crossing point of the bi-polar signal [45].

The CFD method described above works extremely well for signals with identical rise times, however, if the rise times and shapes of pulses vary slightly, it is better to use a smaller t_D so that the zero-crossing occurs toward the beginning of the pulses where the variation is less.

3.1.3.3 Time to Digital Converter (TDC)

It is important to make sure that the dominating factor in the timing resolution does not come from the electronics, and for this reason, the fastest electronics available should be used. The Caen V1290A TDC can record timing signals with a 25 ps dispersion in its "Very High Frequency Mode ", the fastest available at the time of purchase [51]. This dispersion is achieved by multiplying the internal 40 MHz clock up to 320 MHz, and using precisely calibrated delay lines for multiple sampling of

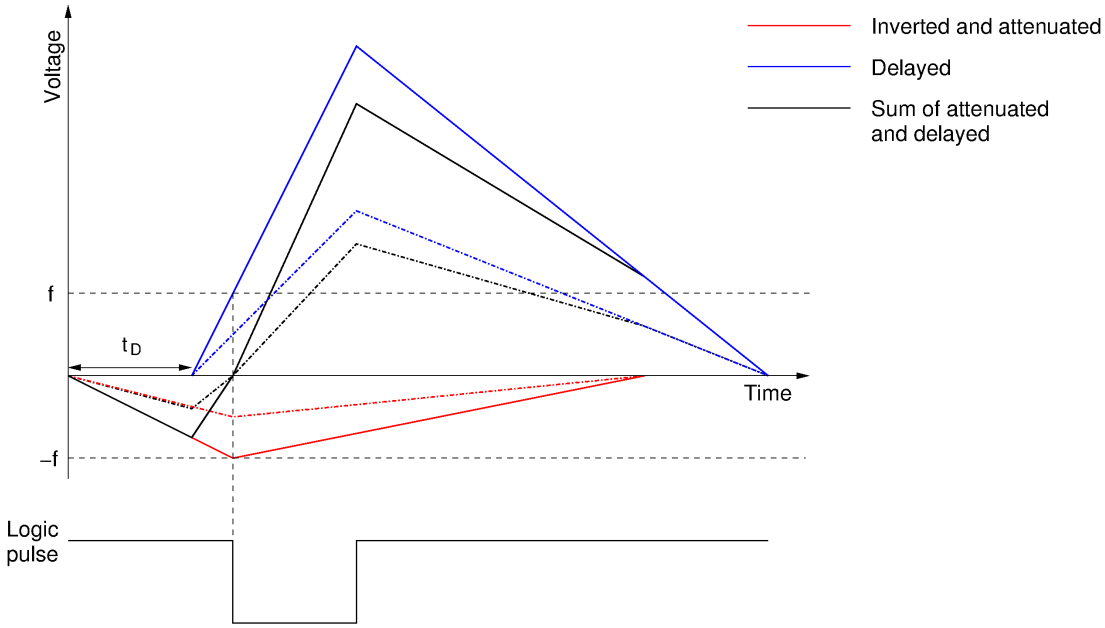

Figure 3.5: Operation of a constant fraction discriminator. The solid line and dash-dot line represent two pulses of different pulse height to show how the zero-crossing always occurs at the same point.

the signals.

The TDC acquired data using a trigger matching mode, a schematic of which can be seen in Figure 3.6. Whenever a timing signal reaches the TDC, the time of the signal with respect to the internal clock cycle is stored in the buffer of the TDC. As soon as a trigger signal is received, the TDC begins searching for hits stored in the buffer within a programmable window. For the TAMU tests, the window offset was set to -375 ns (looking backwards in time), with a match window width of 375 ns. Any hits recorded by the TDC that are outside of this window are rejected as they are not considered to be in coincidence with the trigger signal.

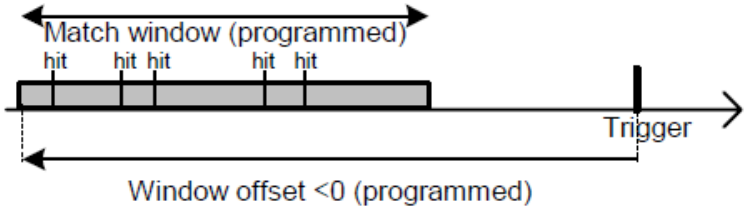

Figure 3.6: Schematic diagram of the TDC trigger matching mode. The TDC looks backwards in time after receiving the trigger input.

3.2 Experiments at the University of Birmingham

Whereas the experiment undertaken at Texas A & M University focused purely on the timing resolution of the diamond detectors and the fast timing electronics, the experiment at the University of Birmingham's Nuffield cyclotron was undertaken to gain a better fundamental understanding of how the diamond detector works. Pulse shapes were analysed during this experiment to observe the effects of changing the capacitance and contact material on the rise times and pulse heights of the diamond signals.

3.2.1 Experimental Setup

A 50 MeV-^{3}He beam, the most energetic available from the cyclotron, was scattered from a Pb target positioned at the centre of a vacuum chamber. Two pairs of diamond detectors were used in this experiment, the first fabricated at the University of Surrey and the second fabricated by Diamond Detectors Ltd (DDL). Both detector pairs were placed in a transmission geometry at angles of 45° and 75° from the beam direction respectively. A top-down view of the setup can be seen in Figure 3.7.

The Surrey detectors consisted of two polycrystalline diamond wafers (one for the front detector and one for the back) measuring 20 mm x 20 mm x 0.3 mm. The contacts fabricated for these detectors were segmented into four pads of differing area, see section 3.2.3 for more details. These wafers were affixed to the same impedance-matched PCBs that were used at TAMU, and signals were taken from the detectors using the same high frequency cables, as these were found to perform well in the previous experiment. The detectors fabricated at DDL used polycrystalline diamond wafers measuring 10 mm x 10 mm, with thicknesses of 220 μm and 150 μm. Unlike the Surrey detectors, the contacts for these detectors, specially designed by DDL, were not segmented and had an active area of around 8 mm x 8 mm.

The low energy scattered beam deposited around 20 MeV in both front and back detectors, considerably less than the energy deposition in the TAMU experiment. Consequently, the pulse heights generated by the diamond detectors were typically only tens to hundreds of mV after amplification.

Preamplification was once again performed by the DBA IV preampliers, and the signals were then either processed by the electronics shown in Figure 3.3 and acquired by the TDC, or acquired by an oscilloscope directly after amplification.

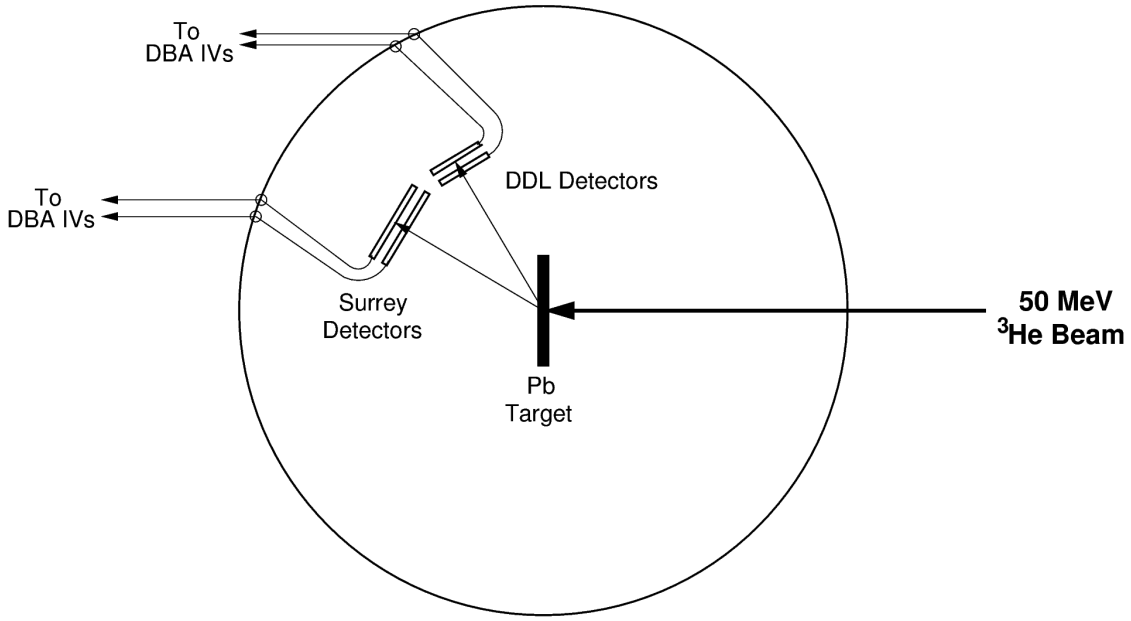

Figure 3.7: Schematic diagram showing experimental setup at the University of Birmingham and the position of the diamond detectors fabricated at the University of Surrey, and those fabricated at DDL.

3.2.2 Pulse Shape Acquisition

Pulse shapes were acquired after amplification by the DBA IVs using 2.5 GHz oscilloscopes so that variations in rise time and pulse height could be analysed. Long coaxial cables carried the amplified signals from the experimental area to the control room and one of two oscilloscopes. This was done alongside TDC acquisition so that timing resolutions could also be obtained.

Each oscilloscope gathered signals from one pad on a front detector and the corresponding pad on the back detector. This was done to correlate the two signals so that a timing measurement could be made if necessary. Runs were repeated until pulse shapes from all pads on the Surrey detectors and both DDL detectors had been acquired at bias voltages of 400 V, 500 V and 600 V.

3.2.3 Test for Capacitance Dependence

In order to test for any capacitance dependence on the rise time and timing resolution of the diamond detectors, pads of differing area, corresponding to different detector capacitances, were fabricated onto the diamond wafers. The largest pad, pad A, measured 18 mm x 5 mm, the same size as the strips used in the TAMU experiment. Pad B had an area about half that of pad A, pad C an area half that of pad B,

and so on. A photograph of the diamond contacts is shown in Figure 3.8, and the dimensions of each of the four pads are given in table 3.1.

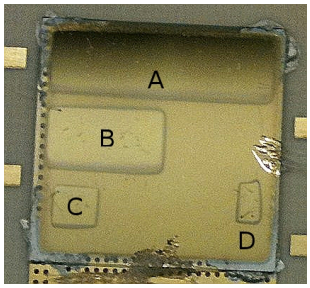

Figure 3.8: Photograph showing the layout of the pads on the diamond contacts used in Birmingham experiment.

Pad	**Dimensions (mm)**	**Pad Area (mm^2)**	**Capacitance (pF)**
A	18 x 5	90	14.6
B	10 x 5	50	8.1
C	4 x 3	12	1.9
D	2 x 3	6	1.0

Table 3.1: Contact pad dimensions, pad area and corresponding capacitance for diamond detectors used in Birmingham experiment. The capacitance of the pad is directly proportional to the pad area.

The capacitance, C_D, of a detector is described by the following equation:

$$C_D = \frac{\varepsilon_r \varepsilon_0 A}{d} \tag{3.1}$$

where ε_r and ε_0 are the relative permittivity of diamond ($\varepsilon_r = 5.5$ [53]) and the permittivity of free space respectively, A is the area of the detector and d is the detector's thickness.

Each of the four pads can be treated as an individual detector as they are electronically isolated from one another, however, they will each have exactly the same ε_r and d values because they are placed on the same wafer of diamond. This means that the capacitance described in equation (3.1) becomes directly proportional to the pad area.

3.2.4 Test for Contact Material Dependence

Although the main aim of the Birmingham experiment was to test for capacitance dependence, the opportunity to investigate detector performance with different con-

tact materials also came about through links with Diamond Detectors Ltd. The development group at DDL had produced at new type of contact, which uses a diamond-like carbon layer between the diamond wafer and a top layer of gold, and were keen to promote it. See Section 2.4.3.2 for more detail.

The diamond-like carbon contact developed at DDL was designed to enhance the electrical transport through the material. Recent research has found that increasing the concentration of sp^2 bonding in diamond-like carbon also increases the number of localised states formed by an overlap of the energetic bands. Electrons are able to hop between these localised states, travelling through the otherwise insulating material [54]. The similarities in structure between the polycrystalline diamond wafer and the diamond-like carbon mean that it is far easier to form an ohmic contact between the two surfaces, further encouraging the transport of electrons from diamond to the contact. The combination of these properties culminates in greater charge collection by the contacts, which leads to larger pulse heights.

The contacts used for the Surrey detectors consisted of a 100 nm layer of Au applied directly onto the diamond wafer. The rise times, pulse heights and timing resolution were compared, after taking account of differences in capacitance, in order to determine whether inserting the diamond-like carbon interface between the diamond wafer and Au layer improves the performance of the diamond detectors.

CHAPTER 4

LYCCA-0 Commissioning Experiment

The diamond detectors were brought together with the rest of the LYCCA detectors for the very first time in September 2010 to take part in the commissioning experiment of the LYCCA-0 array, the first prototype of LYCCA. The aim of the commissioning experiment was to successfully synchronise all of the LYCCA detectors and demonstrate the capabilities of the array. This chapter will outline the experimental setup of the commissioning experiment, which took place at GSI with the aid of the FRagment Separator (FRS). The different LYCCA-0 detectors shall also be described in detail, and an explanation of the fragment identification procedure using LYCCA-0 shall be given.

4.1 The PreSPEC Campaign

PreSPEC is the precursor campaign to HISPEC, the high-resolution in-beam gamma-ray spectroscopy project that will use fragments from the Super-FRS at FAIR and the high resolution AGATA Ge array to study the structure of exotic nuclei. This first campaign of experiments made up the commissioning phase of LYCCA-0, which used the existing FRS and RISING Ge array [4] situated at GSI.

The first experiments of the PreSPEC campaign were performed using well known secondary beams in order to establish the performance of LYCCA-0. Once LYCCA-0 had proven to work effectively, further experiments which focused on discovering new physics, such as the origin of mixed-symmetry states in N=52 isotones and coulomb excitation of isotopes in the ^{100}Sn region [55], were undertaken. This thesis only addresses the very first experiment of the PreSPEC campaign, which concentrates on the proof-of-principle study of LYCCA-0.

4.2 The FRS

4.2.1 Beam Production and Selection

At GSI, ions are accelerated and stripped of their electrons using the UNILAC linear accelerator and the SIS 18 synchrotron. This combination can accelerate ions up to 90% of the speed of light, and the variety of ion sources available at GSI allows primary beams of hydrogen up to uranium to be produced. A multitude of other stable and radioactive beams can be produced through fragmentation of these accelerated ions by bombardment with a thick production target. In the case of the first LYCCA-0 commissioning experiment, $^{64}Ni^{26+}$ ions were bombarded onto a production target of ^{9}Be at an energy of 550 MeV/u in order to produce ^{63}Co as a fragmentation product, along with many other nuclei.

The presence of so many different fragmentation products makes it difficult to perform experiments and consequently, the FRS is required to separate these fragments so that only the desired nuclei are sent to the experimental area. The FRS uses four dipole magnets, each with a set of focusing quadrupole magnets placed before and after (see Figure 4.1). Four focal planes, F1 to F4, are defined between the quadrupole magnets, where various degrader and slit systems are situated, as well as a number of auxiliary detectors that are used for fragment identification (see section 4.2.2).

The FRS uses a Bρ-ΔE-Bρ method to separate the fragments, where a mass-to-charge ratio, A/Q (where Q=Z for fully-stripped ions) selection is made using the first two dipole magnets. This selection means that only a small range of ions with a magnetic rigidity (Bρ) similar to that of the desired fragment are able to hit the centre of the degrader. All other ions are lost as they pass through the magnets, or hit the slits placed before the degrader. Further selection is then required to separate the desired fragment from its A/Q counterparts, which is achieved using

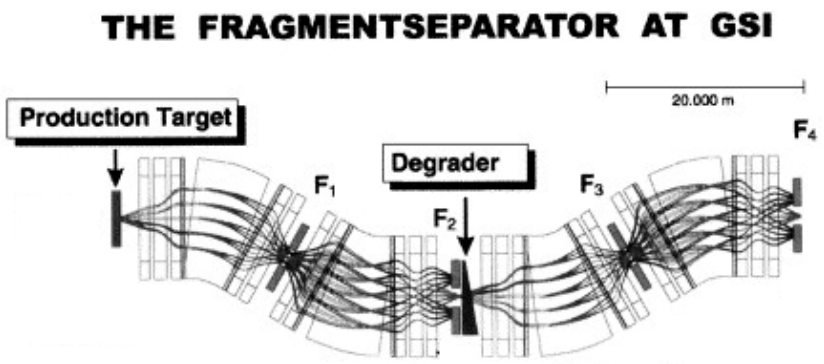

Figure 4.1: Schematic diagram showing the path of different ions through the FRS. The larger, curved dipole magnets are bordered either side by quadrupole magnets which focus the ions to form focal planes F1 to F4. The effects of degraders and slits can also be seen at F2 and F4. Adapted from [56]

the degrader. The energy loss of a fully stripped ion depends on its proton number, which means that each different species of fragment passing through the degrader will lose a different amount of energy and will exit the degrader with a different momentum. Selection of the desired fragment can then be made using the final two dipole magnets by exploiting these momentum differences [57]. Fragment selection can be changed by altering the magnetic fields of the dipole magnets.

Two fragment selections were used during the commissioning experiment, a ^{64}Ni selection, which was also the primary beam, and a ^{63}Co selection. The energy of the first ^{64}Ni secondary beam was varied for calibration purposes by changing the thickness of the degrader at the F2 focal plane. A second degrader could also be inserted into the beam line at the F4 focal plane to lower the secondary beam energy further.

4.2.2 Auxiliary Detectors

Even with accurate magnet, degrader and slit settings, it is still possible to get contaminants in the secondary beam. It is therefore necessary to use a number of auxiliary FRS detectors to distinguish between the desired secondary beam and any unwanted fragments. These detectors are also required during tuning of the FRS magnets to ensure that the correct secondary beam is selected. Energy loss, time-of-flight (ToF) and position measurements are performed using MUSIC (MUltiple Sampling Ionisation Chamber), scintillators SC21 and SC41, and TPCs (Time Projection Chamber) respectively. These three detector systems are described in the following subsections.

4.2.2.1 MUSIC

MUSIC is a gas-filled detector used to measure the energy loss of an ion. As an ion passes through the chamber, the CF_4 counting gas becomes ionised, generating electron clouds inside the detector and causing the ion to lose energy. The clouds of electrons drift toward the eight positively biased anode strips (see Figure 4.2), generating a pulse whose height is directly proportional to the number of electrons produced by the ionisation process. A larger signal height corresponds to greater energy loss.

A Frisch grid is used to screen the anode strips from the positively charged ions in the detector and eradicate any dependence of the pulse height on the interaction position in the chamber. This is done by holding the Frisch grid at a bias value between that of the cathode and anode so that the electrons are initially attracted toward the grid before continuing on to the anode. Charge is only induced on the anode by electrons travelling between the Frisch grid and the anode, meaning that the signal height has no position dependence and is directly related to the number of electrons produced in the ionisation event [30].

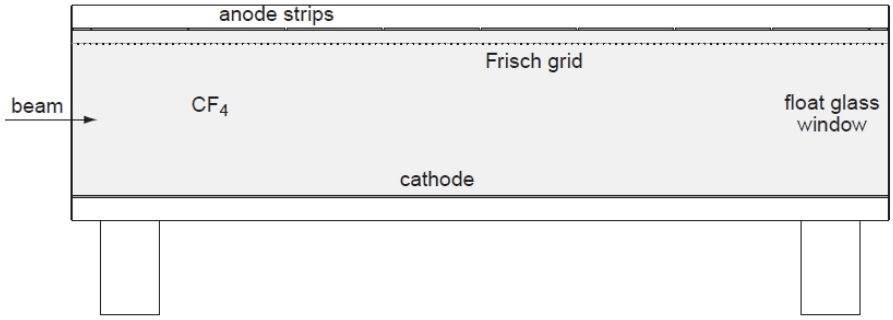

Figure 4.2: Diagram showing the operation of the FRS MUSIC detectors. [58]

4.2.2.2 FRS Scintillators

The FRS uses two plastic scintillators for ToF measurements. The first scintillator (SC21) is positioned at the F2 focal plane, and the second (SC41) is position around 35 m downstream at the F4 focal plane. The photons produced by the plastic scintillating material are collected by two photomultiplier tubes (PMTs) situated to the left and right of the scintillator. In order to account for any deviation in a particle's flight path from the centre of the beam axis, ToF measurements are made using the left PMTs and right PMTs separately and the final ToF measurement is found by averaging these. Position measurements can also be made by measuring

the time difference between left and right PMT signals of the same scintillator [59]. The large flight path between the two scintillators allows for clear differentiation between the ToF measurements of nuclei with neighbouring masses.

4.2.2.3 TPCs

Tracking of the nuclei through the FRS is carried out by Time Projection Chambers (TPCs) installed at the F2 and F4 focal planes. The principle of the TPC is similar to that of MUSIC, a TPC once again uses the ionisation process to generate electron clouds inside a gas-filled chamber. A schematic diagram of a TPC is shown in Figure 4.3. A uniform electric field is created inside the drift volume by applying high negative voltages to the cathode and Mylar strips surrounding the chamber, causing the electrons to drift toward the four anode wires placed at the bottom of the TPC. The anode wires are partially surrounded by C-pad cathodes, each of which is connected to one of two delay lines and increases the delay by 15 ns from the neighbouring C-pad. An electron avalanche occurs near the anode wires, increasing the amount of charge induced on the C-pads and producing a larger signal.

The vertical position, or y-position, of any particle interaction is determined by measuring the time taken for electrons to drift to the anode wires. Four separate drift time measurements are made, one from each of the four anode wires. The time difference between the delayed signals arriving at the left and right of the delay lines is used to evaluate the x-position of an interaction. Two measurements of the x-position are made, one from each delay line. As four y measurements and two x measurements are taken for every interaction, this helps to reduce the noise and erroneous signals in the TPC [60].

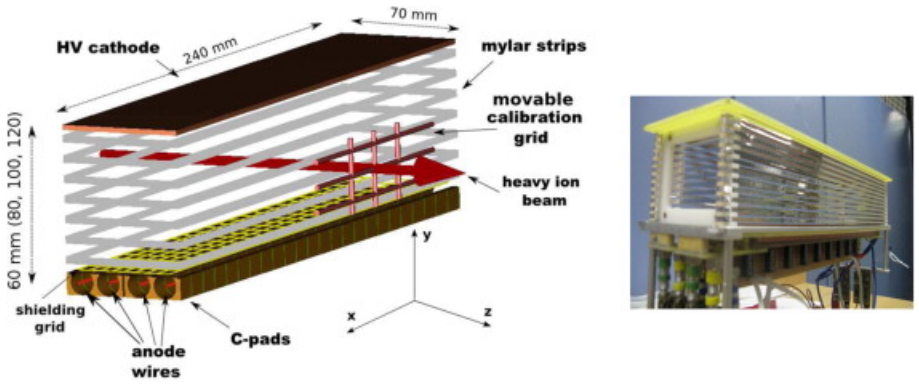

Figure 4.3: Diagram of a Time Projection Chamber (TPC) used for tracking nuclei through the FRS.[60]

4.2.3 Fragment Identification

The clearest way to identify and distinguish between the cocktail of fragments travelling through the FRS is to use a two-dimensional Z versus A/Q plot, which groups fragments of the same species into areas of greater intensity. Two examples of such a plot are shown in Figure 4.4. Each region of intensity corresponds to a different fragment, with isotopes running horizontally across the plot.

The proton number, Z, is determined from energy loss measurements taken by MUSIC, as the energy loss of an ion is directly proportional to the square of its charge. A combination of ToF and Bρ measurements are required to determine the mass-to-charge ratio, A/Q, of each ion. Magnet settings such as the B-fields, dispersion and magnification can be used, along with x-position measurements, to calculate individual Bρ values for each ion.

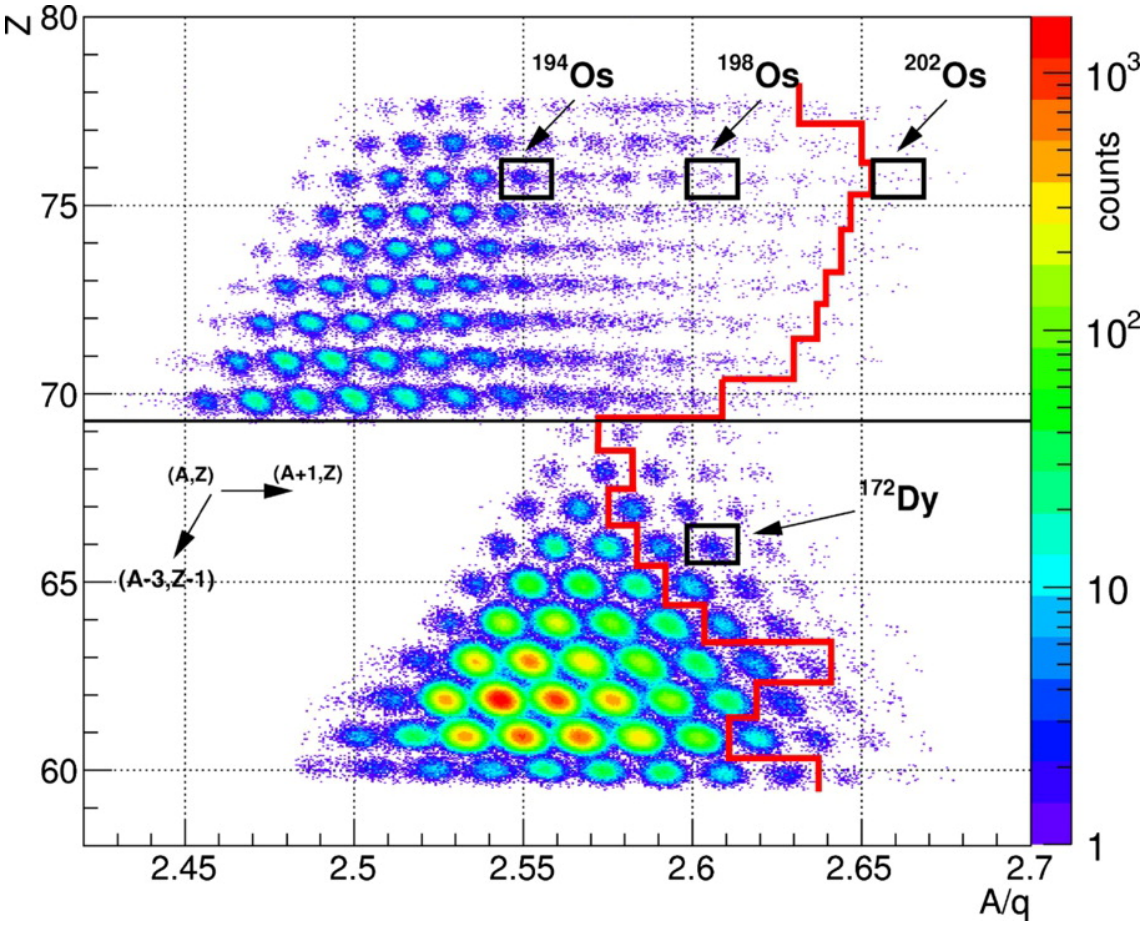

Figure 4.4: Two examples of a Z versus A/Q plot used to identify different fragments travelling through the FRS. Each region of high intensity corresponds to a different species of fragment. [61]

If fragments of the same species pass through the FRS and encounter the same magnetic field, detectors, degraders etc., one could naively think that the energy loss and ToF measurements would always be exactly the same for each fragment. More often than not, a variation in these measurements is introduced due to energy-loss and angular straggling, which occurs when ions pass through any matter in the beam line, as well as the intrinsic resolution of the detectors. These factors give the regions in Figure 4.4 a measurable Gaussian width.

4.3 The LYCCA and LYCCA-0 Arrays

The production of the final LYCCA array can be divided into four main stages, with each stage involving physics experiments and in-beam tests to build on experience gained from the previous stages [9]. The first stage involved in-beam tests of the individual DSSSD-CsI LYCCA modules, which were successfully undertaken using the Tandem accelerator at the University of Cologne [62]. Stage 2, the current stage, is the implementation of the first LYCCA prototype, LYCCA-0. This stage builds upon the first stage by including a further 11 DSSSD-CsI modules as well as introducing a diamond ToF start detector and fast plastic scintillator ToF detectors. The PreSPEC campaign runs throughout this second stage of production.

The number of DSSSD-CsI modules will increase further during stage 3 and LYCCA-0 will move to the Low-Energy Cave at the Super-FRS. The size of the stop ToF position detector shall be increased at this stage, and upgrades will continue until the full array of modules has been built. The full LYCCA array will be implemented at stage 4, during which the HISPEC campaign will run. It is currently projected that this stage will be reached in 2022.

4.3.1 Structure of the Arrays

As was alluded to in the previous paragraph, both LYCCA and the LYCCA-0 prototype are modular arrays that can be arranged into a number of different configurations to suit different experimental scenarios. LYCCA-0 currently consists of 12 modules, and more will be added over time until the final number of 26 modules is reached for the full LYCCA array. These modules make up the LYCCA wall which is positioned approximately 3.6 m downstream of the secondary target. Another set of detectors, known as the target detectors, are positioned just a few centimetres behind the secondary target. A schematic view of the positions of the LYCCA

detectors along the beam line is shown in Figure 4.5

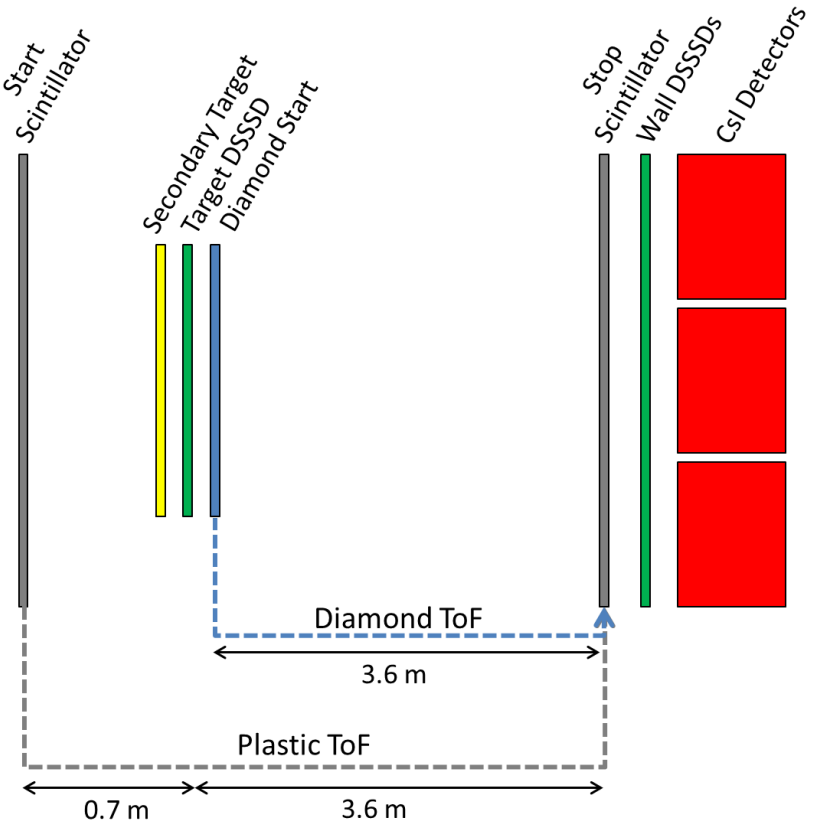

Figure 4.5: Positions of the LYCCA detectors along the beam line. The detectors are separated into two groups, the target detectors, positioned close to the secondary target, and the wall detectors, positioned around 3.6 m downstream. The diagram also illustrates the two different ToF options used during the experiment, the plastic ToF which measures between the start and stop scintillators, and the diamond ToF, which measures between the diamond start and stop scintillator.

A single LYCCA module measures 63 mm x 63 mm and is made up of a DSSSD mounted directly in front of 9 CsI crystals for energy loss and residual energy measurements respectively (see Figure 4.6a). Each LYCCA module is held in place inside the vacuum chamber by a grid-like housing structure, shown in Figure 4.6b, which can hold up to 26 modules in various configurations. A central 3 x 4 grid configuration of 12 modules was chosen for the commissioning of LYCCA-0. The final wall detector is a fast plastic scintillator used as the stop detector of both ToF timing options for LYCCA-0. The scintillator is placed inside the LYCCA vacuum chamber, directly ahead of the LYCCA modules. Further details of the fast plastic

scintillators are given in section 4.4.

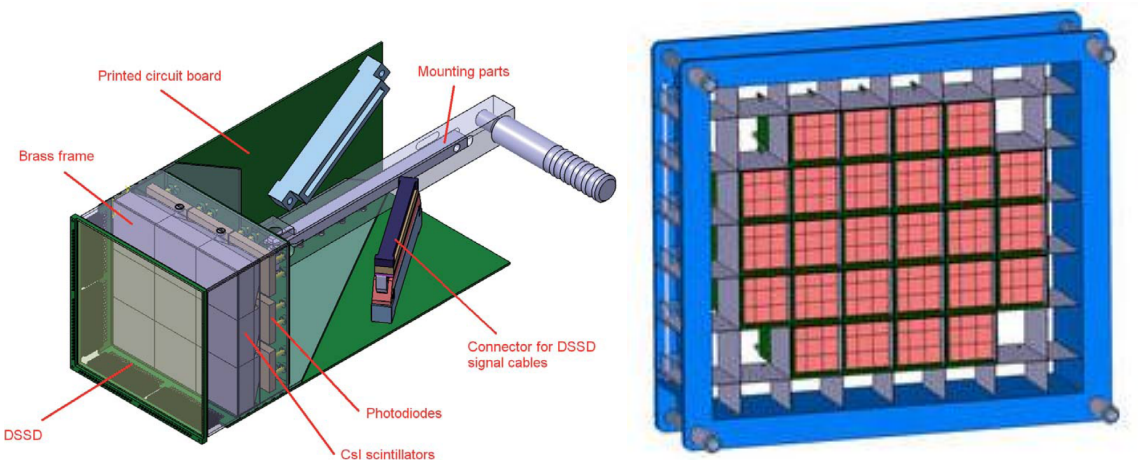

(a) A single LYCCA module

(b) Holding structure which houses up 26 LYCCA modules.

Figure 4.6: Technical drawings of (a) a single LYCCA module, which consists of a DSSSD mounted directly in front of nine CsI crystals, read out by photodiodes [62], and (b) the holding structure, which houses up to 26 LYCCA modules.

For the first commissioning experiment, the target detectors consisted of a DSSSD, identical to those used in the LYCCA wall, and a diamond detector which contained 6 diamond wafers. A fast plastic scintillator was also positioned ∼70 cm upstream of the secondary target. As can be seen in the photograph in Figure 4.7, both DSSSD and diamond detector were attached to the same mount, which was subsequently fastened onto the secondary target ladder to ensure that the secondary target, DSSSD and diamond detector were correctly aligned with one another. A 400 mg/cm^2 Au secondary target was used to encourage Coulomb excitation of the beam.

Two ToF options were used simultaneously throughout the first LYCCA-0 commissioning experiment. The first option, which shall be referred to as the plastic ToF, used fast plastic scintillators as both start and stop signals. The second option, the diamond ToF, used the diamond detector as a start detector and the fast plastic scintillator in front of the LYCCA wall as the ToF stop. Ideally, the start of any LYCCA ToF measurement would want to made as close to the secondary target as possible so that the velocity of a fragment exiting the target can be calculated directly from the ToF measurement. Although this is the case for the diamond ToF, it could not feasible for the plastic ToF as the plastic scintillator was too large to fit inside the target vacuum chamber, which is limited in size by the surrounding

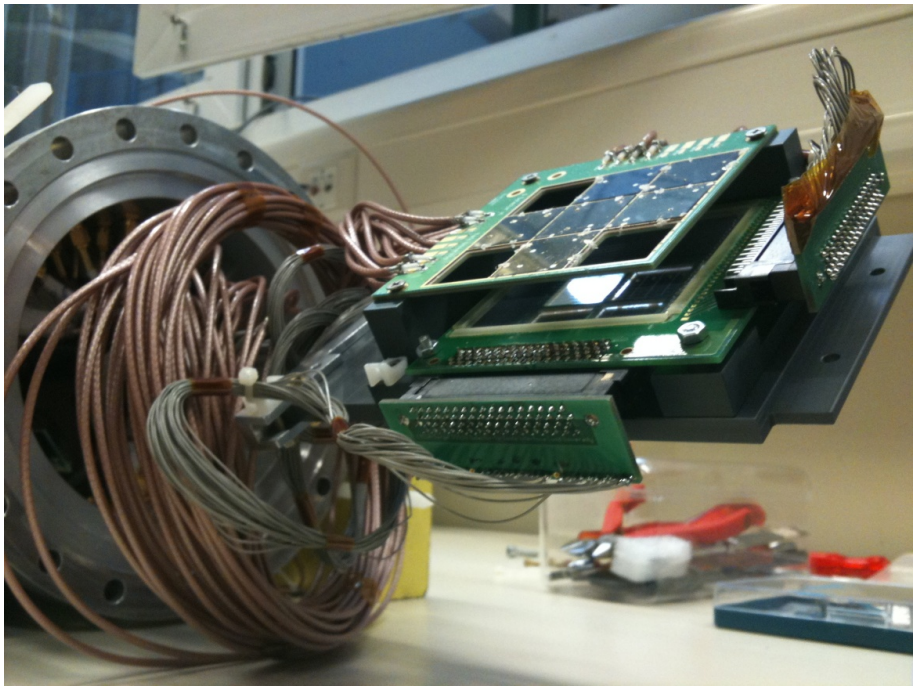

Figure 4.7: Photograph showing the target detectors, a single DSSSD (middle) and the diamond start detector (top). The secondary target is positioned on the underside of this mounting structure.

RISING Ge array.

4.3.2 Diamond Start Detector

The diamond start detector was designed to cover the same area as the target DSSSD, although only 6 out of a possible 9 wafers were in use during the commissioning of LYCCA-0. A top-down view of the diamond start detector is shown in Figure 4.8a. For 5 of the 6 wafers, the contacts were segmented into four strips, as was the case for the TAMU experiments (section 3.1), whilst the final wafer used a contact which covered the full area of the wafer. This larger contact was included as a further test of the timing resolution dependence on detector capacitance, and to discover whether increasing the pad area from a 18 mm x 5 mm strip to a full area contact affects the timing resolution in the same way as decreasing the pad size to 2 mm x 3 mm. Three different types of contact metallisation were used for the diamond start detector, details of which can be seen in table 4.1. Different metallisations were used, partly for convenience, as some of the contacts had already been fabricated prior to the construction of the start detector, and partly to compare the performance of each contact under the same experimental conditions.

Wafer	Front Contact Material	Back (Ground) Contact Material
2	Al (80 nm)	Ti/Pt/Au (30/20/50 nm)
4	Ti/Pt (30/50 nm)	Ti/Pt (30/50 nm)
5	Ti/Pt/Au (30/20/50 nm)	Ti/Pt/Au (30/20/50 nm)
6	Au (100 nm)	Au (100 nm)
8	Al (80 nm)	Ti/Pt/Au (30/20/50 nm)

Table 4.1: Contact metallisation for each wafer of the diamond start detector. The thickness of each metal layer is given in brackets.

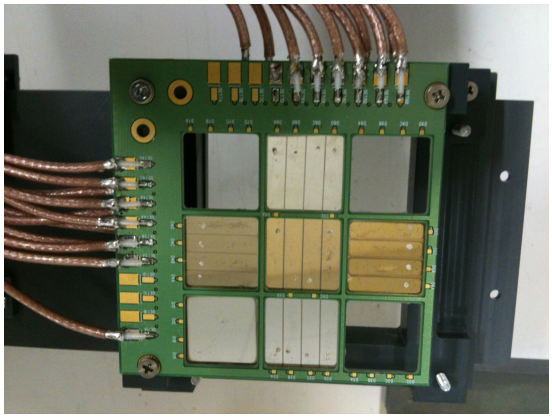

(a) Top-down view of diamond start detector

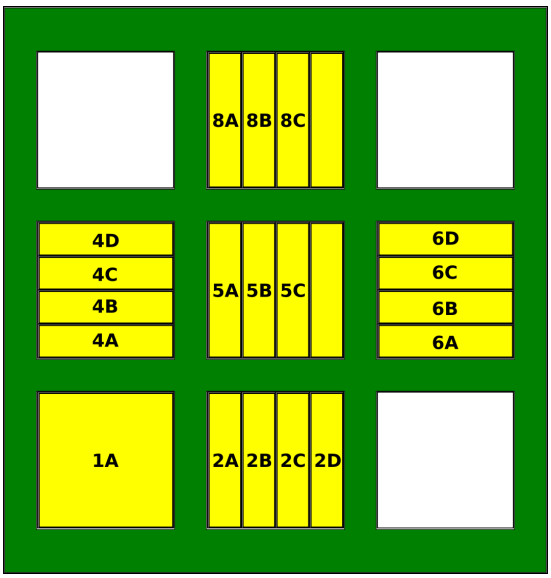

(b) Wafer and strip positions

Figure 4.8: The diamond start detector as (a) a photograph showing the different contact metallisations, the high density PCB, and the high frequency cables used in the commissioning experiment, and (b) a schematic diagram showing the strip and wafer positions as seen looking downstream.

The PCB used for the diamond start detector was, once again, impedance matched and designed to cope well with high frequency signals. The diamond signals were carried to DBA IV preamplifiers using the same high frequency coaxial cables as were used in the detector optimisation experiments, however, for the LYCCA-0 commissioning, the cables had to carry the signals over 2.5 m before reaching the preamplifiers, compared with a distance of only 1 m for the optimisation experiments. Cables of this length were necessary during the commissioning experiment as the flange containing the cable feedthroughs for the target detectors had to placed above the gamma-ray array and the target mount the lowered into position at the

centre of the array, approximately 2 m below the flange. Around 0.5 m of cable was required to carry the signal from the flange feedthroughs to the preamplifiers outside of the chamber.

The amplified diamond signals were processed by LEDs before being converted to an ECL signal and fed to the V1290 TDCs, as can be seen in Figure 4.9. The 64 signals from the plastic scintillators were processed using CFDs, and then distributed evenly between the three TDCs along with the 19 signals from the diamond start detector. The start of data acquisition was signalled for all three of the TDCs using the master trigger to ensure that the timing data from one TDC was correlated with the other two.

For the commissioning experiment, the master trigger could be set to either a particle trigger, or one of two particle-γ coincident triggers. The particle trigger was generated when signals from all LYCCA and FRS detectors were received within a certain time window of a signal from the SC41 FRS scintillator. A particle-γ trigger was generated in a similar manner to a particle trigger, but also required a signal from one of the γ-ray detectors to arrive with the time window to fulfil the trigger requirements [62].

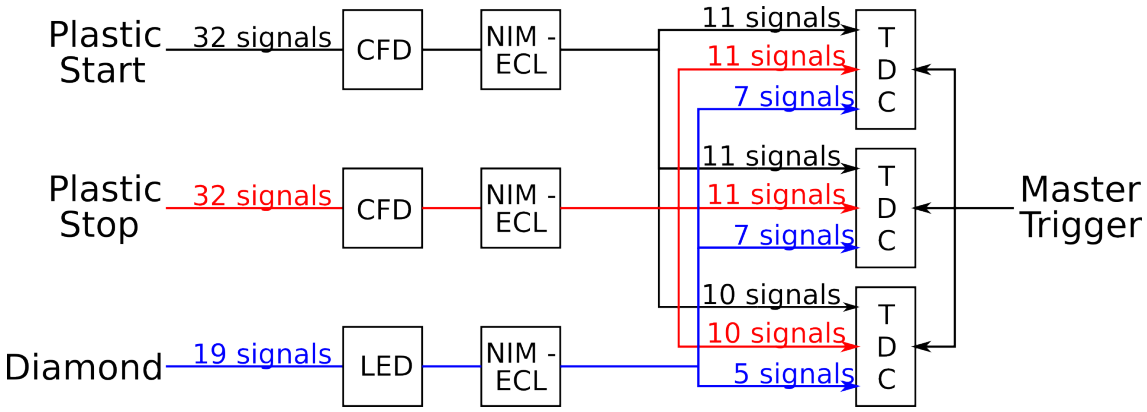

Figure 4.9: Schematic diagram of the electronic setup for the ToF detectors at the commissioning experiment. The 64 scintillator signals and 21 diamond signals were distributed evenly between the three V1290A TDCs. The TDCs were synchronised with one another using the master trigger which signalled the start of data collection in each TDC.

4.3.3 Si DSSSDs

Double Sided Silicon Strip Detectors (DSSSDs) are commonplace in nuclear physics experiments due to their ability to measure both the energy loss and the position

of a particle. The DSSSDs used for LYCCA-0 measure 60 mm x 60 mm, with an active area of 58 mm x 58 mm. Each DSSSD is segmented into 32 horizontal strips on the front of the detector, and 32 vertical strips on the back (see Figure 4.10). The crossover effect of the front and back strips creates 1.8 mm x 1.8 mm pixels that are used to determine the position of any particle that strikes the detector.

Due to limited signal processing electronics during the first commissioning experiment, four neighbouring strips were electronically adjoined on both front and back of some DSSSDs to effectively form strips that were four times wider. This worsens the position resolution of the DSSSD significantly as only 64 pixels are formed per DSSSD rather than the usual 1024 pixels. With this in mind, only DSSSDs in the top and bottom rows of the LYCCA-0 wall used this less precise method, as fewer fragments are expected to hit the detectors found in these positions. The position measurements performed by the target DSSSD and the wall DSSSDs can be used to track a fragment through LYCCA (see section 4.3.5 for more details).

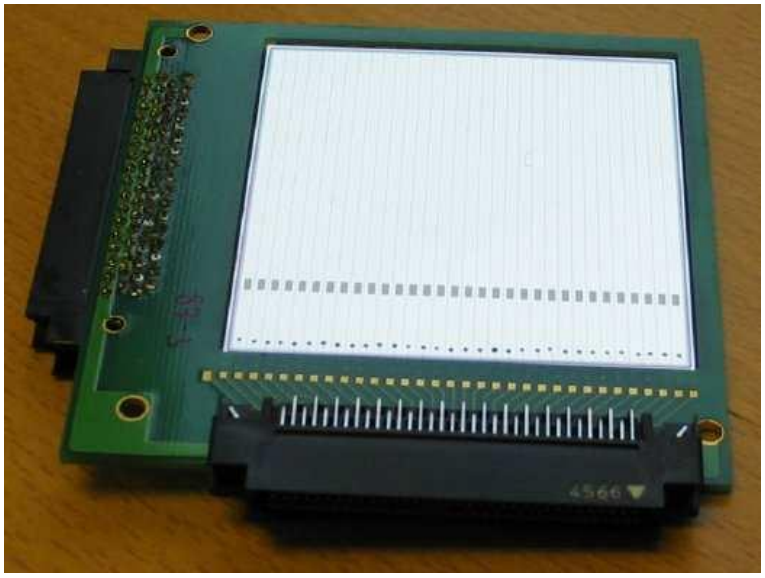

Figure 4.10: Photograph of a DSSSD used in the LYCCA-0 commissioning experiment. Segmentation into 32 vertical strips can be seen on one side of the detector, whilst the opposite side will be segmented into 32 horizontal strips, creating a total of 1024 pixels.

Silicon, as an intrinsic semiconductor has a naturally high leakage current, caused by electrons that are thermally excited across the narrow band gap of 1.1 eV [30]. This leakage current would ordinarily overshadow any current generated by ionising fragments passing through the detector, rendering the detector useless, however, this leakage current can be significantly reduced by applying p-type and

n-type dopants to opposite sides of the Si detector and creating a p-n junction. Thermally excited electrons are attracted toward the high concentration of holes found in the p-type material, and the excess free electrons in the n-type material diffuse toward the redundant holes left by the thermally exited electrons, creating a depletion region containing very few charge carriers between the p- and n-type materials.

The width of the depletion region can be increased by reverse biasing the detector, i.e., applying a negative voltage to the p-side of the detector with respect to the n-side. A reverse bias of -60 V was applied to the LYCCA-0 DSSSDs to ensure that all electron-hole pairs created by ions passing through the detector were collected at the electrodes before any recombination occurred. The energy signal from the DSSSDs was amplified using preamplifiers and then sent through Mesytec shaping amplifiers before being acquired by peak sensing Analogue-to-Digital Converters (ADCs). Typical energy loss values measured by the wall DSSSDs during the commissioning experiment were found to be 250 - 350 MeV.

4.3.4 CsI Crystals

CsI scintillators were chosen to make the residual energy measurements for LYCCA as these inorganic scintillators provide good energy resolution for charged particle detection. The energy resolution of a scintillator is found to be highly dependent upon the uniformity and efficiency of the light collection, the latter of which can be improved by surrounding the crystal in reflective foil and tapering one end of the crystal to optimise light collection. Any issues concerning the uniformity of light collection can be minimised by reducing the size of the scintillating crystal.

The CsI crystals used in the LYCCA-0 commissioning experiment had a front face measuring 19 mm x 19 mm, with a total depth of 40 mm. The final 7 mm of this depth tapers toward a back face which measures 10 mm x 10 mm, and acts as a light guide for the photons generated inside the scintillating crystal (see Figure 4.11a). Light collection is made by photodiodes that are glued onto the back face of the crystal using optical epoxy. Each individual crystal is then wrapped in three layers of VM2000 foil for improved efficiency and mounted together in groups of 9, as can be seen in Figure 4.11b. This photograph also shows an individual crystal and a single photodiode, the sizes of which can be compared to a two Euro coin. The CsI crystals are doped with a thallium activator, which enables the emission of a photon in the visible region so that it can be detected by the photodiode.

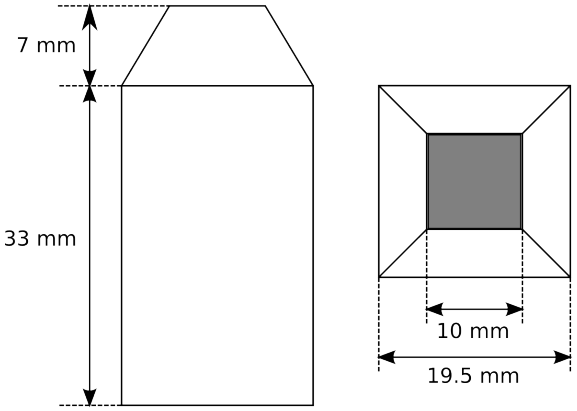

(a) The dimensions of a CsI crystal

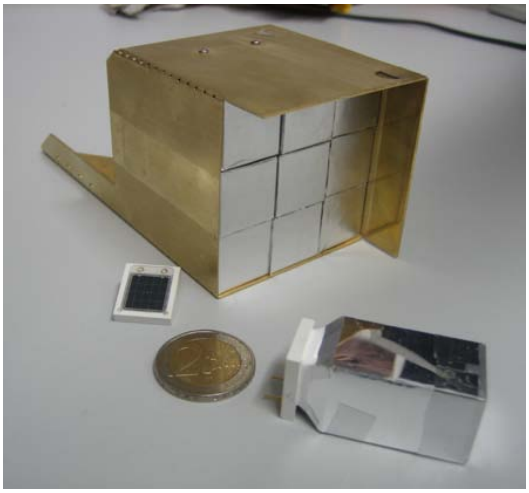

(b) Photograph showing the CsI scintillators

Figure 4.11: Details of the CsI scintillators used for residual energy measurements including (a) a schematic of the individual CsI crystals, and (b) a photograph showing an individual CsI crystal wrapped in VME2000 foil, a single photodiode and a full block of 9 CsI crystals in their mounting.

4.3.5 Tracking Fragments Through LYCCA-0

Accurate knowledge of a particle's trajectory after the secondary target is vital when trying to correct for the Doppler shift of a gamma ray emitted from an in-beam nucleus. Knowing the angle of the trajectory is also very important when trying to reduce the error associated with the ToF measurement, as this allows the length of a fragment's flight path to be calculated on an event by event basis.

Fragments were tracked through the LYCCA-0 detector system using the target and wall DSSSDs, as well as the TPC situated closest to the secondary target. Figure 4.12 shows one possible trajectory for an ion passing through the position detectors and the secondary target. The angle of the trajectory before the target, θ_{in}, can be calculated using the relative x and y measurements from the TPC and target DSSSD, as indicated in the figure. Similarly, the angle of the trajectory after the target, θ_{out}, can be calculated from x and y measurements of the target and wall DSSSDs.

4.3.6 Calibrating LYCCA-0

For a fragment to be correctly identified using LYCCA-0, each detector had to be calibrated using known energy values. Three different FRS degrader settings were

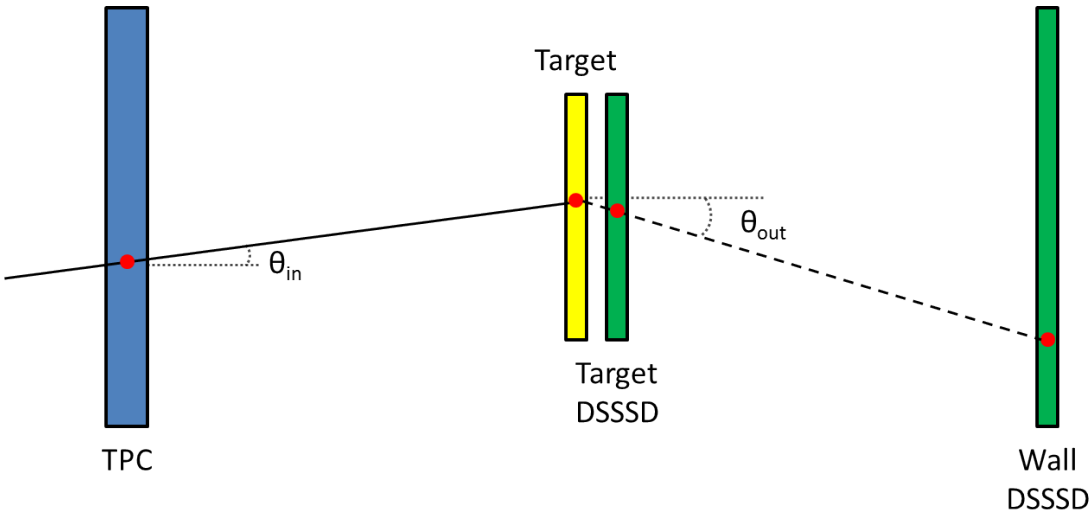

Figure 4.12: A fragment can be tracked through the LYCCA-0 detector system using position measurements from the final FRS TPC, as well as the target and wall DSSSDs. Both the angle into (θ_{in}), and out of (θ_{out}) the target can be calculated from these measurements, which are useful when making corrections to various aspects of the analysis.

used to generate three different energy loss and residual energy measurements in the wall DSSSDs and CsI scintillators respectively. The predicted values for these energies were calculated using LISE++ [63], a simulation program for fragment separators that is commonly used to find the transmission and yield of fragments travelling through the FRS and other separators. Details of the degrader settings and the energy values calculated in LISE++ are given in table 4.2. A 550 MeV/u ^{64}Ni secondary beam was used for all calibration runs.

Production Target	**F2 Degrader**	**F4 Degrader**	**Energy Loss (MeV)**	**CsI Energy (MeV)**
0 g/cm^2	4 g/cm^2	2 g/cm^2	165	17715
4 g/cm^2	4 g/cm^2	0 g/cm^2	200	12360
4 g/cm^2	6 g/cm^2	0 g/cm^2	360	5150

Table 4.2: Details of the degrader settings used in the calibration of LYCCA-0 and the corresponding energy loss and residual energy values predicted using LISE++.

The raw energy measurements from the wall DSSSDs and the CsI scintillators from each of the three calibration runs were plotted against the predicted values, and a linear fit was made to the three points. The parameters of the linear fit determined the offset and gain for the calibration, and was repeated for each DSSSD strip and individual CsI crystal in the LYCCA-0 wall. These offsets and gains were used

throughout the rest of the experiment so that an accurate conversion between raw energy data and predicted energy could be made. Further details on calibrating the LYCCA-0 energy detectors can be found in reference [64].

4.3.7 Gamma-ray Detectors

Two different types of γ-ray detectors were present for the first LYCCA-0 commissioning experiment, the primary γ-ray system being made up of fifteen former EUROBALL Ge cluster detectors that surrounded the downstream side of the LYCCA-0 target position. This array was chosen as it had been used previously throughout the RISING campaign, and therefore did not require commissioning. Eight HECTOR BaF_2 detectors, optimised to detect high-energy γ-rays, were also positioned around the secondary target at a forward angle of 85°. The γ-ray detectors are labelled in the top-down photograph of the LYCCA-0 setup shown in Figure 4.13, along with other important aspects of the LYCCA-0 array.

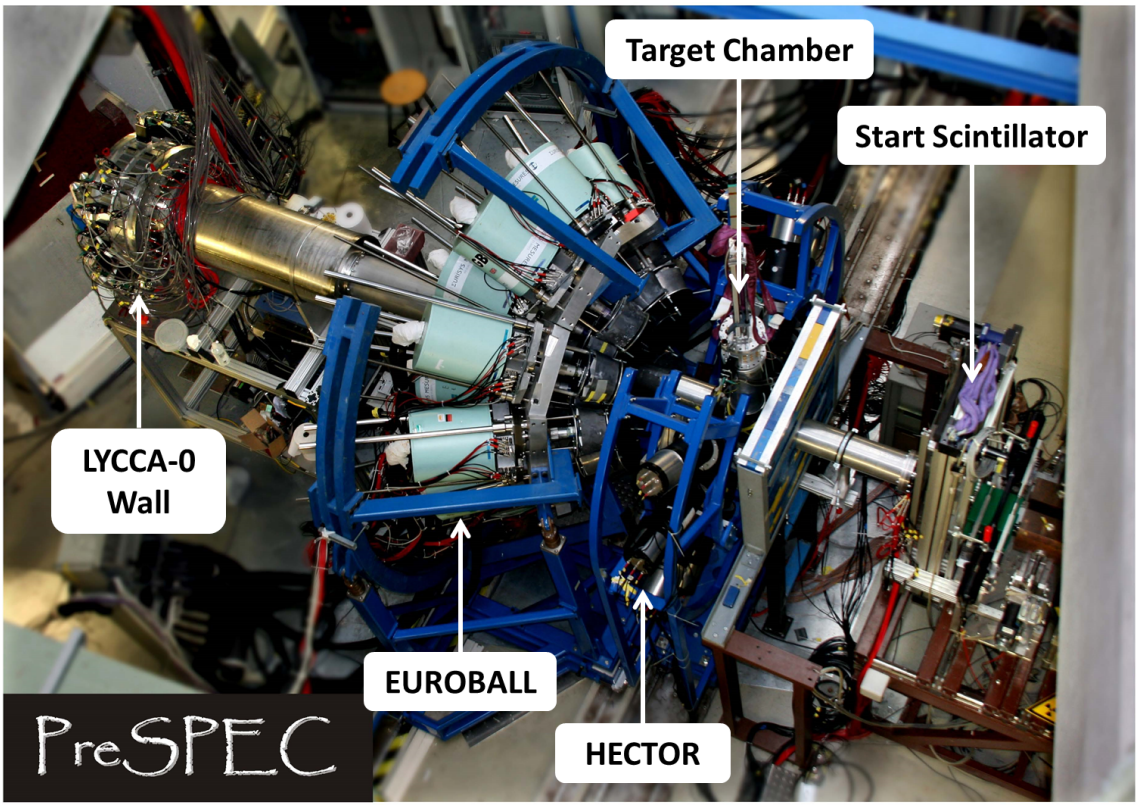

Figure 4.13: A top-down photograph of the LYCCA-0 setup. The γ-ray detectors can be seen surrounding the target chamber, which houses the secondary target, target DSSSD and diamond detector. The chamber that accommodates the LYCCA-0 wall detectors can be seen at the end of the beam line.

4.4 Fast Plastic Scintillators

Even though the ultimate ToF system for LYCCA always aimed to use diamond detectors because of their durability and good timing resolution, a full complement of diamond detectors was not immediately available for the commissioning experiment, as they were still in an early stage of development. Fast plastic scintillators were therefore employed to ensure a full ToF system could be used.

4.4.1 Construction and Operation

A large area, single sheet design was chosen for both start and stop LYCCA-0 scintillators because this design offered the most potential for good timing resolution [12]. The large area also ensured that the majority of fragments that were scattered at a relatively large angle by the secondary target were still able to hit the stop detector in a fairly central location. A photograph of the plastic start scintillator can be seen in Figure 4.14. Light collection is performed by the 32 photomultiplier tubes (PMTs) positioned around the outside of the 27 cm-diameter plastic sheet. For the start scintillator, these PMTs were held in position by an octagonal acrylic glass frame which grouped the PMTs into eight sets of four. The stop scintillator used a more efficient circular frame design, which permits the PMTs to be placed closer to the scintillator plastic, effectively increasing the solid angle of the PMT and allowing more photons to be collected.

The scintillators use a 2 mm-thick BC-420 plastic scintillator sheet, produced by Saint-Gobain. Unlike the CsI scintillators used in the LYCCA wall, plastic scintillators use organic molecules to produce photons in the visible region. These molecules are dissolved in a solution which can be polymerised and shaped into a sheet. When a charged particle passes through the plastic sheet, energy from the particle is transferred to the organic molecule, causing an electron to excite into a higher electronic energy level. De-excitation of this electron from the S_1 electron state to the S_0 ground state produces a photon of typically a few eV in a process known as fluorescence [30]. With a charged ion in the commissioning experiment losing around 800 MeV when passing through the start scintillator, one can imagine that millions of photons are produced in a single event. These photons travel through the plastic in an arbitrary direction until they reach one of the PMTs, usually after being internally reflected a number of times. Not all photons are collected by the PMTs, some are absorbed by the scintillator material, some are lost at the

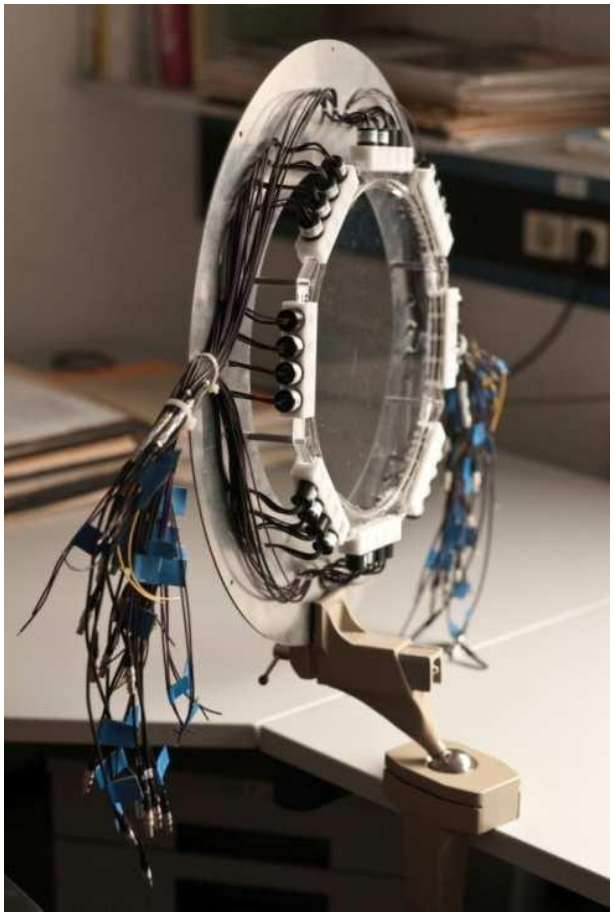

Figure 4.14: Photograph of the LYCCA-0 start scintillator. It consists of a 27 cm-wide plastic sheet surrounded by 32 PMTs for light collection [12].

plastic-air interface, and others are simply generated outside of the solid angle of any of the 32 PMTs, and so cannot be detected.

The timing resolution of the plastic scintillators mainly depends upon the number of photons detected, and the time taken to collect these photons, i.e., the rise time of the PMT signal. A faster rise time and improved resolution can be achieved by placing the PMTs closer to the interaction point, which is not possible when using large area scintillators. Taking this fact into consideration, one can expect the timing resolution, σ, from a single PMT around the LYCCA-0 scintillators to be fairly poor, however this can be vastly improved by combining signals from all 32 PMTs to create the final timing signal. Each PMT takes an independent measurement for every ion passing through the scintillator, which means that, assuming each PMT performs identically, the timing resolution is reduced by a factor of $\sqrt{32}$. This more than compensates for the reduction in resolution caused by the slow rise time of the

PMTs.

4.4.2 Corrections to Timing Signal

Despite the fact that a large-area, single-sheet design has many advantages when it comes to making a good timing detector, it also introduces an uncertainty into the timing signal associated with the distance of the interaction point from the centre of the scintillator. Photons generated at the centre of the scintillator have to travel the full radius of the detector before being detected by a PMT, which takes over 700 ps. This can be compared to the time taken for a photon generated just 5 cm from a PMT, which is around 260 ps. An uncertainty of 440 ps between these two extremes is introduced into the timing system, which is more than a factor of four greater than the minimum timing resolution of 100 ps required for unambiguous fragment identification. It therefore becomes very important to correct for this position dependence, and this can be done with the aid of the the tracking detectors.

The position of a hit on the start scintillator can be determined by interpolating the position measurements made by the TPC positioned at F4 and the target DSSD, which are found either side of the start scintillator. A similar procedure can be done for the stop scintillator using the target DSSSD and LYCCA-0 wall DSSSDs. With the hit positions on the scintillators known, the following correction can then be made to the timing signal, t_i, from a given PMT [65]:

$$t_{cor_i} = t_i - \frac{d_i \cdot n}{c} \tag{4.1}$$

where t_{cor_i} is the corrected timing signal, d_i is the distance between the interaction point and the PMT, n is the refractive index of the plastic scintillator, which is equal to 1.58 for BC-420, and c is the speed of light. This correction must be made to every PMT signal before a final timing value can be obtained by averaging all 32 corrected signals.

4.5 Mass Measurements with LYCCA

Fragments can be identified using LYCCA and LYCCA-0 in one of two ways, either by using 2D ToF versus energy plots, where fragments of the same mass form loci, or by calculating the mass of a fragment on an event-by-event basis from calibrated ToF, energy and energy loss measurements. Although the 2D plots are very useful when trying to gate on a single fragment, it is very difficult to obtain a reliable mass

resolution from these plots because of the diagonal nature of the fragment regions. This problem is not encountered when using the event-by-event mass calculation method, and a mass resolution measurement is much easier to perform.

Measuring the mass resolution of LYCCA-0 is an integral part of the analysis presented in this thesis, as it is the only way of deconvoluting the timing resolution from the energy resolution. Simply determining the width of the ToF peak when gated on a single fragment would not provide an independent time resolution measurement, as this width would also include the dispersion of momentum experienced by the fragments as they undergo a fragmentation reaction, and this cannot be accounted for. By combining the energy and ToF measurements into a single mass measurement, each energy measurement is correlated with a corresponding ToF value, which means that only the resolution of the energy and time measurements contribute to the width of a mass peak, and the momentum spread no longer has to be considered.

Equation 4.2 describes how the energy and mass of a fragment in a beam affects the beam velocity, β, at relativistic energies:

$$\beta^2 = 1 - \left(\frac{931.5}{931.5 + \frac{E}{A}} \right)^2 \tag{4.2}$$

The factor of 931.5 is used to convert atomic mass units into MeV. Rearranging the above produces the relativistic mass equation, which allows one to calculate the mass of a fragment in the beam from measurements of its energy and velocity over a certain flight path:

$$A = \frac{E_{total}}{\frac{1}{\sqrt{1-\beta^2}} - 1} \cdot \frac{1}{931.5} \tag{4.3}$$

Here, E_{total} is the kinetic energy (in MeV) of the fragment during the majority of its flight path, and β is the velocity of the fragment after the secondary target as a fraction of the speed of light, c. For both timing options, the longest flight time occurs between the secondary target and the stop scintillator, and hence it is the energy of the fragment at this point that is used for the mass calculation. This energy can be calculated by summing the measurable energy deposition in both LYCCA-0 wall detectors, as well as the energy deposited in the stop scintillator and the Al foil used to shield the DSSSDs from the scintillation light. Obviously, the stop scintillator and foil are not capable of making energy loss measurements, so the energy deposition in these materials need to be calculated using simulation software

such as LISE++.

The β value of each fragment after the secondary target can be calculated from the diamond ToF, t_{dia}, using the equation:

$$\beta_{dia} = \frac{d_{dia}}{\cos(\theta_{after}) \cdot t_{dia} \cdot c} \tag{4.4}$$

where d_{dia} is the length of the flight path for the diamond ToF, i.e., the distance between the diamond start detector and the stop scintillator, and θ_{after} is the angle at which the fragment travels after interacting with the secondary target.

Finding the β value from the plastic ToF, t_{pl}, requires a more complicated approach, as the start scintillator is placed a significant distance in front of the secondary target. It is therefore useful to split the flight path into two distances, before and after the target, and estimate the velocity at which the fragments were travelling between the start scintillator and secondary target. The equation used to calculate β_{pl} is given below:

$$\beta_{pl} = \left[\left(t_{pl} - \frac{d_{before}}{cos(\theta_{before}) \cdot \beta_{before} \cdot c}\right)\left(\frac{cos(\theta_{after}) \cdot c}{d_{after}}\right)\right]^{-1} \tag{4.5}$$

Here, d_{before} and d_{after} represent the distances between start scintillator and target, and target and stop scintillator respectively, and θ_{before} and θ_{after} represent the angle of a fragment's trajectory before and after the secondary target. β_{before} is the estimated β value of a fragment as it passes between the start scintillator and the target, and is calculated using the β measurement through the FRS, which varies event by event, and a constant offset value calculated from the LISE++ simulation code. This offset is different for each secondary beam setting, and is determined by finding the difference between the simulated value of β through the fourth dipole of the FRS and the simulated value after the start scintillator. With this in mind, the fraction $\frac{d_{before}}{cos(\theta_{before}) \cdot \beta_{before} \cdot c}$ can effectively be thought of as the time taken for a particle to travel from the start scintillator to the secondary target, and therefore, subtracting this from the total plastic ToF leaves just the ToF after the secondary target, as required.

The contribution to the mass resolution, $\partial A(E)$, from the resolution of the energy detectors can be found by partially differentiating equation 4.3 with respect to E_{total}. This gives:

$$\partial A(E) = \frac{A}{E} \cdot \partial E \tag{4.6}$$

Similarly, a partial differentiation of equation 4.3 with respect to β provides an expression for the mass resolution contribution, $\partial A(\beta)$, from the resolution of the β measurement :

$$\partial A(\beta) = -\frac{\beta(1863A + 2E)^3}{6941538A \cdot E} \cdot \partial\beta \tag{4.7}$$

The resolution of the energy and β measurements in the above equations are represented by the symbols ∂E and $\partial\beta$ respectively. The mass resolution contributions from E and β can be combined in quadrature to give the overall mass resolution, ∂A, that would be measured from experimental data:

$$\partial A = \sqrt{\partial A(E)^2 + \partial A(\beta)^2} \tag{4.8}$$

If the energy resolution is known, then $\partial A(E)$ can be calculated using equation 4.6, which can subsequently be used to find $\partial A(\beta)$ from equation 4.8. Once $\partial A(\beta)$ is known, the resolution of the β measurement can be found, which is directly related to the timing resolution of the detectors used to make the ToF measurement.

Ideally, one should find the timing resolution from $\partial\beta$ by partially differentiating the equation used to calculate the β value. This, however, is not straightforward for the β_{pl} calculation in equation 4.5, as the β_{before} term adds a number of complications. As a result, the general equation for β given in equation 4.4 is used to find the relationship between the resolution of β and the timing resolution. Partially differentiating and rearranging this equation gives:

$$\partial t = \frac{c \cdot t^2}{d} \cdot \partial\beta \tag{4.9}$$

Here, t and d represent the ToF and the length of the flight path for either plastic or diamond ToF options, depending upon which timing resolution is desired. Only the complete plastic ToF that includes the time taken for a fragment to travel from the start scintillator to the secondary target is known, and therefore, the total flight path between the start and stop scintillators must be used in the timing resolution calculation.

CHAPTER 5

Results: Detector Optimisation Experiments

Results from the optimisation experiments undertaken at Texas A & M University (TAMU) and the University of Birmingham are given in this chapter. Factors such as the electronics setup, detector bias and contact material were varied in the TAMU experiment, whereas the Birmingham experiment focused upon the capacitance dependence of the diamond detector, as well as further investigating the effect of the contact material.

5.1 TAMU Experimental Results

The most important results from the TAMU tests were the optimisation of the electronic setup and the timing resolution achieved by the diamond detector, however, a number of problems were encountered during the experiment, which helped to broaden the understanding of the detectors.

5.1.1 Problems Encountered During the Test

5.1.1.1 Low Amplitude Signals

The diamond detector prototype shown in Figure 3.2b was first bombarded with a 33.5-MeV/u ^{40}Ar beam that was incident upon the top wafers of the front and back detectors, both of which had Al contacts. The resultant signals from the wafer on the back detector were found to generate very few events in the TDC. After connecting the outputs from the preamplifiers to a high frequency oscilloscope via long coaxial cables into the control room, it was concluded that the lack of events was caused by low amplitude signals from the Al wafer that were unable to exceed the threshold of the LEDs and CFDs. When the signals from the top wafer of the front detector were viewed using the same coaxial cables and oscilloscope however, the amplitudes were considerably greater, enabling the expected number of events to be recorded by the TDC.

This suggested that it was not the contact material that was affecting the amplitude of the signals, rather the quality of the contact fabrication or connection between the contact and bonding wire that was causing the issue. This problem meant that only the strips on the lower Au wafers could be used to make timing measurements, preventing the comparison of timing resolutions for different contact materials.

5.1.1.2 Breakdown of the Preamplifiers

The most significant problem encountered during the experiment involved the breakdown of most of the DBAIV preamplifiers. As well as their main purpose of amplifying the signals from the diamond detector, the preamplifiers were also used as a means of applying the high voltage (HV) bias across each diamond strip. After around 12 hours of biases being applied and removed via the DBAIVs, they became hot, causing the electrical components inside the preamplifiers to blow.

Some of the diamond strips had to be biased by the same HV supply through a splitter box because there weren't enough high voltage channels for each of the 16 strips. Whenever a preamplifier blew, the HV supply it was connected to automatically tripped, suddenly reducing the bias to 0V. If this HV supply was also connected to other preamplifiers via a splitter box, the sudden drop in bias also caused these preamplifiers to blow. By the end of the ^{40}Ar beam time, only 3 out of the 16 preamplifiers were able to amplify signals.

To avoid any further damage to the preamplifiers, fans were placed beside the DBAIVs in an attempt to cool them down. The bias was also increased and decreased slowly to limit the amount of current passing through the preamplifier, which was the source of most of the heat.

Although the temperature of the DBAIVs was thought to be the main cause of their breakdown, "sparking", or electrical breakdown on the surface of the detector was also proposed as a possible explanation. Diamond has a very high electrical breakdown field, making it an unlikely location for sparking to occur, however sparking may have taken place between the quick-drying silver paint used to attach the wafers to the PCB and the signal tracks on the PCB used to carry both the signals from, and bias to, the diamond strips. As can be seen in Figure 5.1, the silver paint extends beyond the ground plate below, effectively reducing the distance between the ground plate and the bias carrying tracks, consequently increasing the electric field present between the them. If the electric field became too high, electrical breakdown of the white insulating material may have occurred, causing a large current to surge through the PCB tracks to the preamplifier and blowing the electrical components inside.

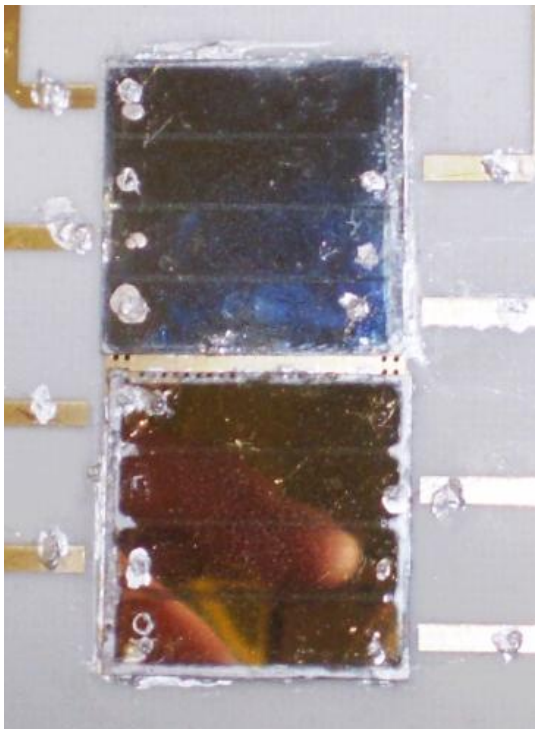

Figure 5.1: Photograph showing the silver paint extending over the edge of the ground plate. This reduces the distance between the ground plate and the bias-carrying tracks, which could cause breakdown to occur on the surface of the PCB.

A new PCB was used for the LYCCA-0 commissioning experiment, the design of which took the possibility of electrical breakdown into consideration. If sparking was the cause of the preamplifier breakdowns, the chance of it happening again using the new PCB should be reduced.

The preamplifier breakdowns meant that only two out of the possible 16 strips could be used to make timing measurements consistently throughout the experiment. Consequently, only analysis from the best performing pair of strips will be shown in this section.

5.1.2 TDC Non-Linearity

Prior to mounting the diamond detectors, a fast pulser was used in the place of the detectors to optimise the TDC settings and ensure that that cabling of the electronics was correct. During these checks, it was noted that the timing measurements were not linear across the full range of the TDC bins. This non-linearity can be seen when plotting the raw pulser data from one TDC channel against another. One would expect to see a perfectly linear trend from this plot due to the consistent nature of the pulser input, however, as can be seen in Figure 5.2, the black data points deviate from the linear fit (red), showing that this is not the case. This non-linearity can be attributed to a variation in bin sizes across the range of the TDC. In theory, each bin should be 25 ps wide, but it is clear from Figure 5.2 that some must be less than this value, creating data points above the linear fit, whilst others must be greater, indicated by data points below the fit.

To fully linearise the TDC, a correction must be made to every bin in each of the 32 channels in the TDC, which is quite a demanding task. The linearisation undertaken during the analysis of the TAMU data only made corrections to the bins within the range of the data collected, which lessened the complexity of the task a little.

For each run file, a cumulative distribution of the raw TDC data from a single channel was made by adding the number of events found in a bin to the number of events found in the previous bin across the full range of the TDC data (see black lines in middle plot of Figure 5.3). This cumulative distribution was then compared to the cumulative distribution of a step function (red line), which would be the ideal shape for the raw TDC data without the non-linearity.

The corrections required for each bin could be found by subtracting the two cumulative distributions from one another, the results of which can be seen in black

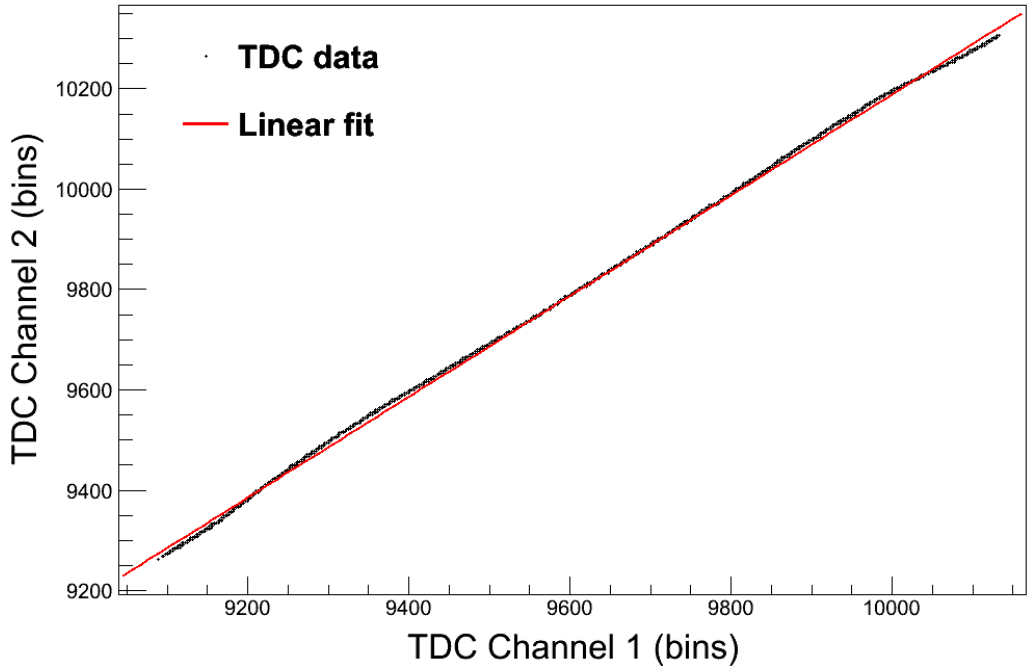

Figure 5.2: Graph showing the TDC data from a pulser (black) compared with a linear fit to the data (red). Due to the repetitive and consistent pulser input, one would expect a perfect straight line to form when one TDC channel is plotted against the other. This is not the case because the bin sizes are found to change across the range of the TDC.

in the lower plot of Figure 5.3. The raw TDC data were then reprocessed so that the bin-dependent corrections could be applied on an event-by-event basis. To check how effective the corrections were, the linearisation method described above was repeated with the corrected data and the final result of the distribution subtraction is shown in blue in the lower plot of Figure 5.3. The variation in this blue histogram is much smaller than the original corrections shown in black, which indicates that the linearisation was successful.

Reducing the non-linearity associated with the TDC should improve the timing resolution obtained from the diamond detector and its accompanying electronics.

5.1.3 Results from ^{40}Ar Beam

5.1.3.1 Resolution at Different Biases

The bias dependence of the timing resolution was tested by varying the bias applied across the front and back detector strips from 300 V to 600 V in five independent

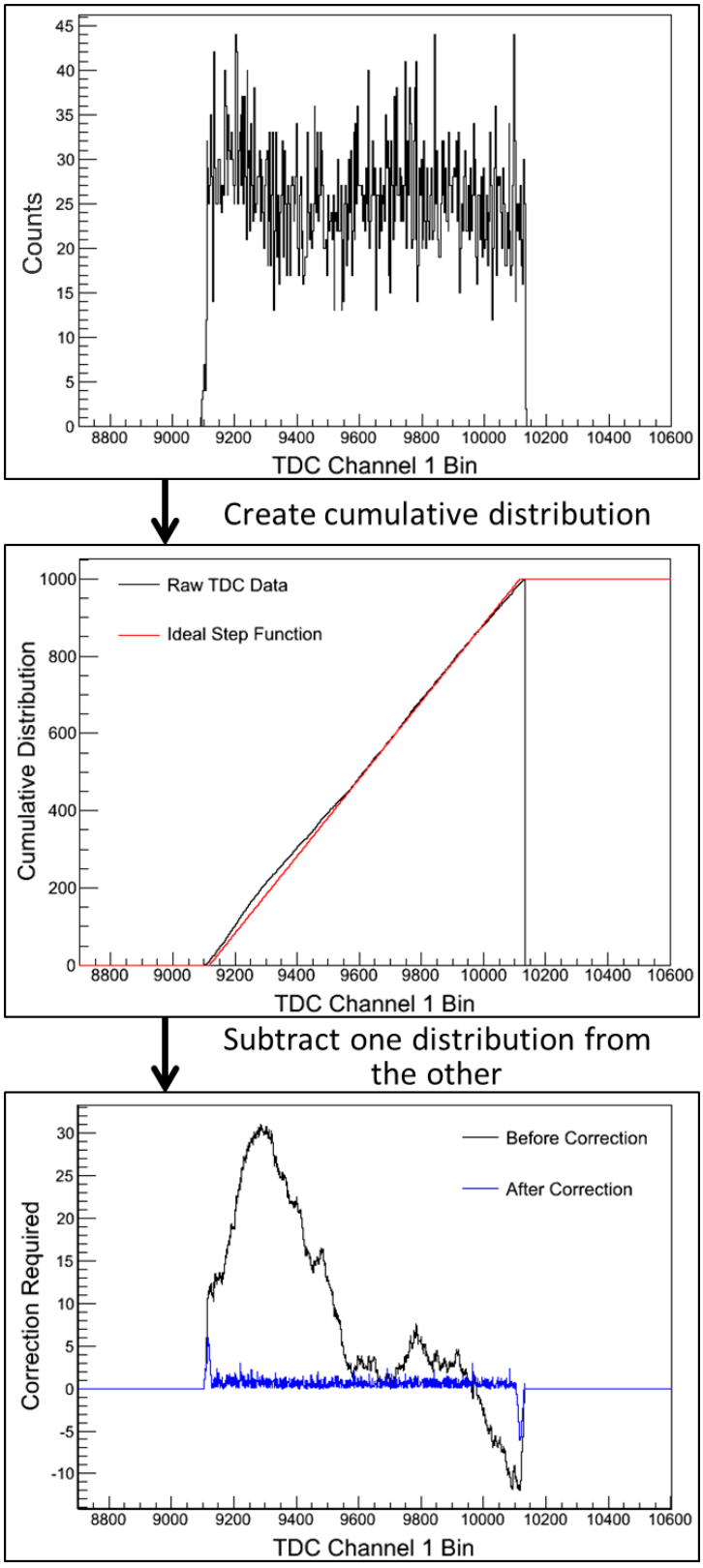

Figure 5.3: Plots showing the linearisation procedure. (top) Raw TDC data, (middle) cumulative distributions, and (bottom) corrections required to each bin before after after linearisation.

runs. Timing peaks were made for each bias setting by subtracting the TDC data of the start timing signal from the front detector strip from the TDC data of the corresponding back strip, which provided the stop signal, and plotting the result on a histogram. The variation in these measurements produced a Gaussian distribution that was fitted to extract the FWHM (Full Width at Half Maximum) of the peak. This value was then converted into picoseconds by multiplying by 25. The TDC data used to create these timing peaks had been processed using the linearisation procedure described above.

FWHM measurements are preferred over σ, as they give a better representation of the precision to which the ToF can be measured. For example, if a FWHM was measured to be 200 ps, it would suggest that fragments with a difference of 200 ps in their ToFs would be distinguishable.

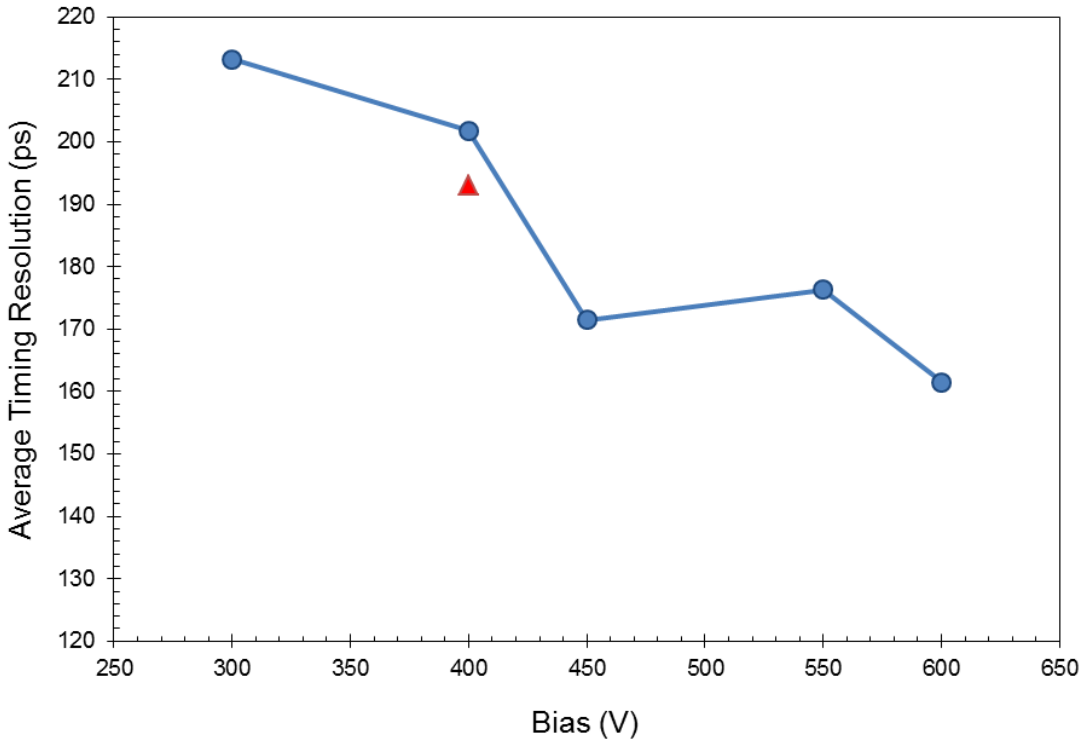

Figure 5.4: Plot to show how the timing resolution (FWHM) of the diamond detectors varies with the applied bias. The general trend shows that the resolution improves as the bias is increased, however, the point shown as a red diamond indicates a result taken under low noise conditions, emphasising the importance of noise on the timing resolution. It is thought that the result at 450 V was also taken under these low noise conditions.

The timing resolution (FWHM) results from each bias setting are shown in Figure 5.4. It should be noted that these resolutions are for the timing measurement itself, not the resolution of each individual diamond detector. The trend of the results indicates that, for biases below 600 V, the timing resolution improves as the bias applied across the strips is increased. This may not be the case above 600 V, as the velocities of the charge carriers within the diamond will eventually saturate. Two results are shown for an applied bias of 400 V. The result with the better resolution (red diamond on Figure 5.4) was taken during a short period when the noise inside the experimental cave was around 20 mV, compared with the usual 40 mV experienced during the rest of the experiment. This result was included in Figure 5.4 to emphasise the importance of low noise levels when trying to achieve a good timing resolution.

The result indicated by a red diamond and the result obtained for a bias of 450 V used data that were taken in consecutive runs. As this latter result appears to deviate from the trend of all of the other bias settings, it seems reasonable to suggest that this may have also been taken under low noise conditions, which resulted in an improved timing resolution.

From the above results, it can be concluded that in order to obtain the best possible timing resolution from the diamond detector, a bias of at least 600 V should be applied to the detector, and the noise levels should be as low as possible.

5.1.3.2 Choosing Between Discrimination Methods

Signals from the best performing pair of strips were first processed using a LED, the thresholds for which were varied to optimise the performance of the detectors. The LED was then replaced with a CFD, and the thresholds were once again varied. The bias applied to the strips remained at a constant value of 600 V throughout the discriminator comparison tests to ensure that any bias dependence did not influence the results.

The timing resolutions (FWHM) obtained using the LED and CFD at different thresholds are given in Table 5.1. These results confirm that data processed by the LED produced the best timing resolutions, and LEDs should therefore be used for all future diamond detector experiments.

The noise level in the experimental cave was found to be around 40 mV for the majority of the experiment, so it is no surprise to see that the best resolution was achieved when the threshold of the LED was set to this value. The timing

Discriminator	Threshold (mV)	Resolution (ps)
LED	50	174
LED	40	165
LED	30	182
CFD	50	527
CFD	40	494

Table 5.1: Timing resolution measurements taken with data processed by either LEDs or CFDs at different threshold voltages.

resolution obtained with a threshold voltage of 50 mV was worse than that obtained with a threshold of 40 mV due to an increase in signal walk at the threshold level. However, lowering the threshold level to 30 mV, i.e, a value below the noise level, allowed erroneous timing signals to enter the data stream, increasing the width of the timing peak and the resultant timing resolution.

The exceptionally high timing resolution obtained using constant fraction discrimination suggests that the CFD was not optimised to be used with the diamond detectors. Unlike LEDs, CFDs require a delay input, the duration of which is defined by the length of the delay cable. Ideally, the duration of the delay should be equal to the time taken for the pulse height to increase from the threshold value to its full peak height, which for signals from a diamond detector should be around 1 ns. If the delay created by the delay cable was longer than this, the zero-crossing point shown in Figure 3.5 may have been formed on the falling edge of the pulse, which can vary considerably from pulse to pulse. If this was the case during the experiment, this could explain why the timing resolution was found to be so poor for the data processed by the CFD.

5.1.3.3 Best Timing Resolution

The best timing resolution measured from the TAMU data was found to be **147 ps** (FWHM), which corresponds to a resolution of **104 ps** (FWHM) for each individual diamond detector, under the reasonable assumption that each detector contributed to the timing resolution equally. The timing peak and Gaussian fit used to obtain this result can be seen in Figure 5.5. The time values shown on the x-axis of this histogram represent the time difference between the start and stop signals (front and back detectors respectively) reaching the TDC, which is greatly influenced by the amount of cable the signals had to travel through on their way to the TDC. It is, therefore, not a time of flight measurement, but could easily be converted into one

by applying a correction offset that accounts for the differences in cable length. This was not deemed necessary for this analysis, as it has no affect on the measurement of the resolution, which is defined only by the width of the timing peak.

The tail seen to the right of the peak in Figure 5.5 may have been caused by low amplitude, late stop signals from the back detector, however, as the height of the signals could not be measured during this experiment, it is difficult to confirm whether this is the case.

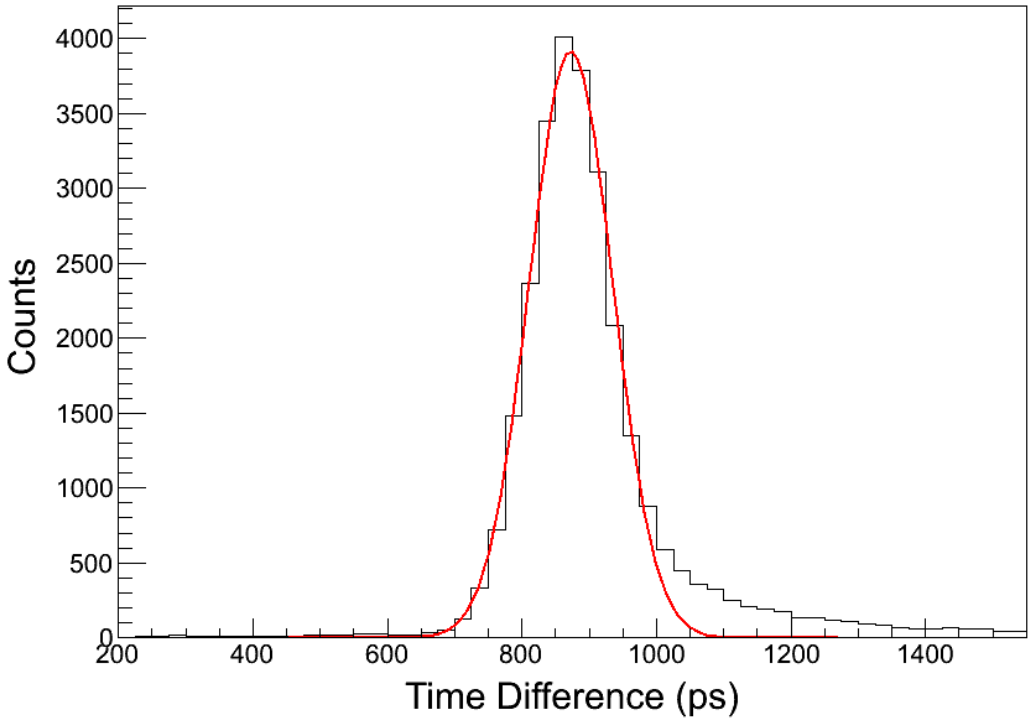

Figure 5.5: Timing peak and Gaussian fit for the best timing resolution result from the TAMU data. The combined timing resolution was found to be 147 ps, which corresponded to a resolution 104 ps for each individual diamond detector.

The ^{40}Ar beam used to obtain the above result was found to contain a small percentage of contaminants such as ^{39}Ar, ^{38}Cl and ^{39}Cl that had been able to pass through the MARS separator. Ordinarily, these contaminants could be eliminated from the analysis using data from identification detectors placed at MARS, however, as the timing data from the diamond detectors was not synchronised with those data, there was no way of distinguishing between the ^{40}Ar beam and other unwanted fragments.

With a flight path of only 15 mm between front and back detectors, the dif-

ference in ToFs for these contaminants was expected to be very little, and could certainly not be resolved in the timing histograms. As a result, the presence of the contaminants would cause the timing peak to widen slightly.

When the energy loss of the contaminants in the front diamond detector is taken into account, the largest deviation in ToF from the expected ^{40}Ar ToF value was found to be caused by the ^{39}Ar contaminant, which travelled between the detectors 13 ps faster than ^{40}Ar . It therefore seems reasonable to suggest that timing resolution measured from the peak in Figure 5.5 may have been affected by the presence of contaminants in the beam, and the diamond detectors may, in fact, have a better resolution than the 104 ps obtained from the data. Whether the resolution of the diamond detectors would be below the desired 100 ps (FWHM) without the effects of the contaminants, however, is not clear.

Nevertheless, the resolution achieved by the diamond detectors at TAMU was encouraging. The problems encountered with the Al contacts and preamplifier breakdown alludes to the fact that improvements could be made to both the contact fabrication technique, and the PCB used to take the signals from the diamond detector strips. With these issues resolved, it was thought that a detector resolution of less than 100 ps could be achievable for the diamond start detector during the LYCCA-0 commissioning experiment.

5.1.4 Results from ^{20}Ne Beam

A 20.8 MeV/u beam of ^{20}Ne was also used during the TAMU experiment with the aim of observing how the energy deposition in the diamond detector affects the timing resolution.

A large proportion of the ^{20}Ne beam was found to be contaminated with ^{16}O, which became evident when two peaks were observed in the timing histograms from the diamond detectors. These peaks were thought to originate from the different speeds at which the ^{20}Ne and ^{16}O fragments travel between the front and back detectors, with the lighter and more energetic ^{16}O fragment travelling faster, and therefore creating the peak with the lower ToF value. An example of these peaks can be seen in Figure 5.6.

To confirm whether this phenomenon was caused by beam contamination, the distance between the front and back diamond detector was increased from 15 mm to ∼30 mm to examine what would happen to the position of the two peaks. If beam contamination was to blame, the difference between the ToF of the ^{20}Ne and

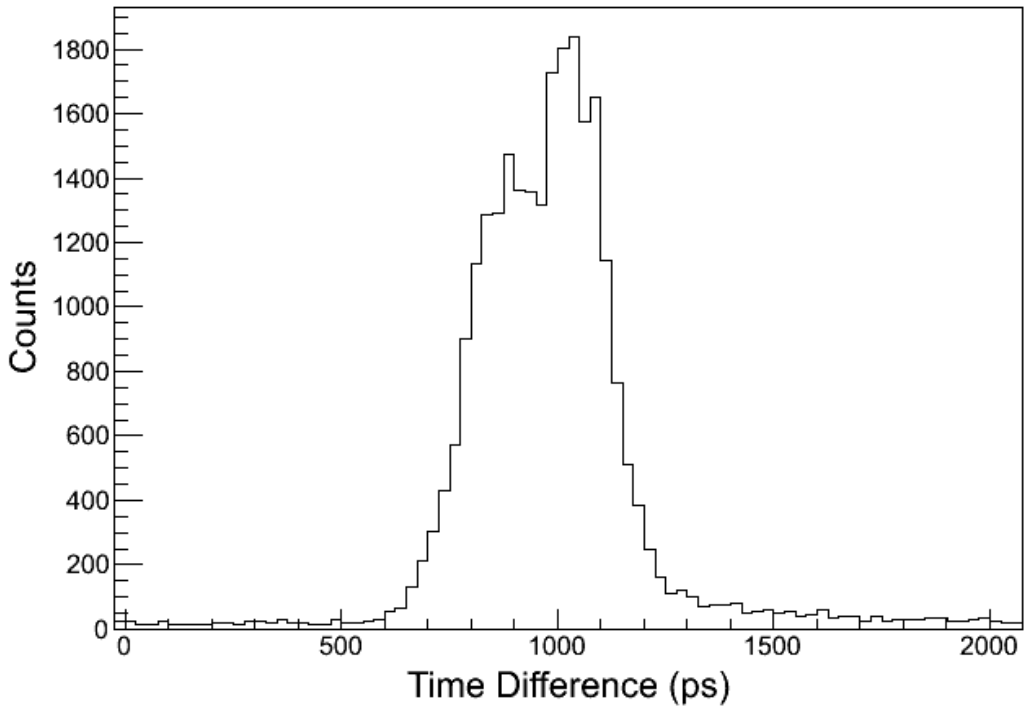

Figure 5.6: Example of the two peaks found in the timing histogram for the ^{20}Ne beam when the separation between the diamond detectors was ∼15 mm. The second peak was thought to arise due to ^{16}O contamination in the beam.

the ^{16}O fragments should increase, causing the peaks to move apart. As can be seen in Figure 5.7, increasing the length of flight path between the two detectors by a factor of two caused the separation between the two peaks to increase from ∼150 ps to ∼300 ps, which agrees well with the beam contamination hypothesis and demonstrates the detector's capability to distinguish between fragments of similar mass, even over a minuscule flight path.

The ^{20}Ne beam was expected to deposit energies of 367 MeV and 49 MeV in the front and back detectors respectively, which were much lower values than the energies deposited by the ^{40}Ar beam. A measurement of the timing resolution was taken from both peaks in the ^{20}Ne data so that a comparison could be made to the best resolution obtained from the ^{40}Ar beam.

Timing resolution measurements were made using the peaks shown in Figure 5.7, as the larger separation between the peaks made them easier to fit. The resultant Gaussian fits can be seen in Figure 5.8. Three Gaussian fits were combined to form the final fit seen in this figure. A wide fit was made to the background, on top of

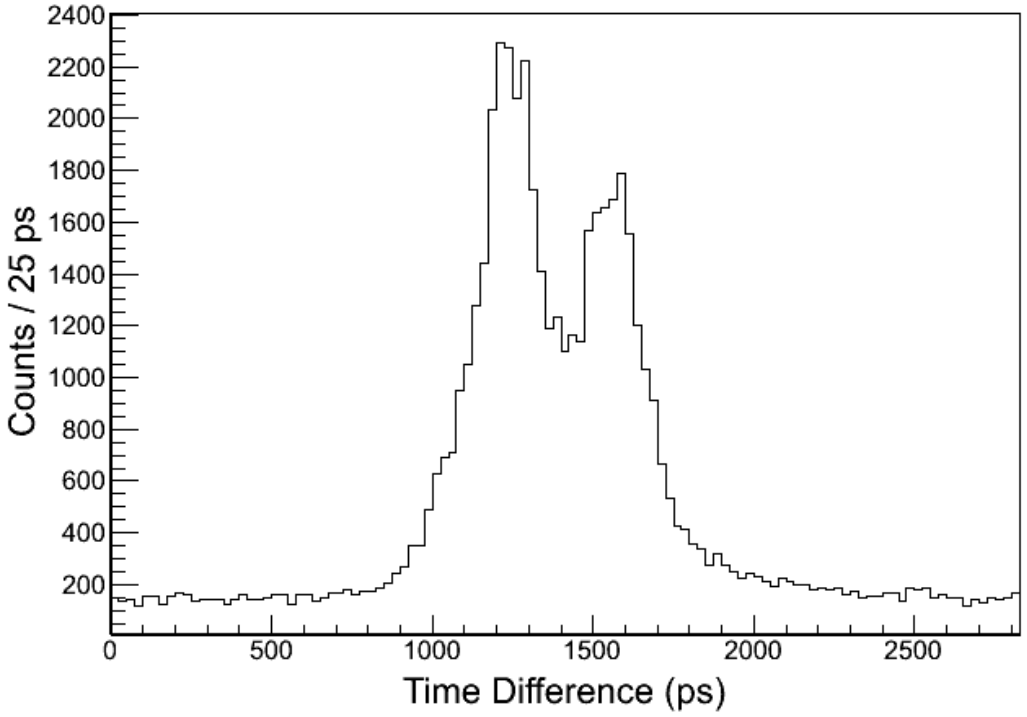

Figure 5.7: Increasing the length of the flight path of the fragments to ∼30 mm caused the two peaks to separate, which provides evidence that the peaks correspond to different fragments in the beam. The peak with a lower time difference is thought to arise from ^{16}O contaminants, whereas the right hand peak is caused by the ^{20}Ne beam.

which two further Gaussian fits were made to each of the peaks. This method was found to give the most accurate fit to both peaks simultaneously.

The σ parameter extracted from the peak on the left, thought to correspond to the ^{16}O fragments, had a value of $\sigma = 101$ ps, or a FWHM value of 236 ps, whilst the Gaussian width for the right hand peak, thought to correspond to ^{20}Ne, was found to be $\sigma = 84$ ps, which gives a FWHM of 196 ps. These timing resolution measurements produce detector resolutions of 167 ps and 139 ps for the left and right peaks respectively.

The individual detector timing resolutions obtained from the ^{20}Ne beam were worse than the 104 ps resolution measured from the ^{40}Ar data, however, the ^{20}Ne data were taken using a bias of 400 V, whereas the ^{40}Ar data used a higher bias of 470 V. If a true comparison between the two data sets is to be made in order to discover the effects of energy deposition on the resolution, measurements taken at the same bias should be used. The timing resolution from the ^{40}Ar data at a

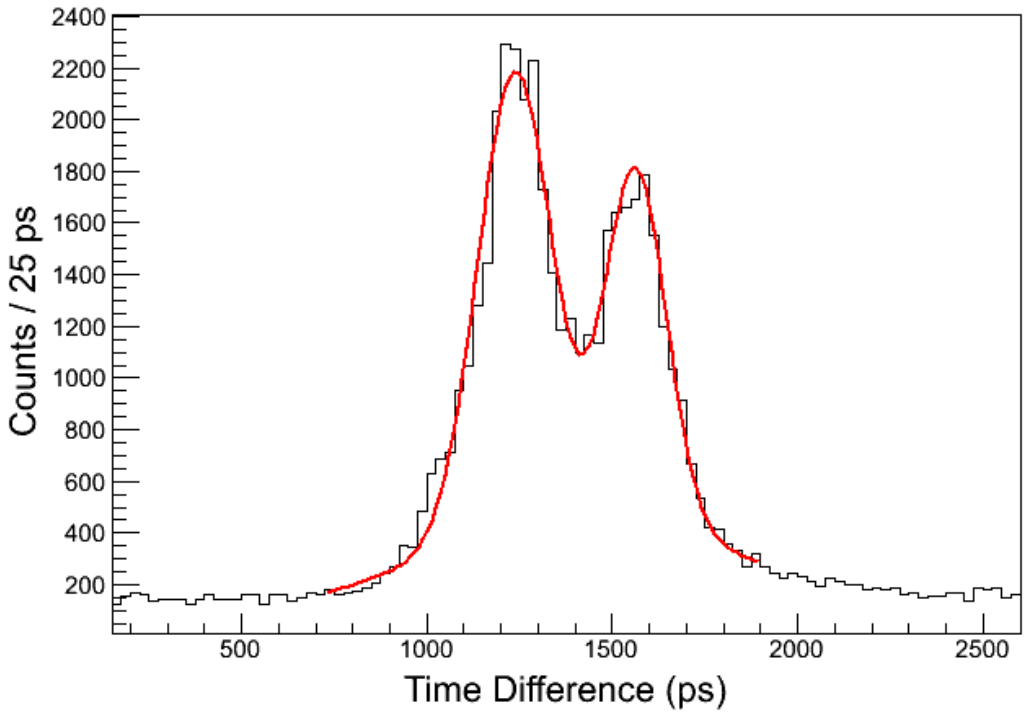

Figure 5.8: Fit made to the ^{20}Ne and ^{16}O peaks. The widths of the Gaussian fit made to each peak were extracted to find the timing resolution, which was then compared to timing resolution measurements obtained from the ^{40}Ar data to examine how the energy deposition in the detector affects the resolution.

bias of 400 V was found to be 143 ps per detector, which is an improvement on the ^{20}Ne results. One must also consider that the ^{40}Ar data contained contaminants that serve to worsen the timing resolution result, whereas the peaks in the ^{20}Ne data contained just one fragment. Overall, the results suggest that increasing the amount of energy deposited in the diamond detectors improves their timing resolution.

5.2 University of Birmingham Experimental Results

5.2.1 Pulse Shape Analysis

The main aim of the optimisation experiment at the University of Birmingham was to study how the pulse shape of the diamond detectors changed with capacitance and contact material, and what effect this had on the timing resolution of the detectors.

The analysis focused on the rise time and the pulse height of the detector signals, which were recorded using two wide bandwidth oscilloscopes that were able to sample at a rate of 20 GHz for two input channels.

The oscilloscope triggers were set just above the noise level at values between 20 - 30 mV so that only detector signals with pulse heights above this trigger level were recorded. The analysis undertaken on the saved waveforms tried to imitate the operation of a leading edge discriminator by applying a threshold voltage gate to the pulses so that only those with a pulse height greater than the threshold were accepted for further analysis. These threshold gates were varied from 20 mV to 60 mV in steps of 10 mV.

The waveforms were plotted onto histograms using 50 ps wide bins to replicate the 50 ps precision of the oscilloscopes. In order to calculate the rise time of an accepted pulse from these histograms, the pulse height, V_{pulse}, of the waveform first needed to be determined. A constant fit was made to the background away from the main pulse, to obtain a value for the baseline voltage, V_{base}. The pulse height could then be found by subtracting the lowest voltage value in the histogram, V_{min}, from V_{base}, as can be seen schematically in Figure 5.9.

A crude measurement of the rise time was obtained by finding the difference between the time at which the pulse reached $0.1V_{pulse}$ and $0.9\ V_{pulse}$ (see Figure 5.9). However, due to the binning of the histogram, this value could only be measured to a precision of, at best, 50 ps, which leads to an error of 5 % if one assumes a rise time of 1 ns. To improve this measurement, cubic interpolation was performed over a range of four bins closest to, and including, the bins that correspond to voltages of $0.1V_{pulse}$ and $0.9V_{pulse}$. This produced an estimate of the time at which the desired voltage was reached within the 50 ps wide bin, resulting in a more precise rise time measurement.

5.2.2 Results for Capacitance Dependence

Figure 5.10 shows the average rise time as a function of detector capacitance at three different bias settings of 400 V, 500 V and 600 V. There are two conclusions that can be made from this figure, the first is that the rise time is dependent upon the capacitance of the detector, and decreases as the capacitance decreases. Secondly, the rise time appears to have no dependence upon the detector bias, which emphasises that it is the electronic properties of the detector's circuit that is the limiting factor in the rise time, rather than the material of the detector itself.

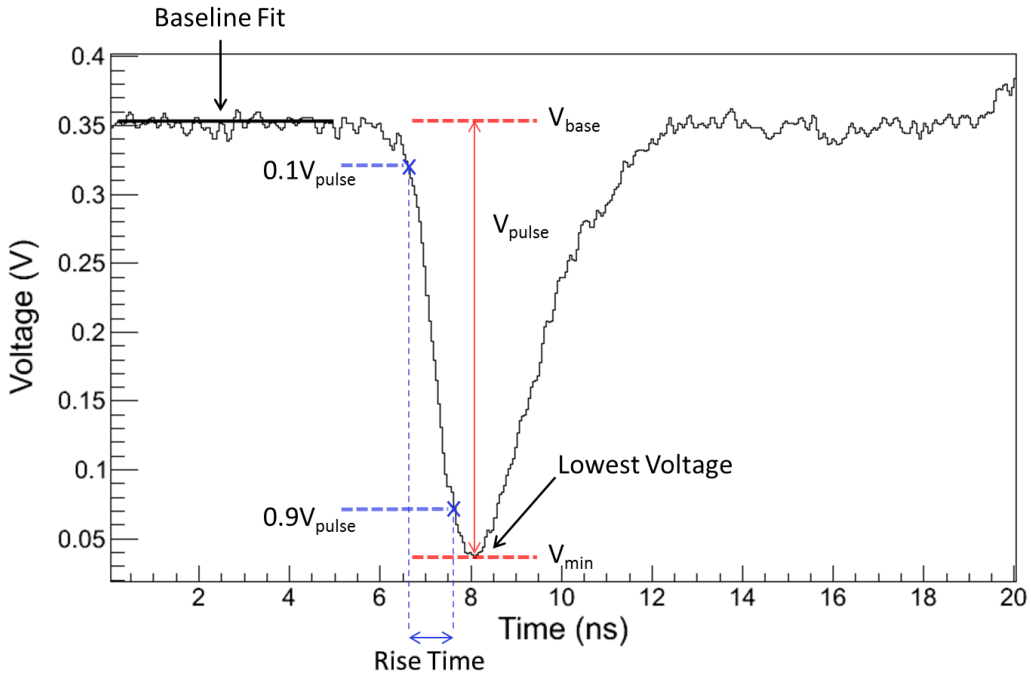

Figure 5.9: A typical waveform plotted onto a histogram. The baseline value, found from the baseline fit to the noise, and the lowest voltage point were used to calculate the full pulse height, as is shown schematically in red. A schematic description of the process used to calculate the rise time of the pulse is also shown in blue.

The bias independence of the rise time seems a contradictory result at first, as the results shown in Section 5.1.3.1 indicate that the timing resolution of the detectors improves as the bias is increased from 300 V to 600 V. However, if we consider what is happening in terms of current, as seen by the current sensitive preamplifiers, rather than charge, both results can be explained.

If saturation velocity has not been reached, increasing the bias across a detector causes the velocity of the charge carriers within the diamond to increase, which leads to a larger induced current on the electrodes, and a larger current pulse at the output of the preamplifiers. This larger pulse means that any signal walk seen at the threshold of the LED is reduced, which results in less variation in the start and stop timing signals, and an improved timing resolution. This description also explains why the timing resolution was found to improve as the energy deposition in the diamond detector increased. A greater number of charge carriers are created when the energy deposition increases, which leads to larger induced currents on the detector electrodes.

The capacitance of the detector determines how quickly the induced current

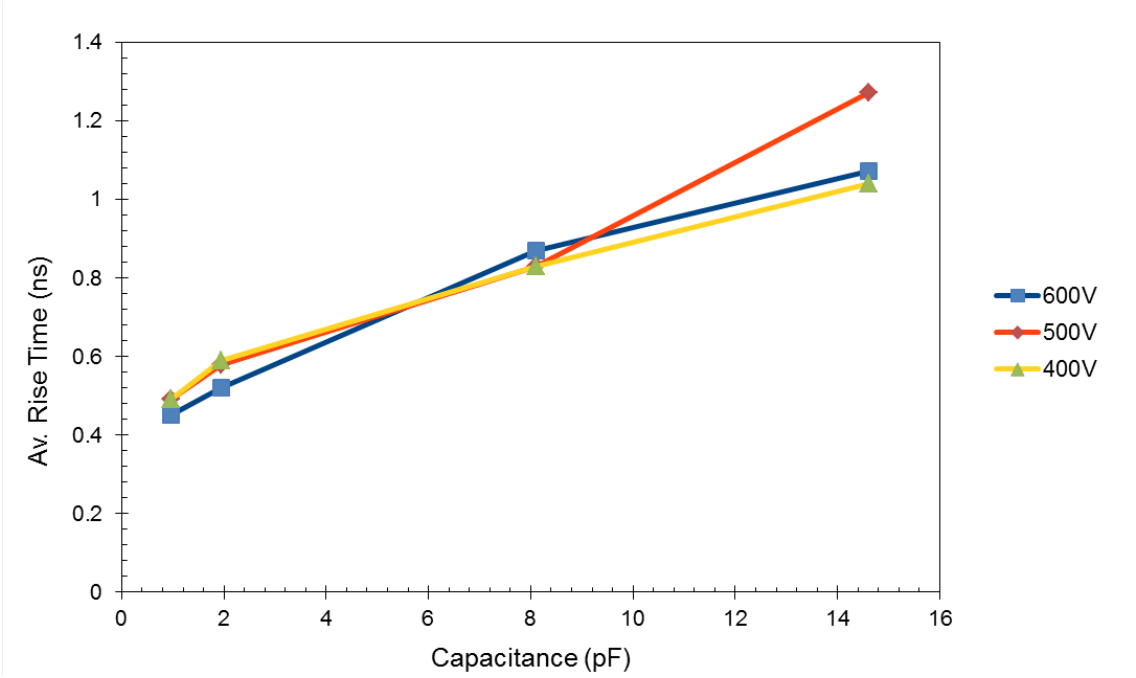

Figure 5.10: Plot showing the dependence of the rise time of a signal on the capacitance of the detector for three different bias settings (400 V, 500 V and 600 V). The main points to note are that the rise time decreases as the capacitance decreases, and that there seems little correlation between the rise time and the bias.

charges and discharges the electrodes of the detector, which appears to be the only limiting factor for the rise time of the signal from the diamond detectors. Increasing the amount of current induced on the electrodes by changing the detector bias should not affect the time taken to charge the electrodes, as the bias bears no relation to the detector capacitance. This explains why the rise time was seen to be independent of the detector bias.

5.2.3 Pulse Height Results

5.2.3.1 Correlation with Rise Time

The pulse height, V_{pulse}, of a signal was plotted against its rise time to determine whether a correlation between the two properties existed. Figure 5.11 shows the resultant plot using pulses taken from pad D, the lowest capacitance pad, at a bias of 600 V. A software threshold of 30 mV was applied to the analysis to remove the majority of events that were just caused by noise. It is clear from the form of the locus in the figure that there is no correlation between the pulse height and rise time of a signal.

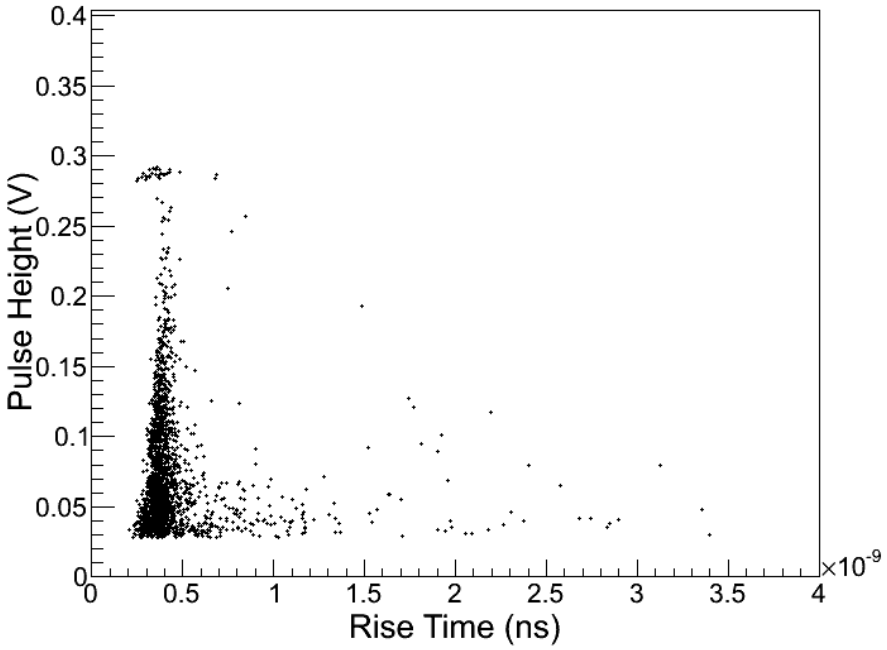

Figure 5.11: Plot showing the relationship between the pulse height of a signal and its corresponding rise time. The vertical nature of the locus clearly shows that no correlation exists between the pulse height and the rise time of the signal.

This result conforms with the explanation given for the bias independence seen in Figure 5.10, and emphasises the fact that the rise time of the current signal only depends upon the detector capacitance, whereas the pulse height is influenced by the detector bias and the energy deposition in the diamond detector.

5.2.3.2 Signal Jitter

A measure of the noise on a pulse, or signal jitter, was obtained by plotting the variation in rise time for different software thresholds. The rise time variation was measured by extracting the σ value from a Gaussian fit made to all rise time results in a data set that passed the software threshold gate. The Gaussian distribution was obtained by projecting the 2D histogram in Figure 5.11 onto the x-axis.

As the rise time has no dependence upon the pulse height of a signal, the rise time of each signal in a data set from the same detector pad at the same bias should be identical. Consequently, any variation in the rise time measurements can only arise from jitter found on the signal. During a rise time measurement, the leading edge of the signal is read off twice and therefore, the rise time variation can be thought of as a sum of the signal jitter from the two readings, combined in

quadrature.

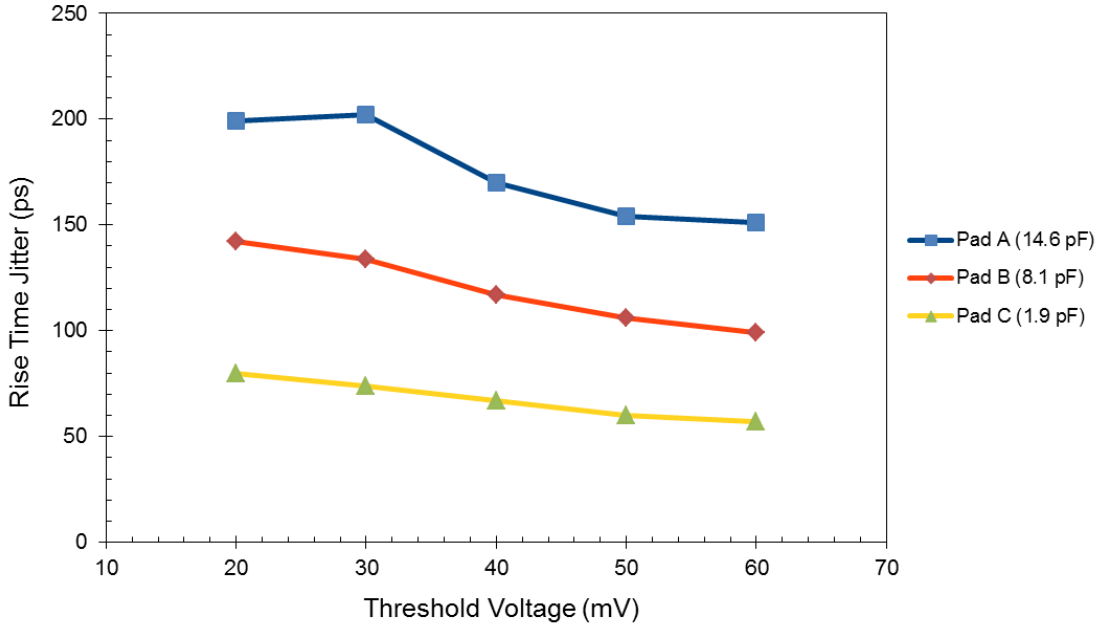

Figure 5.12: Plot showing how the rise time jitter varies with threshold gate for pads A , B and C. The rise time jitter is a measure of the timing noise on the leading edge of the signal, and is found to decrease as the capacitance of the pad decreases, and the threshold gate increases.

Figure 5.12 shows how the rise time jitter varied as the threshold gate was increased for pads A (14.6 pF), B (8.1 pF) and C (1.9 pF). Less jitter was seen on signals from contact pads with lower capacitance, and the jitter also seemed to consistently decrease as the threshold gate increased. Both of these results can be explained by considering how the gradient of the leading edge of a signal affects the signal jitter.

The signal jitter can be described by equation 2.7, and is depicted in Figure 2.15. If one assumes that the level of noise on the signal, σ_n, remains unchanged from pulse to pulse, the time variation, σ_t, becomes solely dependent upon the gradient of the leading edge of the signal. Increasing this gradient whilst keeping σ_n the same leads to a reduction in σ_t, and hence, a reduction in the rise time jitter.

This correlates with the results seen in Figure 5.12. The gradient of the leading edge increases as the rise time decreases and, as a result, the lower capacitance pads with the shorter rise times have less rise time jitter. Similarly, increasing the pulse height of a signal also causes the gradient to increase. By changing the threshold gates from 30 mV to 60 mV, one is effectively limiting the pulse heights to larger

and larger values, and hence, the rise time jitter decreases.

5.2.4 Timing Resolution

Timing measurements were also acquired during the Birmingham experiment using the TDC and an electronics setup identical to that used at TAMU. This allowed a timing resolution to be measured using data from the oscilloscopes and the TDC.

Coincidence measurements between corresponding contact pads on the front and back detectors were acquired on the oscilloscopes so that ToF measurements could be made. The start and stop times were extracted from the waveforms of the front and back detectors respectively by reading off the time at which each pulse reached a threshold voltage of 30 mV, as is depicted in Figure 5.13. The ToF was then obtained from the difference between these two timing values. This process was repeated for each pair of coincidence measurements in a data set, and the ToF results were plotted onto a histogram that formed a Gaussian distribution. The timing resolution was then measured by extracting the width of the distribution using a Gaussian fit.

The above approach was employed as it best replicated the operation of the leading edge discriminator used for acquisition via the TDC, enabling a more realistic comparison to be made between the timing resolutions obtained from the oscilloscopes and the TDC.

Timing resolutions were obtained from the TDC data using the analysis technique outlined in Section 5.1.3.1.

A summary of the timing resolution measurements obtained from each of the four pads of the Au contact diamond detector fabricated at the University of Surrey is shown in Figure 5.14, along with the resolution obtained from the diamond detectors with a diamond-like carbon contact that were fabricated by DDL. Results from both the oscilloscope data and the TDC data are shown.

This plot clearly shows that the timing resolution improves as the capacitance of the detector decreases. As the rise time of the pulses also follows this trend, this suggests that the improvement in timing resolution is a consequence of the faster rise time, which agrees the interpretations given for the other Birmingham test results. A faster rise time obviously produces a leading edge with a steeper gradient, and as the rise time jitter results suggest, this reduces the variation in the timing signal, which ultimately leads to an improved timing resolution.

The main conclusion that can be realised from Figure 5.14 is that the DDL

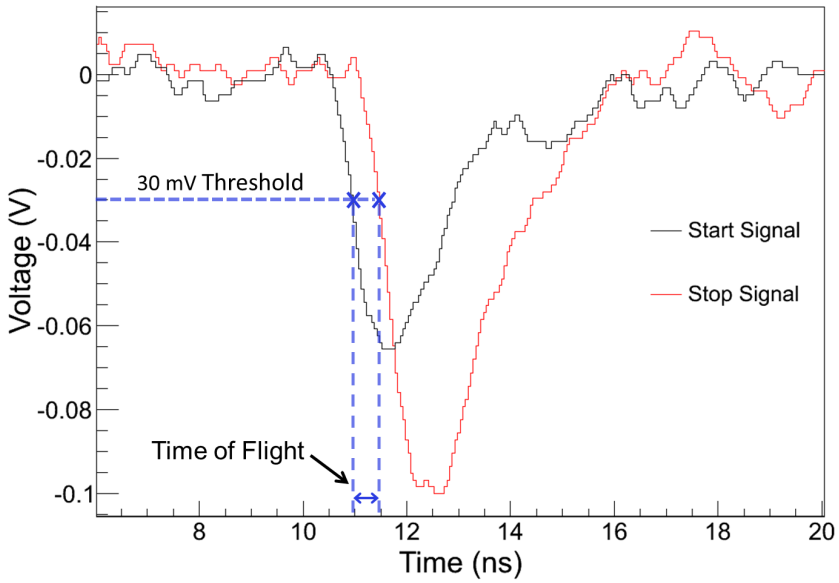

Figure 5.13: Diagram demonstrating how the ToF measurements were performed using waveform data from the oscilloscopes. The times at which the coincident front and back signals reached a threshold of 30 mV were extracted, and the ToF was obtained from the difference between these values.

detectors consistently achieved better timing resolution results than the Surrey detectors of similar capacitance. One assumes that this is as a result of the diamond-like carbon contact material used on the detectors. As the rise time of the signal is determined by the capacitance of the detector, this cannot account for the improved timing resolution measurements seen from the DDL detectors when compared with those from the Surrey detectors. The improvement must therefore originate from an increase in pulse height when compared with a detector of equal capacitance but with a Au contact like those fabricated at Surrey.

As the energy deposition in the DLL detectors was not significantly different from that in the Surrey detectors, the only remaining explanation is that a larger current was induced on the diamond-like carbon contact. The agrees with the premise of the diamond-like carbon contact outlined in Section 2.4.3.2.

As the analysis undertaken on the oscilloscope data tried to replicate the signal processing performed by the leading edge discriminator, one might expect that the timing resolution results from the oscilloscope and TDC analysis to be very similar. However, a discrepancy between the two methods can be seen in Figure 5.14, which arises from the fact that the long coaxial cables used to transfer the output of the preamplifiers inside the experimental area to the oscilloscopes outside of the area

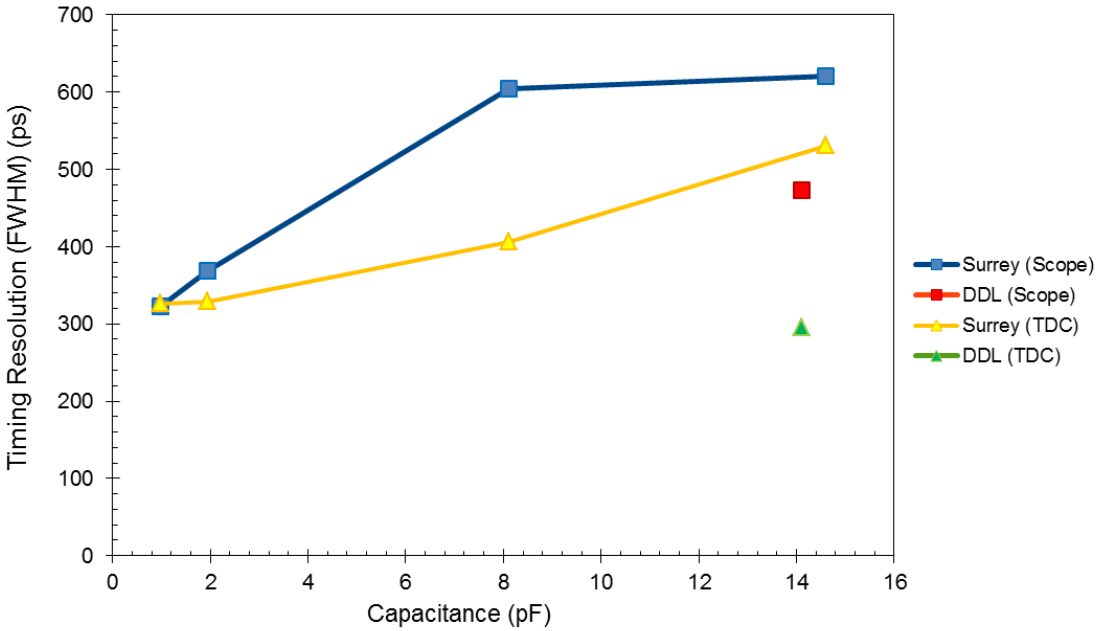

Figure 5.14: Plot showing the timing resolution results as a function of capacitance. The blue and yellow data points represent timing resolution results from the four pads of the detectors fabricated with Au contacts at the University of Surrey, where the red and green data points show the results from the detectors that had been fabricated at DDL with a diamond-like carbon contact. Timing resolutions calculated from the oscilloscope data and TDC data are shown as squares and triangles respectively.

will have attenuated and possibly distorted the signals. As a result, the pulse shape seen by the leading edge discriminator will not have been the same as that recorded by the oscilloscopes, which accounts for the differences seen in the timing resolution results.

The attenuation and distortion caused by the long coaxial cables should not have affected the trends observed from the rest of the Birmingham results presented in this chapter as all of the coaxial cables used to transport the detector signals to the oscilloscopes were of a similar length and therefore imparted similar measures of attenuation and distortion to every waveform. This does mean that the rise time and pulse height values obtained from the data may not be representative of the actual values of the signals seen at the output of the preamplifiers, but values for the upper and lower limits of the rise time and pulse height respectively can be obtained.

5.2.5 Implications of Birmingham Experimental Results

The results from the Birmingham optimisation experiment indicate that it is best to use a diamond-like carbon contact in conjunction with the diamond detector, and this contact should be as highly segmented as possible to reduce the capacitance associated with the detector. Unfortunately, increasing the segmentation introduces a number of problems for a large area detector. Firstly, signals from each segment need to be gathered using bonding wires from the contact onto the PCB. If the number of segments increases, the area of PCB required to cope with the additional bonding wires and PCB tracks would also increase, leading to a larger area of dead space on the detector.

Secondly, increasing the number of segments on the diamond detector also means that the number of channels of electronics needed to process the signals increases, which can be costly. Perhaps more significant, however, is the fact that the number of cables leading from the detector to the preamplifier will have to increase. If one wants to keep the same high frequency and low attenuation cables used in the optimisation experiments, space will quickly become very limited inside the LYCCA-0 target chamber at GSI, and at a certain level of segmentation, the number of cables inside the chamber will become unfeasible. This may also be the case at the future LYCCA setup in the low energy cave at FAIR.

It is therefore clear that for any future prototypes of the large area diamond detector, a compromise must be made between the timing resolution of the diamond detector and the feasibility of the detector segmentation.

CHAPTER 6

Results: LYCCA-0 Commissioning Experiment

This chapter details the analysis undertaken on data from the very first LYCCA-0 commissioning experiment, which took place at GSI, Germany in September 2010. The experiment was devised to provide a proof-of-principle study of the LYCCA-0 detector system, and determine its performance in terms of mass, charge and individual detector resolutions.

Comparisons between the plastic ToF and the diamond ToF options for LYCCA-0 will be made, which can only be done by gating on various aspects of the data in order to control any energy and mass dependence of the timing resolutions of these options. The implications of the results presented in this chapter are discussed in Chapter 7.

6.1 Identification of Incoming Particles

Z vs. A/Q histograms were used to identify fragments passing through the FRS, and impinging upon the secondary target. An example of the identification plot used for the ^{63}Co beam is shown in Figure 6.1. The most intense area of this plot represents ^{63}Co particles that have passed through the FRS, whereas the less intense oval

areas correspond to other species that may have been generated by fragmentation reactions in the FRS detectors, or contaminants with similar mass and charge to the main beam. The vertical and horizontal lines that can be seen in the Z vs. A/Q histogram are caused by pile-up effects in the MUSIC detectors, which leads to spurious energy loss measurements in the data stream, and consequently, incorrect Z and A/Q values.

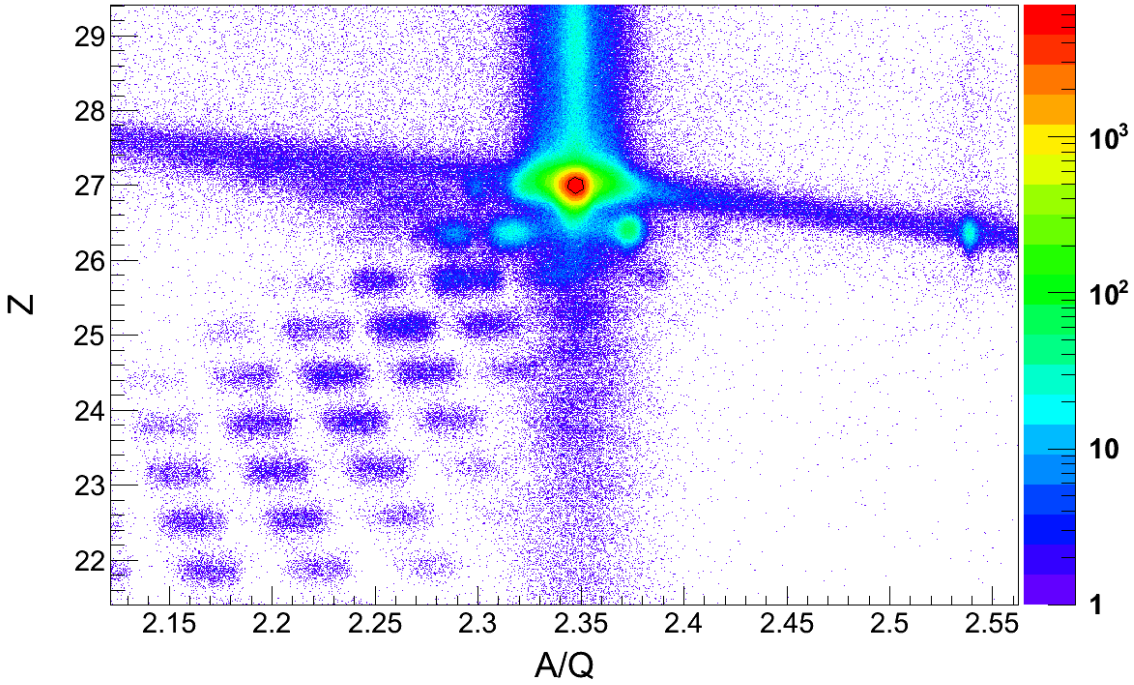

Figure 6.1: Z vs. A/Q plot calculated using ToF, energy loss and position data from the FRS detectors. This plot was used to identify fragments before the secondary target. The gate shown in the centre of the most intense region is used to select incoming ^{63}Co fragments.

A restrictive gate at the centre of the most intense region was created to select incoming ^{63}Co particles, as would be done during the analysis of a typical experiment. This gate, which can be seen in Figure 6.1, was used on all analysis presented in this chapter, unless stated otherwise.

6.2 Z-Measurements After the Secondary Target

The FRS detectors were designed for identifying incoming particles before they hit the secondary target, and with the long flight path of 37 m between the FRS ToF detectors, very good resolution can be achieved. However, these detectors could not

provide any information on the fragments after the secondary target. For this, the LYCCA detectors were required.

The LYCCA-0 energy detectors were used to separate the fragments by their proton number. After calibrating the wall DSSSDs and CsI detectors using the three calibration beams described in Section 4.3.6, the energy loss, dE, measured in the wall DSSSDs was plotted against the residual energy, E_{res}, which is a sum of the total energy measured by the CsI and dE from the wall DSSSDs. The resulting 2D histogram for the ^{63}Co beam is given in Figure 6.2.

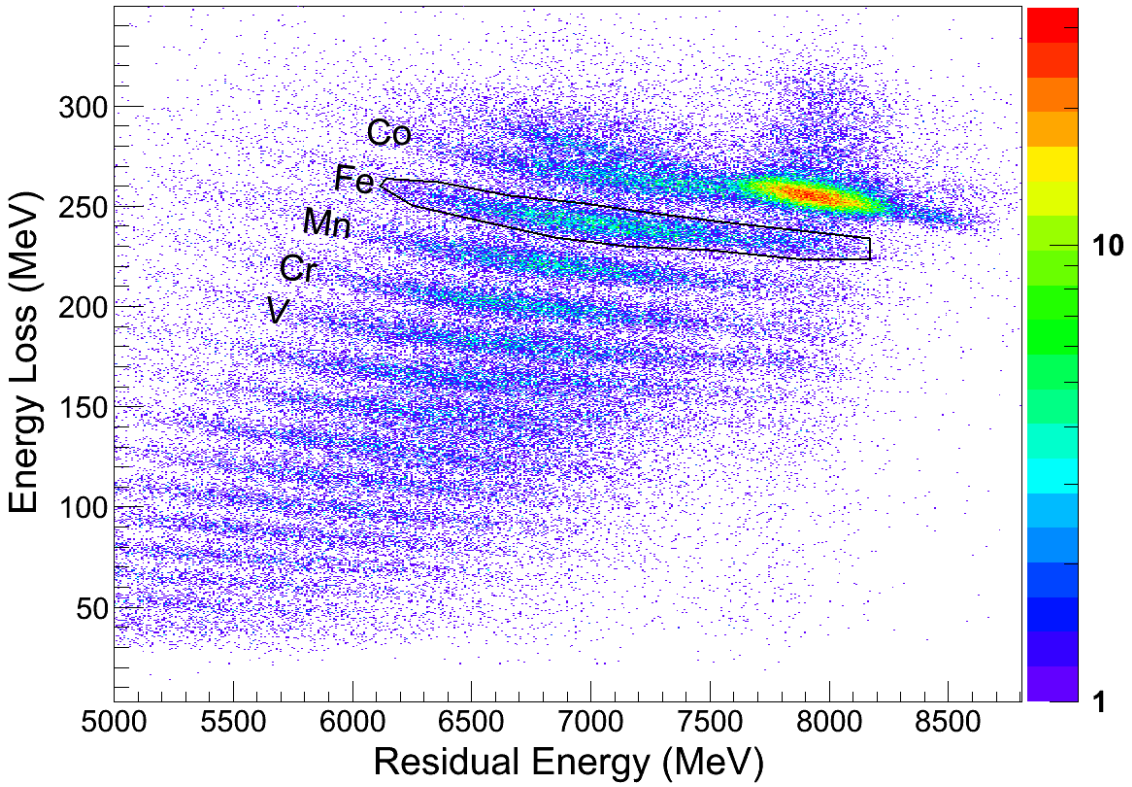

Figure 6.2: dE vs. E_{res} plot for the ^{63}Co beam, created using measurements from the wall DSSSDs and CsI detectors, which separates events into areas of the same Z. The region with the highest number of events corresponds to ^{63}Co nuclei. The other regions represent fragments of lower Z, as have been labelled, and the gate used to select Fe fragments is shown.

A number of fragments can be identified in this plot, from Co down to Al. These were produced in fragmentation reactions that took place within the diamond start detector and the target DSSSD. The reaction rate of fragmentation reactions depends upon the atomic mass and the thickness of material within a detector or target. Intuitively, the rate increases with the thickness of material, and is also

found to increase in materials with lower atomic mass. As a result, the diamond detector, with a thickness of ∼100 mg/cm^2 and A = 12, generates a greater number of fragmentation reactions than the Au secondary target with an atomic mass that is sixteen times greater, albeit with a thickness of 400 mg/cm^2.

Any species can be selected for further analysis by gating on one of the regions formed in this plot, as has been done for Fe fragments in Figure 6.2. For a coulex reaction such as ^{63}Co on a ^{197}Au target, a large proportion of the incident particles pass through the secondary target without any nuclear interaction, and therefore pass through the LYCCA detectors with very similar energy characteristics, forming a confined and intense region of events in the dE vs. E plot. This region can be used to identify the $Z = 27$ events, and the neighbouring isotopes can then be determined.

Energy loss vs. β plots were also used to distinguish between different Z values. An example of such a plot for the ^{63}Co beam is shown in Figure 6.3. As was the case in the dE vs. E_{res} plot, the most intense region of this histogram represents the unreacted beam, and therefore indicates the position of the Z=27 fragments, and each region below this corresponds to the next highest Z value. Details on calculating β shown in this plot from the plastic ToF data can be found in Section 4.5.

6.2.1 Z Resolution

A measurement of the Z resolution was taken so that a comparison could be made between the performance of LYCCA-0 and CATE. The Z resolution of the dE vs. E_{res} plot was measured by projecting the histogram onto the y-axis, and calibrating the dE values to the correct Z values. However, before the histogram could be projected, the quadratic dependence between dE and E_{res} had to be removed and the plot rotated so that each region became parallel to the x-axis. This meant that the widths of the peaks produced in the y-axis projection were representative of the width of each Z region alone, and didn't include any contribution from the diagonal nature of the regions.

Markers were placed along the centre of the Z=26 region of Figure 6.2, as can be seen in Figure 6.4. It should be noted that the colour of Figure 6.4 has been changed from that shown in Figure 6.2 to aid the visual appearance of the markers. The dE and E_{res} measurements taken from these markers were then used to generate a quadratic fit that matched the data well, and a poorly fitting linear fit.

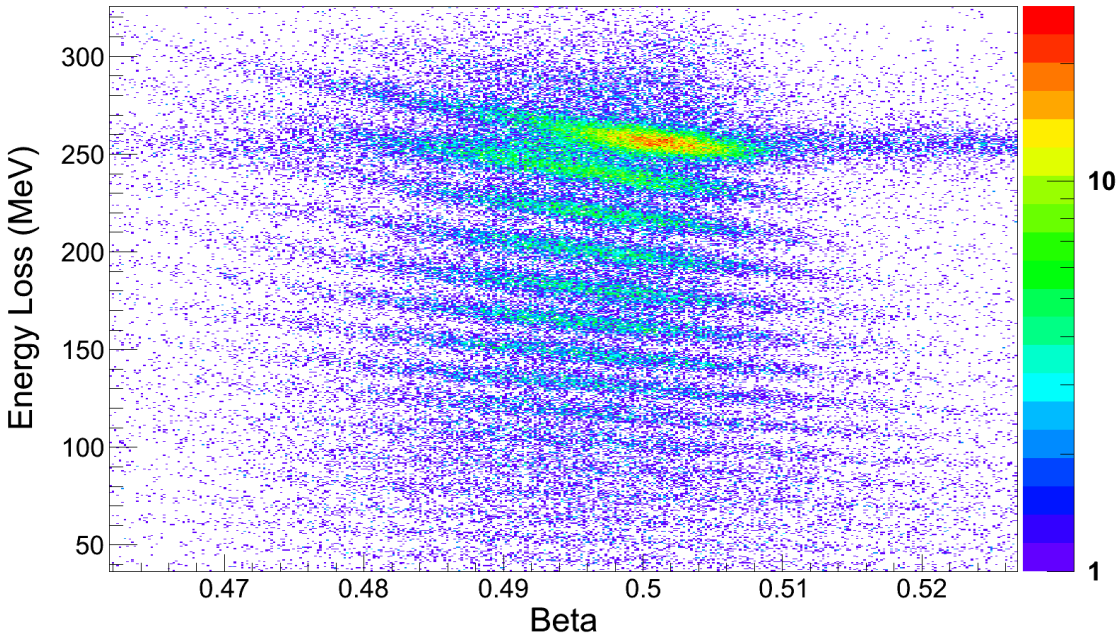

Figure 6.3: Energy loss vs. β histogram for the ^{63}Co beam, which provides a second method of identifying the fragments by their charge. The most intense region corresponds to Z=27, with each lower region corresponding to the next highest Z value.

In order to remove the quadratic dependence of the Z=26 region, the dE residuals between the linear fit and quadratic fit were found and added to the original dE measurements. This forced the data found in Z=26 region to follow the trend of the linear fit, removing any quadratic dependence.

The gradient of the linear fit was then manipulated to find the rotation angle needed to horizontally align the Z=26 region with the x-axis. The linearised and rotated plot can be seen in Figure 6.5a. As the quadratic relationship between dE and E_{res} is different for each Z region, only the Z=26 fully aligns with the x-axis.

New dE and E_{res} values (dE$'$ and E'_{res} respectively) were calculated using the rotation matrix given below:

$$\begin{bmatrix} dE' \\ E'_{res} \end{bmatrix} = \begin{bmatrix} cos\theta & -sin\theta \\ sin\theta & cos\theta \end{bmatrix} \begin{bmatrix} dE \\ E_{res} \end{bmatrix} \tag{6.1}$$

The calculation was altered slightly to ensure that the plot was rotated about a point found in the Z=26 region.

A y-axis projection of Figure 6.5a was used to convert the energy loss mea-

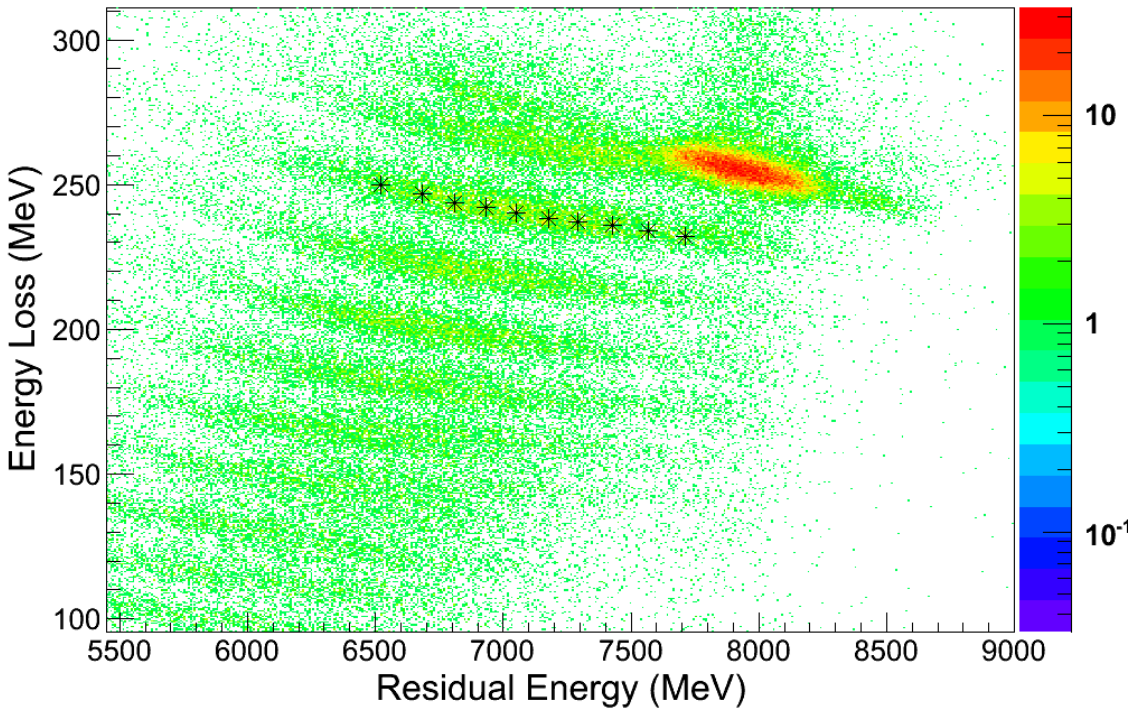

Figure 6.4: Markers were placed along the centre of the Z=26 region found on the dE vs. E_{res} histogram (Figure 6.2). Both quadratic and linear fits were made to the marker positions to remove the quadratic dependence and allow the plot to be aligned with the x-axis.

surements into Z values so that a Z resolution could be obtained. Only events with E_{res} less than 7600 MeV were included in this projection, which eliminated the vast majority of unreacted beam events. This allowed the peaks in the projection to be fitted more easily, as the Z=27 peak could be described by a single Gaussian, created by the reacted fragments, rather than two Gaussian peaks, one of which corresponded to the Z=27 fragments, and the other that corresponded to the unreacted beam. The centroid positions of the four clearest peaks in the projected plot were measured and plotted against the expected Z values. Calibration parameters were then obtained from these data using a quadratic fit in accordance with the Bethe formula, as described in Section 2.3.1.

Applying the calibration to the energy loss measurements produces the plot shown in Figure 6.5b. The quality of the peaks decreases dramatically at values of Z below Z=24 as the linearisation is only based on the Z=26 region. With this in mind, it seemed sensible to extract the Z resolution from the Z=26 peak alone, rather than calculating an average resolution from a number of peaks. To ensure

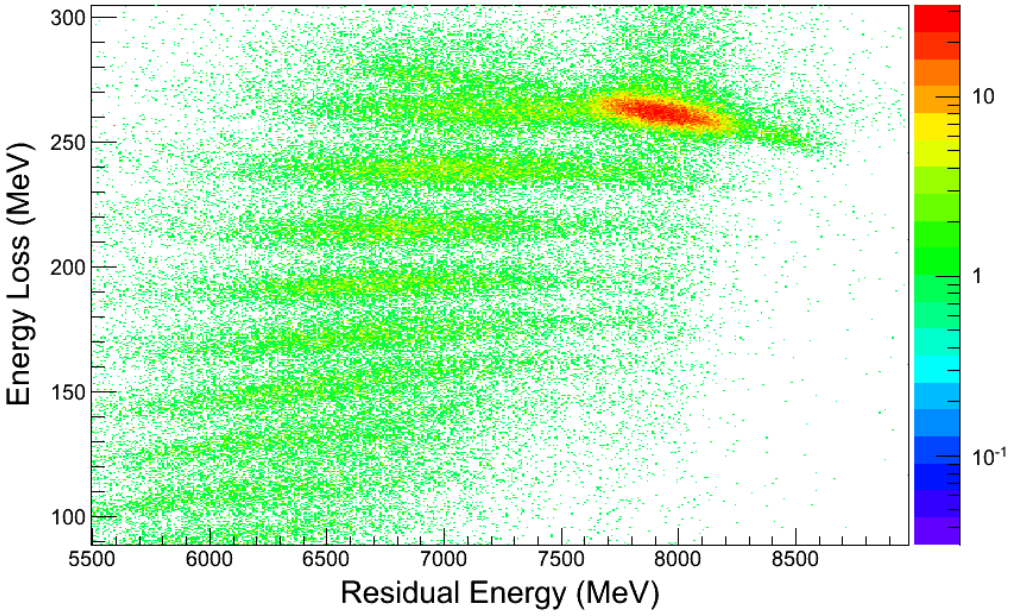

(a) Linearised and rotated dE vs. E_{res} plot

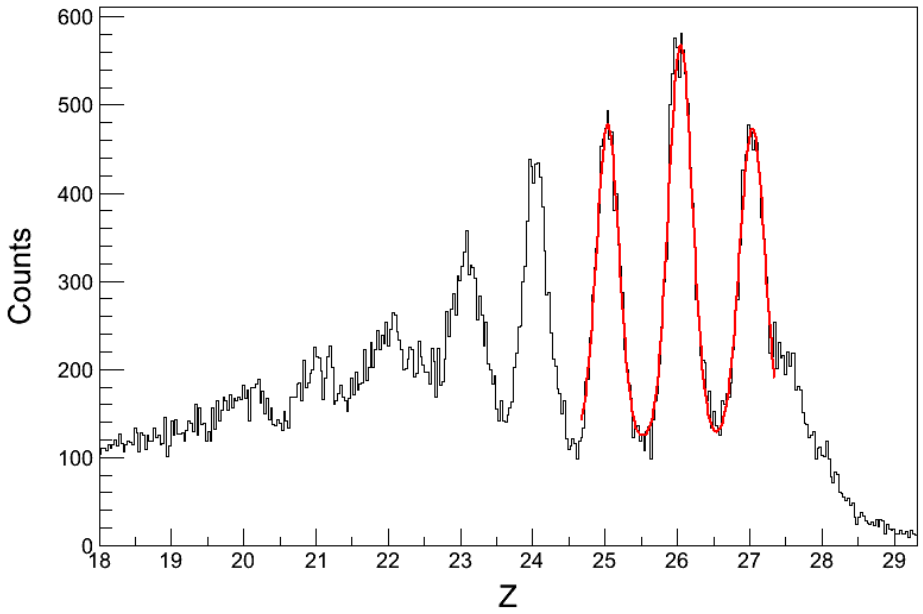

(b) Projection onto y-axis after Z calibration

Figure 6.5: (a) A rotated version of the dE vs. E_{res} plot without quadratic dependence in the Z=26 region. A projection of this plot onto the y-axis was used to calibrate dE with Z to form the final calibrated projection shown in (b).

a reliable fit of this peak, a three Gaussian fit was applied to the Z=27, Z=26 and Z=25 peaks as well as a zeroth polynomial to estimate the background.

A FWHM value of $\Delta Z = 0.39 \pm 0.01$ was extracted for the Z=26 peak. CATE was able to achieve a Z resolution of $\Delta Z = 0.7$ (FWHM) with a 100 AMeV beam of ^{55}Ni onto a ^{9}Be target [11]. The improvement seen in the LYCCA-0 resolution demonstrates the advancements between the development of CATE and LYCCA-0. The main source of improvement probably came from the use of smaller CsI crystals in the LYCCA-0 array, which meant that position corrections did not have to be made to the residual energy measurements.

6.3 Gates Used in Analysis

A number of gates were imposed upon the data prior to further analysis, which ensured that the event corresponded to a fragment event rather than signal noise, a Bremsstrahlung event or other unwanted events. In order to proceed in the analysis, the events must comply with the following criteria:

- The event must have a valid E_{res} measurement, a ToF measurement from both ToF options, as well as position measurements from the target and wall DSSSDs.
- The event must be within the Z vs. A/Q gate for incoming ^{63}Co fragments.
- The event must have similar energy deposition in the front and back strips of the DSSSDs.

The final criterion can be applied by creating a gate surrounding the diagonal region on a plot of front strip energy vs. back strip energy for the DSSSDs, like the one shown in Figure 6.6. Only an event that deposits a similar amount of energy in the front and back strips of the target DSSSD and the wall DSSSD should be generated by a fragment passing through the detector. As a result, gating on events such as these should help to reduce unwanted events.

6.4 Isotope Identification Using Plastic ToF

It was necessary to analyse measurements from the plastic ToF before proceeding onto the diamond ToF data so that the performance and behaviour of the fast plastic

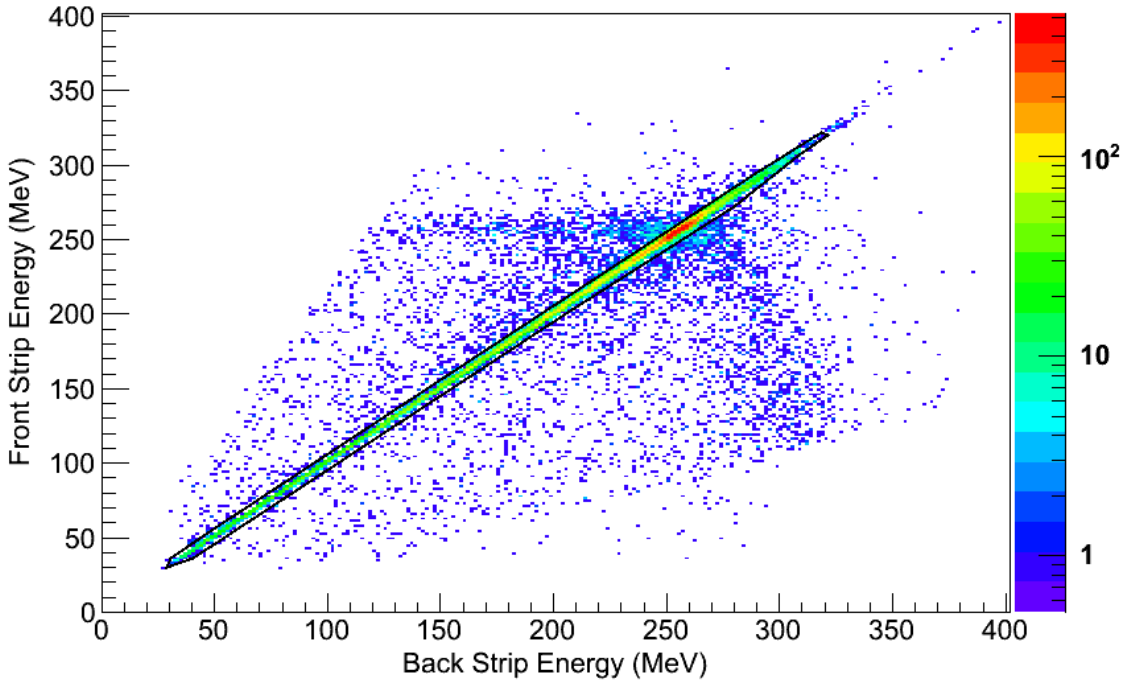

Figure 6.6: Front strip energy vs. back strip energy for one of the wall DSSSDs. The gate placed on the diagonal region of the plot is used to select events with similar energy deposition on the front and and back strips of the detector, which should correspond to an event caused by a passing fragment.

scintillators, which make up half of the diamond ToF system, could be understood. Without this knowledge, it would have been impossible to separate the contributions from the fast plastic scintillator and the diamond start detector to the diamond ToF measurement.

6.4.1 Calculating the Plastic ToF

Every time an ion passed through the start or stop plastic scintillator, up to 32 of the surrounding PMTs fired and sent timing information to separate channels of the TDC. An averaging algorithm was used to convert these raw data into useful ToF information. For each event, data from all 32 channels of the start scintillator were first considered. The multiplicity of the event was calculated by recording the number of channels with timing data greater than zero. This corresponded to the number of PMTs that fired as the ion passed through the scintillator. The non-zero data were then converted from arbitrary bin numbers into picoseconds by multiplying by a factor of 24.4 ps, the width of a single bin of the TDC. A position

correction was than made to each individual timing measurement to account for the distance between the ion interaction and the PMT position (see Section 4.4.2).

The corrected times from all firing channels were then summed together and divided by the multiplicity to obtain an average start time. The same algorithm was repeated using the data from the PMTs of the stop scintillator, and the ToF was calculated by taking the difference between the average start and the average stop time.

6.4.1.1 Calibrating the ToF

The ToF value that arises from the averaging algorithms described above needed to be calibrated so that any differences between the cable lengths used for the start and the stop scintillator could be taken into consideration. This calibration was performed by adding a constant offset to every ToF value, so that the final measurement represented the time taken for particles to pass between the two scintillators, rather than the time difference between data from the two scintillators reaching the TDC.

The offset was calculated using the LISE++ simulation program that used the standard FRS setup with the additional LYCCA-0 detectors placed at the end. Care was taken to ensure that the correct materials and thicknesses were used in the simulation for all detectors, so that the energy loss and beam velocity measurements were very similar to those expected in the experiment. Important distances, such as those between the timing detectors, were measured and added to the simulation to guarantee that any simulated ToF measurements were representative of the experimental data. The simulated ToF between the plastic scintillators was found to be 28.558 ns. This was then compared to the mean plastic ToF value from the uncalibrated experimental data, and the difference between these two values was defined as the ToF calibration offset.

6.4.2 Isotope Identification Plots

An initial isotopic identification was made by plotting the plastic ToF against E_{res}, after applying the gates listed in Section 6.3. Gates on both the dE vs. E_{res} and dE vs. β histograms were used to ensure that the Z value of the events analysed corresponded to that of the desired species.

The cleanliness of the plots was found to improve significantly by restricting the events to those with maximum multiplicity on both start and stop scintillator. Some

of the PMTs surrounding the scintillators failed to work during the commissioning experiment and, as a result, the maximum multiplicity expected from the start and stop scintillators were 30 and 31 respectively. From Figure 6.7, one can see that whilst the majority of events from the start scintillator have the maximum multiplicity of 30, around one third of the data from the start scintillator are found to have a multiplicity of 25. This is thought to be caused by a malfunctioning CFD unit that failed to process five of the channels from the start scintillator.

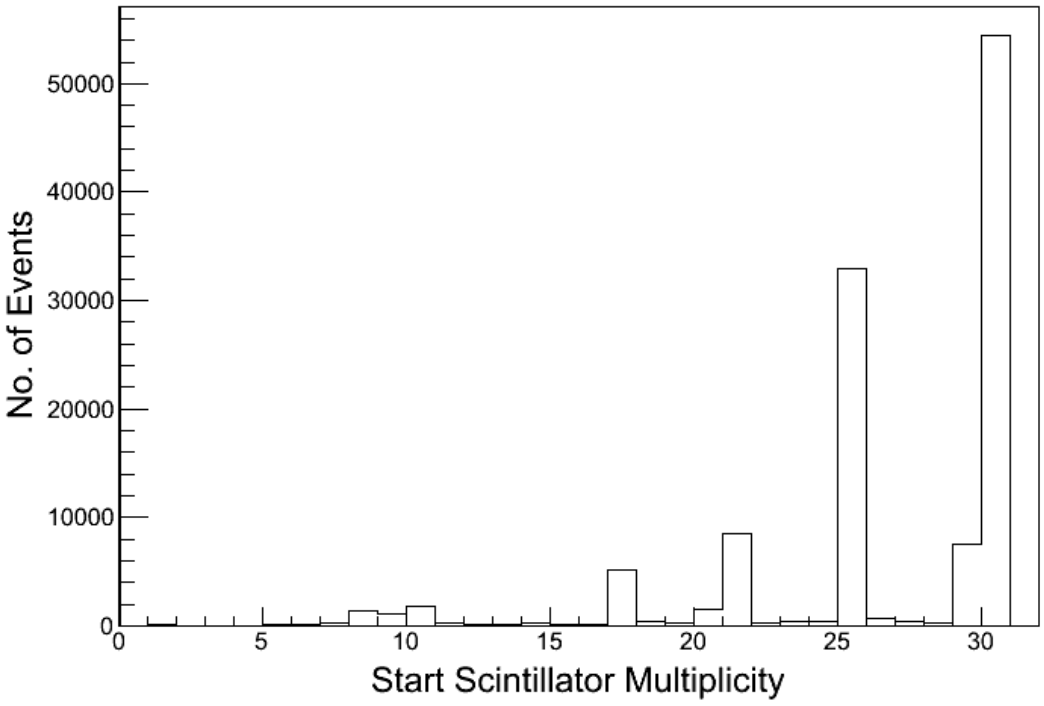

Figure 6.7: Plot to show the distribution of start scintillator multiplicities. For the majority of the events, the maximum number of PMTs fired, however there are also a large proportion of events with a multiplicity of 25. These events will have a less accurate timing measurement, causing the resolution of the plastic ToF to deteriorate.

Lower multiplicity events will be less accurate, as fewer timing measurements are taken simultaneously. Hence, limiting the events to just those with maximum multiplicity on both the start and stop scintillator improves the timing resolution of the plastic ToF, and makes the isotopes on the ToF vs. E_{res} plots more discernible. Although applying these constraints is advantageous, it also considerably reduces the number of events present in the identification plots, which poses a problem when one wants to select these events for gamma-ray analysis of rarely populated states,

as will often be the case in HISPEC experiments.

The cleanest ToF vs. E_{res} plots for the Co and Fe fragments found in the ^{63}Co beam can be seen in Figure 6.8. Similar plots with a slightly less restrictive gate on the incoming ^{63}Co fragments from the FRS are also shown in Figure 6.9. These plots have more statistics, and therefore make the different fragments easier to see, however, they also appear to have worse mass resolution than the cleaner plots.

Similarities can be seen in the shape and dispersion of the fragment regions between the Fe fragment plot shown in Figure 6.8(b) and the simulation of the Fe fragments generated by the LYCCA simulation package [13], which was created assuming an energy resolution of 1 % and a timing resolution of 50 ps over a 3.4 m flight path. Not only does this comparison suggest that the minimum acceptable energy and timing resolution requirements may have been met, but it is also the first piece of analysis to show that including ToF measurements in the design of LYCCA enables differentiation between neighbouring isotopes. It should be noted that the reaction used in the LYCCA simulation is not the same as that used in the commissioning experiment and therefore, the Fe fragments shown in the simulated ToF vs E_{res} (^{50}Fe to ^{53}Fe) will not be in the same mass range as the Fe fragments produced in the commissioning experiment.

The different regions in the Co identification plot were assigned to different Co isotopes by comparing their positions with that of the most intense unreacted ^{63}Co region, and using the knowledge that less massive fragments produced lower E_{res} measurements. The large amount of unreacted beam in the Co plot made it difficult to separate ^{63}Co and ^{62}Co, however lower mass Co fragments could be identified, and are labelled in Figure 6.9.

Identification of the Fe isotopes from these ToF vs. E_{res} plots was much more difficult however, as there was no known marker that could used for comparison. The only way to unambiguously determine which Fe isotopes had been formed was to calculate the fragment mass on an event-by-event basis, and calibrate these mass calculations using the unreacted beam as a reference point. The mass calculations also allowed for a quantitative comparison to be made between the plastic and diamond ToF options in the form of a mass resolution measurement, which cannot be acquired from the ToF vs. E_{res} plots.

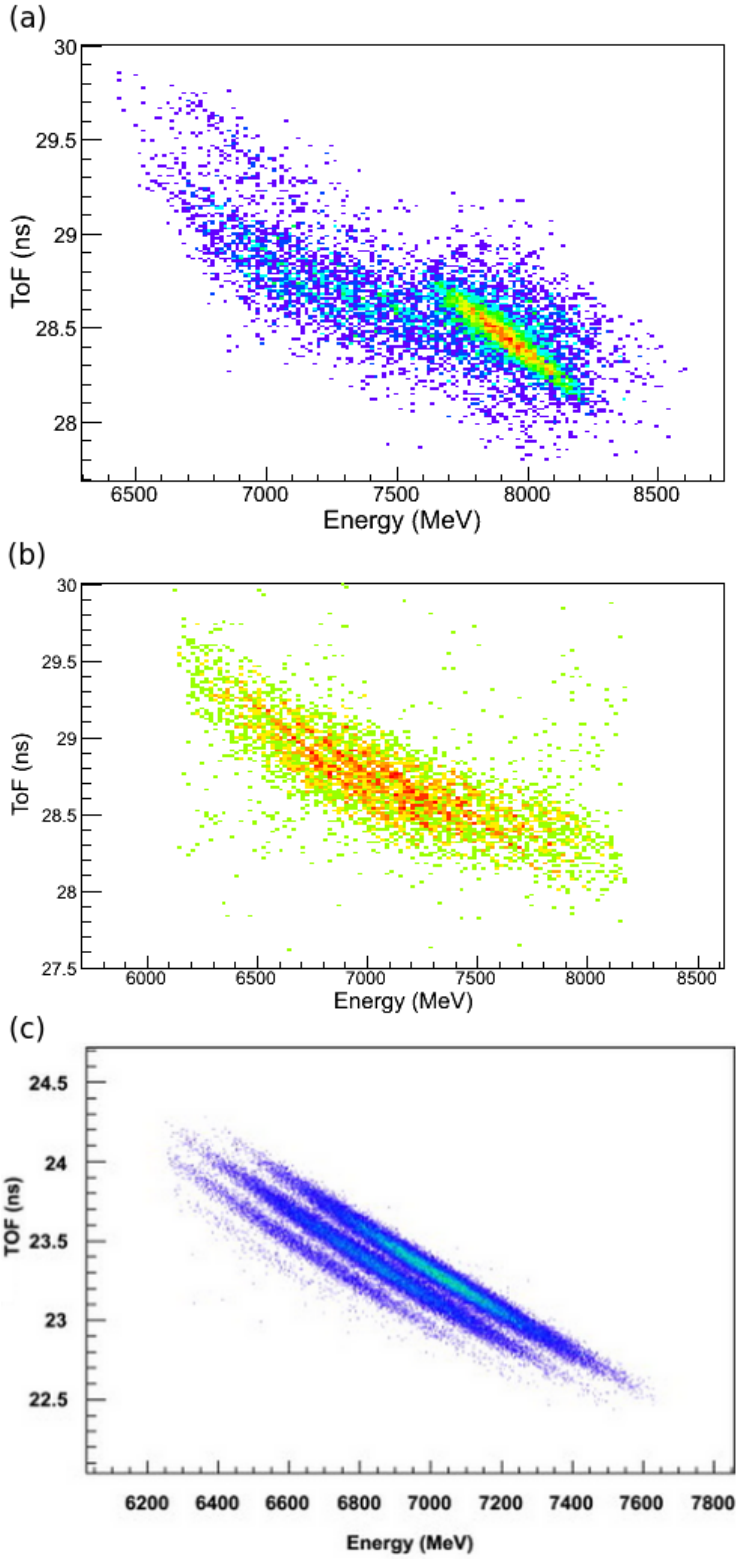

Figure 6.8: ToF vs. E_{res} plots for (a) Co fragments and (b) Fe fragments. These plots were created using a restrictive gate on incoming fragments from the FRS, which created the cleanest spectra. (c) A simulation showing fragments ^{50}Fe to ^{53}Fe which was generated assuming energy and timing resolutions of 1 % and 50 ps respectively.

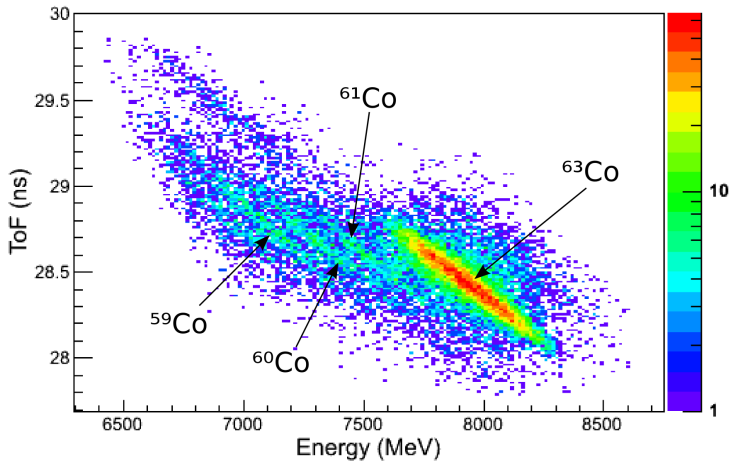

(a) Z = 27

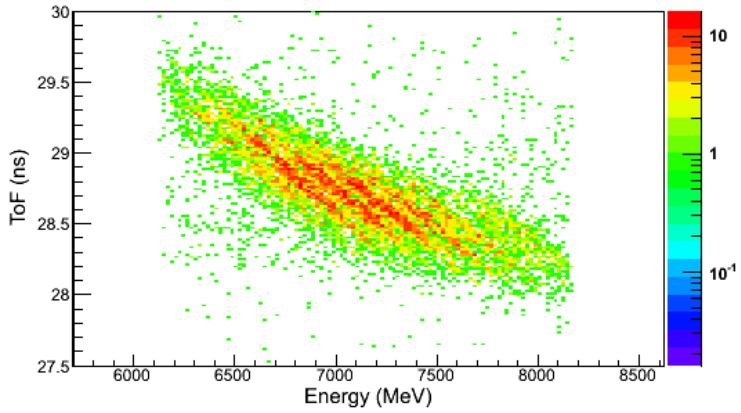

(b) Z = 26

Figure 6.9: Plastic ToF vs. E_{res} plots for (a) Co fragments and (b) Fe fragments. These plots were created using a less restrictive gate on incoming fragments from the FRS, which improves the visual quality of the identification plots, making it easier to see the different fragments, but also worsens the mass resolution. The distinguishable Co fragments are labelled in (a).

6.4.3 Mass Calculations

The co-dependence present between the ToF and energy measurements means that the resolution of the timing detectors cannot be measured without accounting for the resolution of the energy detectors. Mass calculations combine these two measurements and allow the timing resolution to be extracted by obtaining a value for the mass resolution as well as the resolution of the energy detectors.

Equation 4.3 was used to calculate mass values for each event. Once again, the gates mentioned in Section 6.3, as well as Z gates generated on both dE vs E_{res} and

dE vs. β plots were applied. The most restrictive gate on incoming particles was used for these calculations as this appeared to give the best mass resolution when applied to the ToF vs. E_{res} plots.

It was decided that only measurements taken from the most central LYCCA-0 wall module would be used for the mass calculations, so that poor calibration of the outer modules did not compromise the mass resolution. A large amount of calibration data was collected from the central DSSSDs and CsI crystals in the LYCCA-0 wall, but only a small number of events were acquired from the modules found on the outer edges because fewer particles were scattered into these detectors. As a result, the lack of statistics from the outer modules made the calibration peaks difficult to fit, adding a sizeable error to the final calibration values for these modules. Using only the central module with most reliable calibration meant that any contribution to the mass resolution from the DSSSDs and CsI crystals was primarily caused by the intrinsic performance of the detectors, rather than inaccuracies in the detector calibrations.

6.4.3.1 Plastic β Results

The β_{pl} used in the plastic ToF mass calculation (4.3) represents the velocity of the fragments after the secondary target, and was determined from the plastic ToF using equation 4.5. Any differences between particle trajectories from event to event were accounted for by measuring the angles before and after the secondary target, and correcting the length of the flight path accordingly. As a significant percentage of the plastic ToF flight path is found before the secondary target, the LISE++ simulation was used to estimate the β offset required to correct for this. For the ^{63}Co beam, the simulated β values through the fourth dipole and directly after the start scintillator were found to be 0.609 and 0.531 respectively, producing a constant β offset of 0.078. This offset was applied to each FRS β measurement to find β_{before}, which was subsequently used in the β_{pl} calculation.

The distribution of β_{pl} values obtained using equation 4.5 can be seen in Figure 6.10. The relatively large width associated with this distribution arises from the momentum spread that is introduced whenever a fragmentation reaction occurs. It would, therefore, be nonsensical to measure the resolution of β_{pl} from this plot, as the true resolution is obscured by the additional width generated by the momentum spread.

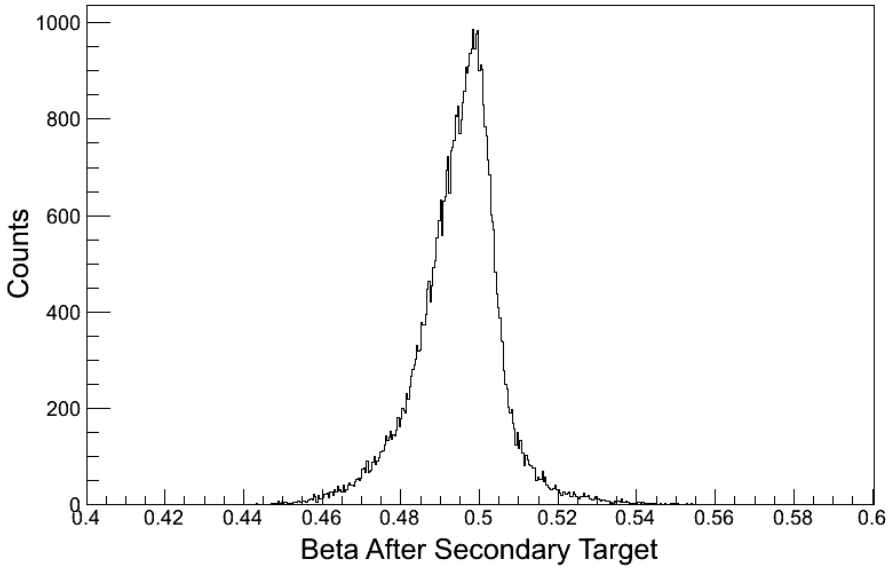

Figure 6.10: Distribution of β_{pl} values that represent the velocity of fragments after the secondary beam as a fraction of c. β_{pl} is calculated from the plastic ToF using equation 4.5, which takes account of the significant percentage of the flight path before the secondary target.

6.4.3.2 Energy Loss Calculations

The energy measurement, E_{total}, used in the mass calculations represents the energy of the fragment during the majority of the flight path, i.e., between the secondary target and the stop scintillator, which was found by summing the energy deposited in the CsI crystals, the wall DSSSDs, the stop scintillator and its shielding foil. The energy loss in the CsI and DSSSD detectors was measurable, but needed to be calculated for the scintillator and foil.

The energy deposited in the scintillator and foil depends upon the mass of the passing ion, and hence, the mass of the fragment must be known before the correct energy loss calculation can be assigned. However, the purpose of this calculation is to obtain the correct mass for the fragment, creating a codependency. To bypass this issue, initial mass calculations were made using the sum of only energy measurements from the CsI detectors and DSSSDs. Theses masses were then calibrated using the methods described in Section 6.4.4, so that mass gates could be applied to determine the energy loss in the Al shielding foil.

As only the energy of the fragment as it exited the Al foil was known (the sum of the CsI and DSSSD energy measurements), stopping power calculations could

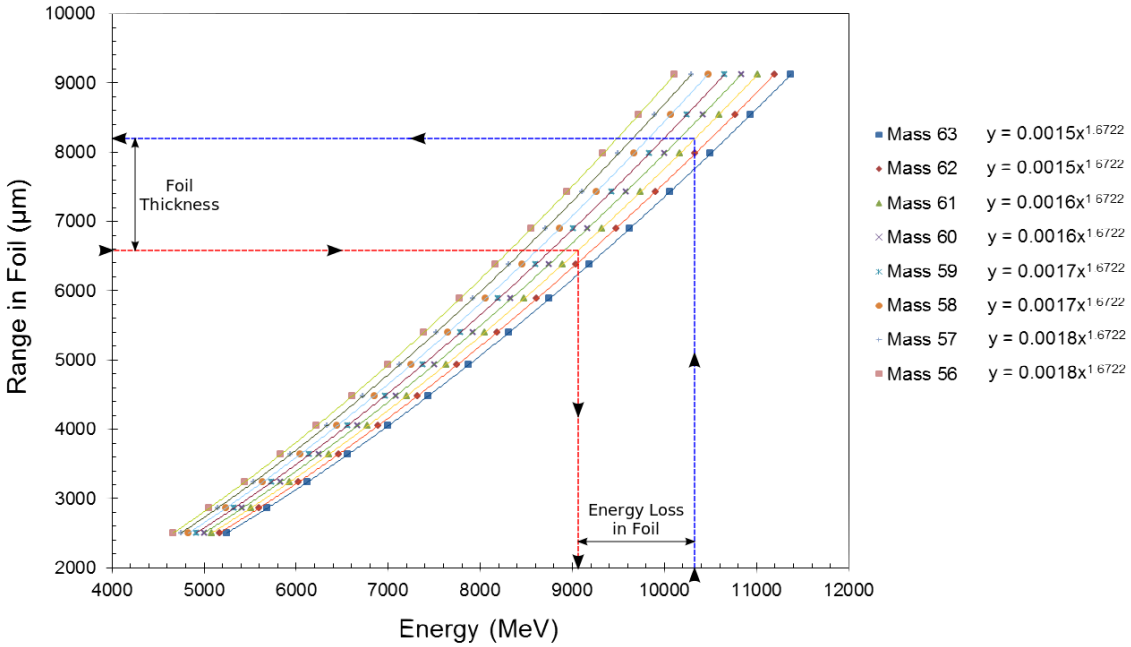

Figure 6.11: Range in Al foil vs. fragment energy for Co isotopes. The known exit energy of the fragment and foil thickness are used to find the energy of the fragment as it enters the foil, and hence, the energy loss in the foil.

not be used. Instead, backward interpolation was performed on range calculations made by ATIMA (ATomic Interactions in MAtter) [50], a program developed by GSI for calculating energy loss and straggling in matter that is incorporated into the LISE++ simulation program. The range in Al was plotted against fragment energy for isotopes ^{63}Co - ^{56}Co, as can be seen in Figure 6.11. This figure also demonstrates the backward interpolation method used to find the energy loss in the Al foil. By tracing a line up from the exit energy of the fragment to the plot corresponding to the correct fragment mass, the equivalent range in Al can be found (blue line). If one was to then subtract the thickness of the foil, in this case 100 μm, from that value, and repeat the tracing process in the opposite direction (red line), the energy of the fragment as it enters the Al foil can be identified, and the energy loss calculated. It should be noted that the thickness of the foil is exaggerated in Figure 6.11 for visual purposes.

This method was employed in a mathematical manner for this analysis by fitting each of the data sets and obtaining eight different equations that could be used to convert energy to range and vice versa. The calibrated mass gates were applied to determine which equation should be used for the conversion on an event by event basis, solving the codependency issue described earlier. The results of each

energy loss calculation were plotted onto a histogram (see Figure 6.12) so that the mean value of the distribution could be found. This mean value of $dE_{Al} = 91.1$ MeV was then used as a final estimate for the energy loss in the foil.

Attempts were made to apply the energy loss correction on an event-by-event basis rather than using a mean energy loss value, however, this was found to worsen the timing resolution of the mass plots.

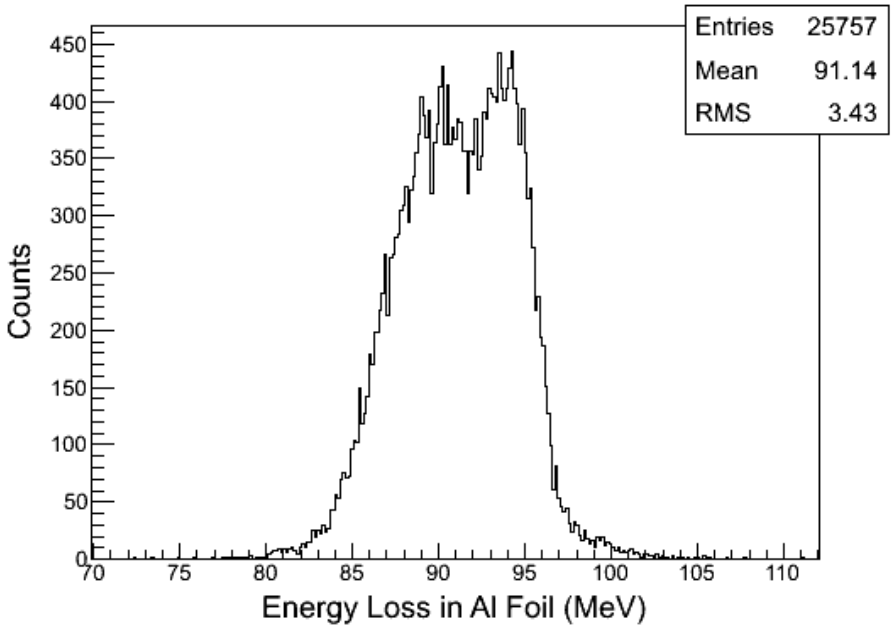

Figure 6.12: Histogram showing the results of each individual calculation of the energy loss through 100 μm thick Al foil. The mean value of this distribution, which is shown in the statistic box as 91.1 MeV, is used as the final estimate of dE_{Al}.

More accurate mass calculations were then made that included dE_{Al} as well as the energy measurements from the wall DSSSD and CsI crystals. These were calibrated once again to create new mass gates that could be used when finding the energy loss through the stop scintillator. Range vs. energy plots were made for Co isotopes passing through a sheet of plastic, and the backward interpolation method was repeated using these plots, assuming a scintillator thickness of 2 mm (see Figure 6.13). Care was taken to ensure that the stoichiometry and the density of the plastic used in the calculations, $H_{10}C_9$ and 1.032 gcm^{-3} respectively [66], matched that of the scintillator material (BC-420). The final estimate for the energy loss through the stop scintillator, dE_{stop}, was then determined from the mean value of these energy loss calculations, and found to be $dE_{stop} = 853.3$ MeV.

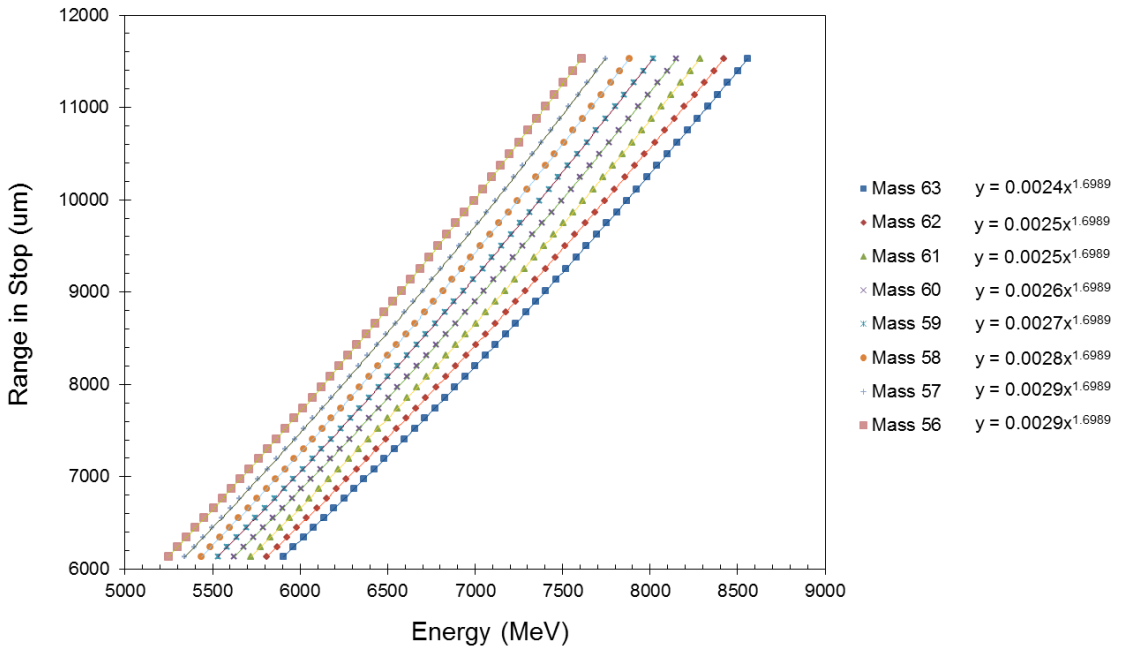

Figure 6.13: Range in stop scintillator vs. energy plots used to find the energy loss through the stop scintillator.

Due to the relatively large thickness of the plastic stop scintillator, the value of dE_{stop} used in the final mass calculations was revised to take account of the trajectory of a particle passing through the scintillator. If a fragment travelled at any angle other than perpendicular to the scintillator, the amount of material that it passed through would be greater than 2 mm. An effective thickness, T_{eff}, was therefore introduced, which is given by the following equation:

$$T_{eff} = \frac{cos(\theta_{after})}{T_{stop}} \tag{6.2}$$

where T_{stop} is the thickness of the scintillator. This was applied to the energy loss through the stop scintillator by multiplying dE_{stop} by the ratio of the effective thickness to the perpendicular thickness. Applying this correction assumes that the energy loss varies linearly with thickness, which is a fair assumption when considering thickness variations of only a few hundreds of μm. A similar correction was also applied to dE_{Al} for completeness, although this was expected to make very little difference to the final outcome of the mass calculations because the thickness variation of the foil that arises from different particle trajectories would be considerably less than that of the stop scintillator.

6.4.3.3 Uncalibrated Mass Plots

Figure 6.14 shows the uncalibrated mass calculations using LYCCA-0 wall energy loss measurements only (top left), LYCCA-0 wall measurements + dE_{Al} (top right), and LYCCA-0 wall measurements + dE_{Al} + dE_{stop} (bottom) plotted onto 1D histograms.

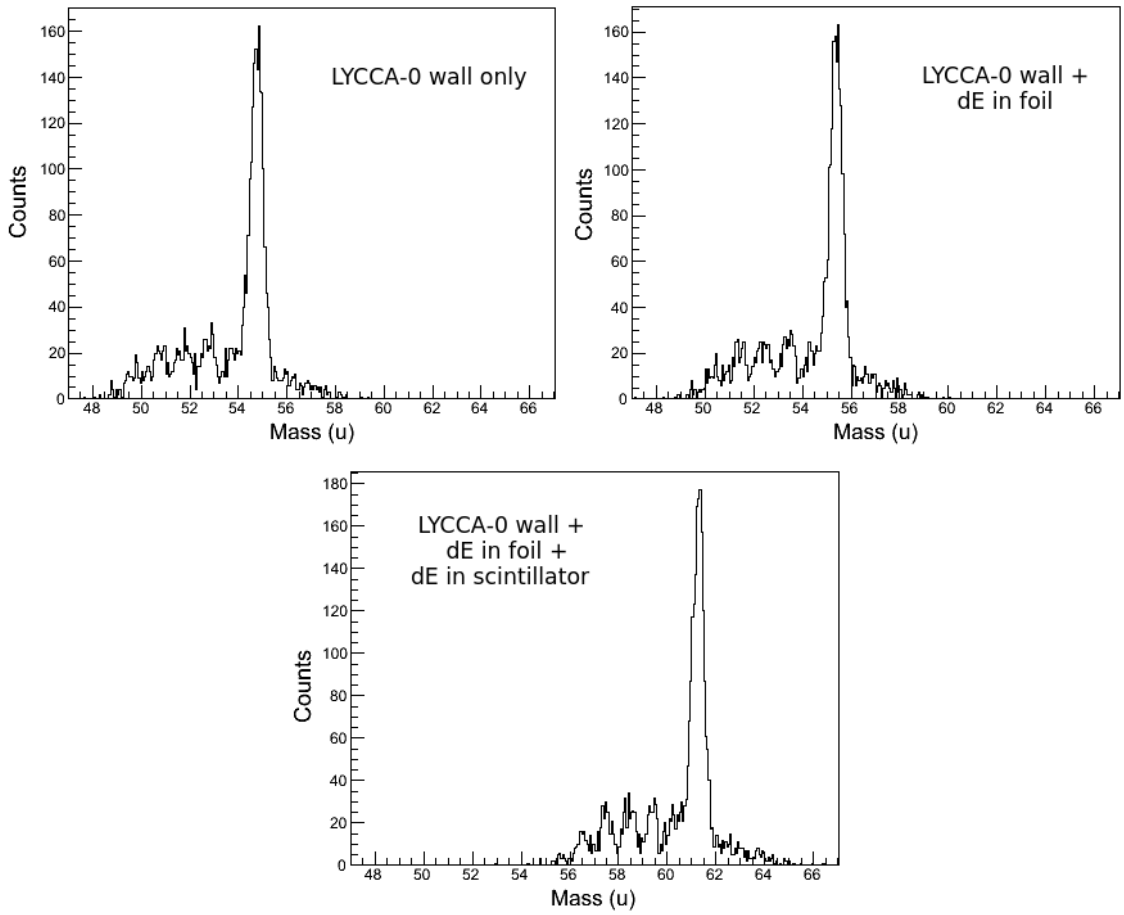

Figure 6.14: Histograms showing uncalibrated mass calculations using LYCCA-0 wall energy loss measurements only (top left), LYCCA-0 wall measurements + dE_{Al} (top right), and LYCCA-0 wall measurements + dE_{Al} + dE_{stop} (bottom). Both the accuracy and resolution of the mass calculations improve as a greater percentage of the total energy of each fragment is accounted for and the energy measurements near their correct values.

From this figure, it is clear to see that including the energy loss through the foil and stop scintillator not only increases the accuracy of the mass calculations, but also improves the mass resolution of the mass calculations, although it is thought that the latter emerges as a consequence of the former. To understand this, one has

to consider what effect an incorrect energy measurement has on the mass calculation.

The non-relativistic relationship between mass, energy and time can be written as $M = kEt^2$, where k is a proportionality constant. If E and t are the exact values of energy and ToF for each fragment, then the calculation will always result in the correct value of M, and any variation in these mass measurements will arise from the energy and timing resolutions. If the energy measurement is incorrect by a value Δ_E, the mass-energy-time relationship becomes:

$$M = k(E - \Delta_E)t^2 \tag{6.3}$$

$$M = kEt^2 - k\Delta_E t^2 \tag{6.4}$$

From the above equation, it is clear to see that an incorrect energy measurement provides an inaccurate result for M, however, we also have to consider how the event-by-event time variation affects the situation. This can be examined by partially differentiating equation 6.4 with respect to t:

$$\partial M = 2kEt\partial t - 2k\Delta_E t\partial t \tag{6.5}$$

The first term of equation 6.5 represents the usual contribution to the mass resolution from the resolution of the ToF. However, the second term appears purely as a consequence of including Δ_E in the non-relativistic mass-energy-time relationship, and any variation in this term on an event by event basis simply adds to the mass resolution. Momentum spread of the beam causes a large variation in t that is usually counteracted by the corresponding energy measurement, however, this cannot be done in the second term of this equation as it does not contain an E measurement, and hence, the ToF fluctuations contribute directly to the mass resolution. As Δ_E tends to zero, and the correct energy measurement is reached, the best mass resolution will be obtained and will only contain contributions from the resolution of the ToF. This explains why the mass resolution is seen to improve as more energy losses are taken into account in Figure 6.14, as more of the total energy of the fragment is accounted for.

6.4.4 Mass Calibration

After including the energy losses in the Al foil and stop scintillator into the mass calculation, the resulting mass values underestimated the fragment masses by around

1.5 u, suggesting that the total energy and the β_{pl} used in the calculation were not completely accurate, and therefore did not correlate perfectly with one another.

The total energy measurement used in the calculation required the β_{pl} value to be that of the beam just before it hits the stop scintillator. However, the calculation used to find β_{pl} determines the average velocity of the beam as it travels between the target and the stop scintillator. In reality, the beam travels a small proportion of this flight path at velocities faster than β_{pl} between the target and the target DSSSD as well as between the target DSSSD and the diamond detector, and the rest of the flight path at a velocity slightly slower than β_{pl}. Although the difference between this average velocity, and the actual velocity of the beam before it hits the stop scintillator will only be small, it may be enough to contribute toward the underestimate seen in the mass calculations.

Another more dominant contribution may have been caused by the variation in the ballistic deficit generated when the signals from the CsI detectors were shaped. Ideally, a pulse from the preamplifier of a CsI crystal should be shaped using a time constant that is much larger than the signal rise time to allow for full charge collection, preserving the signal amplitude. However, using a large time constant is not always practical, and as a result, the height of the shaped pulse is often less than that of the original. The reduction in amplitude between the original and shaped pulse is known as the ballistic deficit and varies with charge collection time [30].

The CsI detectors were calibrated using ^{64}Ni beam whereas the mass measurements presented in this Chapter were created using data from a number of different Co and Fe fragments. The charge collection time in the CsI crystal is dependent upon the type of ion incident on the detector, and hence, the ballistic deficit experienced by the CsI detectors varies depending upon the species of fragment detected. As only a ^{64}Ni beam was used during calibration, the energy measurements taken throughout the experiment wrongly assumed a ballistic deficit equal to that of the ^{64}Ni fragments, leading to incorrect energy measurements for the Co and Fe fragments, and therefore an incorrect mass measurement.

In order to obtain a mass resolution in atomic mass units, u, the mass plots shown in figure 6.14 needed to be calibrated. The same calibration method described below was also used to generate the mass gates used to calculate the energy deposited in the Al foil and the stop scintillator (see Section 6.4.3.2).

Calibration was undertaken by fitting Gaussian fits to the five most prominent peaks found in the uncalibrated Co fragment mass plot. The expected fragment mass was then plotted against the centroids of each of these fits, and a linear fit was made

to the data, the resultant gradient and intercept of which formed the calibration gain and offset. A convincing estimation of the expected fragment mass could be made from the Co mass plot, as the significantly larger peak is known to originate from the unreacted ^{63}Co beam, and therefore corresponds to a mass of $A = 63$. Using this insight, and taking the distance between each peak into consideration, it was concluded that the other peaks, from right to left, corresponded to $A = 61$ to $A = 58$. The $A = 62$ peak appeared to be indistinguishable from the largest peak, and could not be used for calibration purposes.

Applying the same calibration offset and gain to all events and then gating on Z = 27 and Z = 26 events results the calibrated mass plots for Co and Fe fragments respectively, as shown in Figure 6.15. Even though the calibration was made using peaks from the mass plot of the Co fragments, the calibration appears to hold well for the Fe fragments, and each isotope can be identified with confidence. From this mass plot, one can see that the three most abundant Fe isotopes formed through fragmentation reactions in the target detectors were ^{57}Fe, ^{58}Fe and ^{59}Fe. Mass gates could easily be placed on any one of these peaks if further analysis into a particular isotope was required.

Details of the mass resolution of the calibrated mass plots can be found in Section 6.6.1

6.5 Mass Measurements Using Diamond ToF

Before similar mass calculations and plots could be made using the diamond ToF, some precursory analysis had to be undertaken. The raw timing signals from all strips of the diamond detector needed to be combined into one ToF measurement. However, each of these signals possessed a different offset caused by differing cable lengths, and each strip included both intended and induced signals that needed to be separated before the true timing measurement could be found.

6.5.1 Induced Signals

When charge carriers begin to move toward the contact of the strip in which they were generated, not only do they induce charge on the electrode of this strip, but also on the electrodes of neighbouring strips. Any signals from the detector strips caused by charge generation within neighbouring strips are known as induced signals. By plotting the diamond ToF against the plastic ToF, the intended signals can be

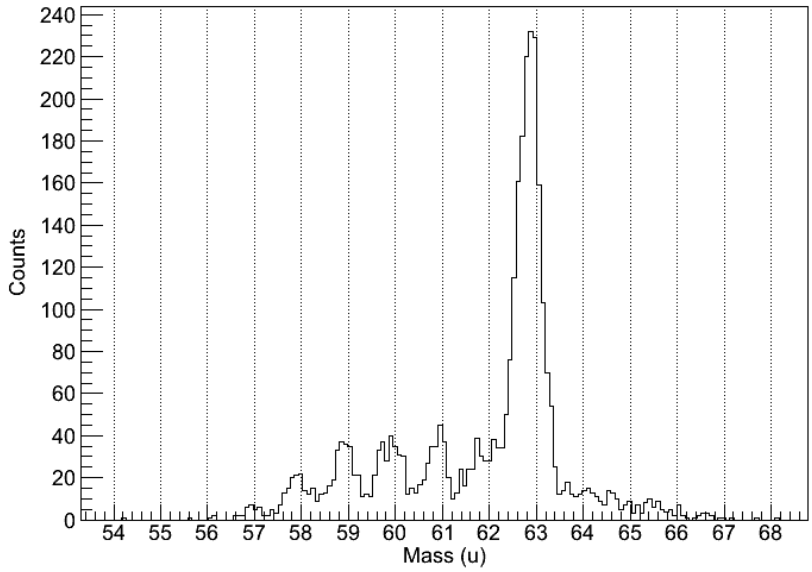

(a) Z = 27

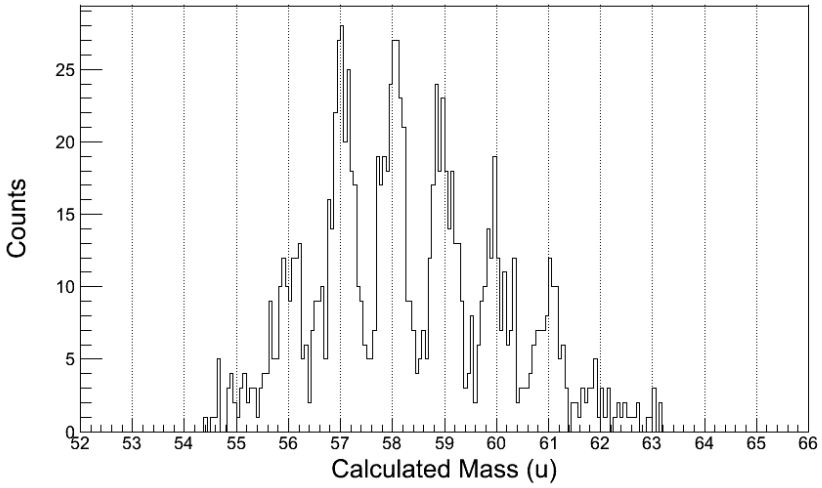

(b) Z = 26

Figure 6.15: Calibrated mass plot showing the different (a) Co fragments and (b) Fe isotopes found in the beam. The calibration offsets and gains were created by comparing the peak positions of the Co fragment mass peaks with the expected peak positions, which could be ascertained from the large peak generated by the unreacted ^{63}Co beam.

visually discriminated from the induced signals, an example of which can be seen in Figure 6.16a.

This figure uses data from strip 4D, which is the topmost strip on wafer 4.

The histogram shows three clear regions of counts, one of which corresponds to the intended timing signal, whilst the other two are formed by induced signals from neighbouring strips. It is possible to determine which region is caused by the intended signals by replotting the histogram in Figure 6.16a using a gate on the target DSSSD map located at the position of strip 4D. As the target DSSSD is positioned only a few mm in front of the diamond detector, applying this gate, which can be seen in Figure 6.16, should restrict the events to those that passed through strip 4D. The resultant plot is shown in Figure 6.16b, and as expected, displays just one region of counts that must correspond to the intended timing signals.

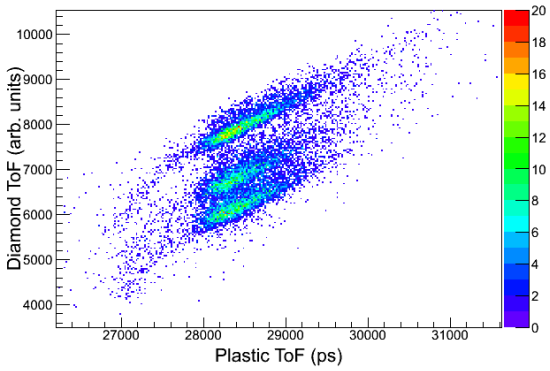

(a) Without any target DSSSD gates

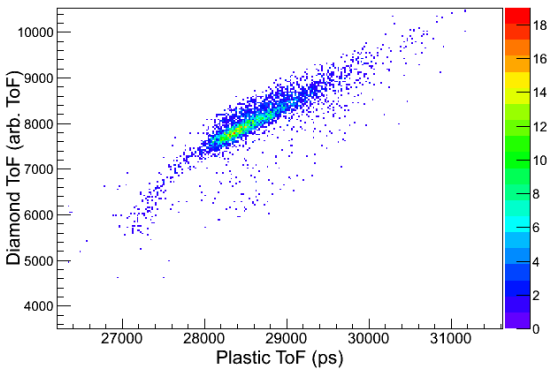

(b) Target DSSSD gate applied

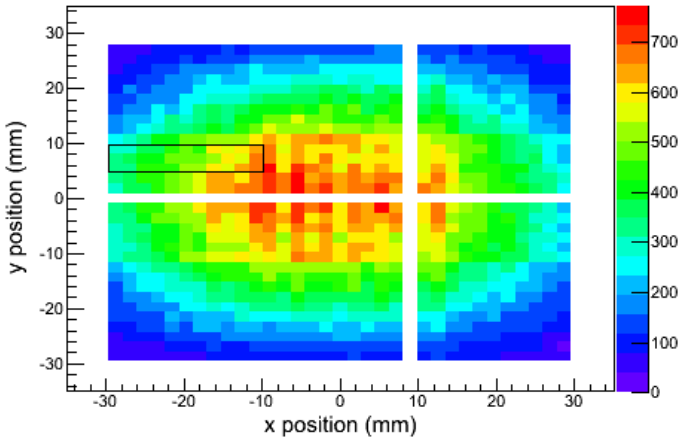

(c) Gate placed at location of strip 4D

Figure 6.16: Diamond ToF vs. Plastic ToF plots showing (a) both intended and induced signals from strip 4D and (b) intended signals only after applying position gate on the target DSSSD map. (c) shows this position gate on the target DSSSD map, placed at the location of strip 4D.

By gating on the positions of strips 4C and 4B in a similar manner, it was

found that the middle region in Figure 6.16a is caused by induced signals from strip 4C, which directly neighbours 4D, and the lower region corresponds to induced signals from strip 4B, which is positioned two strips from 4D. Gating on the location of strip 4A, positioned the furthest from 4D, produces just a few random events in the diamond ToF vs. plastic ToF histogram, which can probably be attributed to noise. After further analysis using data from other diamond strips, it was found that the intended signals always corresponded to the region with the longest diamond ToF measurement, whereas induced signals formed the areas below at shorter ToF values.

The shorter ToF measurements generated by these induced signals is thought to originate from differences in their amplitudes. Any signal induced by the movement of charge carriers through a neighbouring strip is going to have a lower amplitude than a signal produced by charge carriers travelling within the strip itself. Similarly, the signal induced by charge carriers moving through a strip positioned two strips away will have an even lower amplitude. When these low amplitude induced signals reach the leading edge discriminator, they may only just extend above the discriminator threshold, introducing a large amount of signal walk. This produces a later ToF start timing signal output when compared with the output from a large amplitude intended signal, which in turn leads to a shorter diamond ToF measurement. Signal cables for strip 4A had to be disconnected during the commissioning experiment as the feedthrough caused a vacuum leak, and as a result, strip 4A was not biased whilst the ^{63}Co data was being taken. Without bias, charge carriers generated in strip 4A would recombine instead of travelling through the diamond lattice, and consequently, signals from charge carrier movement in strip 4A are not induced on the contacts of 4D, and are not visible in Figure 6.16a.

To ensure that only intended diamond ToF measurements were included in the mass calculations, strip position gates on the target DSSSD map were applied to the data obtained from the each of the corresponding diamond strips. These gates were used throughout the diamond ToF analysis.

6.5.2 Calibration of Strips

Although removing the induced signals from each of the diamond timing measurements helped to clean up the individual strip signals, a calibration offset still needed to be applied to the measurements before combined diamond ToF values could be made. To do this, the diamond ToF was calculated for each strip by taking the av-

erage stop scintillator timing measurement, i.e., the output from the averaging algorithm outlined in Section 6.4.1, away from the raw diamond timing after converting the TDC bins into picoseconds. The average stop scintillator timing measurements included position corrections to account for the distance between the interaction point and each PMT.

The distribution of diamond ToF measurements from each diamond strip were individually plotted onto histograms, and Gaussian fits were used to find the centroid values of each distribution. Offsets were then calculated for each strip using these centroids so that, when applied, each ToF peak became aligned with the distribution from strip 2A. Despite this calibration method producing a reasonable first estimate, some of the ToF distributions were found to be skewed, which increased the inaccuracies associated with the Gaussian fit. This skewness is thought to arise from the fact that the generation of some fragments may be more abundant at certain angles, and hence, one strip may detect a larger number of Fe fragments, for example, than another strip, depending upon its position within the diamond detector.

To overcome this problem and improve the strip calibration, a new technique was devised that used only ^{63}Co fragments to create the calibration offsets. Separate Co mass calculations were made for each strip using the method described in Section 6.5.4. New mass offsets were then created by comparing the positions of the ^{63}Co mass peak for each strip with that of strip 2A. These mass offsets, which varied from strip to strip, were applied on an event by event basis, along with the ToF offsets described above so that a final mass calculation could be made that combined data from all working diamond strips.

An additional ToF offset was applied to the diamond ToF measurements so that the values became representative of the time taken for a fragment to travel between the diamond detector and the stop scintillator. This offset was found using the same technique used for finding the ToF offset for the plastic ToF. The centroid value of the diamond ToF distribution for strip 2A was compared with the ToF expected from the LISE++ simulation, and the difference between these two values was assigned to the ToF offset. The same offset was applied to each strip during the β_{dia} calculation.

Only data from 16 of the 20 strips were used for the diamond ToF analysis. Signals from the other four strips, all of which were positioned on different wafers, as well as the diamond wafer constructed with a full pad contact (1A), were too noisy to be included in the analysis. The noisy signals were most probably caused

by a poor connection between the metal contact and bonding wire, or delamination of the metal contact. Unfortunately, the noisy signal from the full pad contact, 1A, meant that a performance comparison between the low capacitance strip contact and the higher capacitance full pad contact could not be made.

6.5.3 Corrections to the Diamond ToF

6.5.3.1 Trajectory Corrections

A number of corrections were made to the diamond ToF measurements and resultant mass calculations, in order to improve their resolutions. The first of these was a trajectory correction, which was made whilst calculating β_{dia} (equation 4.4). The angle of the fragment's trajectory after the secondary target was found using the tracking capabilities of the target and wall DSSSDs, and was then used, in combination with the distance between the diamond start and the plastic stop detectors, to calculate the length of the fragment's flight path. Using this flight path value instead of the distance between the diamond detector and stop scintillator meant that the velocity of a fragment travelling along a trajectory with a relatively large angle is not underestimated, improving the accuracy of the β_{dia} calculation.

6.5.3.2 Strip Position Corrections

In analogy with the position correction made to the plastic ToF described in Section 4.4.2, a correction was also made to the diamond ToF to take account of the time taken for a signal to travel from the interaction point to the position of the bonding wire. The bonding wire was generally placed 1 - 3 mm from one of the narrow edges of a strip, which meant that the maximum distance a signal had to travel along a strip to reach the bonding wire was 15 - 17 mm. A signal takes approximately 60 ps to travel this distance, which introduces an unwanted variation in the start measurement of the diamond ToF and worsens the timing resolution.

The exact position of the bonding wire varied from strip to strip, making individual position corrections, like those made to the plastic ToF, difficult. Uncertainties in the bond wire position would just add further error into the analysis, as would uncertainties in the exact position of the interaction point caused by the position resolution of the target DSSSD. As a result, target DSSSD gates were used to narrow down the position of the interaction to within one of three areas of the strip, near the bond, middle of the strip and furthest from the bond. These three

regions are shown in Figure 6.17.

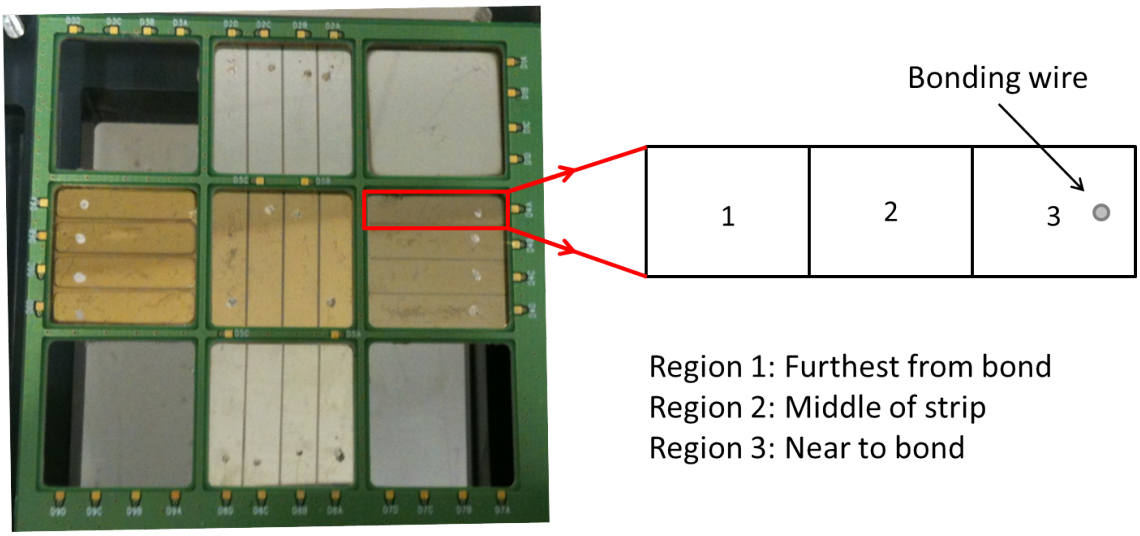

Figure 6.17: Each strip on the diamond detector was divided into the three regions shown in the diagram so that corrections could be made for the time taken for signals to reach the bonding wire.

Mass calculations were made for each event that passed through one of these position gates, and separate mass plots were created for the near bond, middle, and furthest from bond regions of the same strip. An example of these plots from strip 4C can be seen in Figure 6.18. Although the majority of the mass plots created for each region contained few statistics, Gaussian fits could still be made to the ^{63}Co mass peak of all mass plots created. The centroid value, extracted from each of these Gaussian fits, was used to calculate the mass offset required to align the near to bond and furthest from bond regions with the middle of strip region of the same strip. Once the three regions on each strip had been aligned, the strips were recalibrated using the mass plot technique described in Section 6.5.2.

The three mass plots shown in Figure 6.18 for each region on strip 4C demonstrate the shift expected between each region. Mass calculations from the near to bond region are shifted to larger mass values, which is indicative of a greater ToF measurement. This correlates well with the hypothesis that signals generated nearer the bond wire position create an earlier start time than signals generated further from the bond wire, and hence, produce a greater ToF measurement.

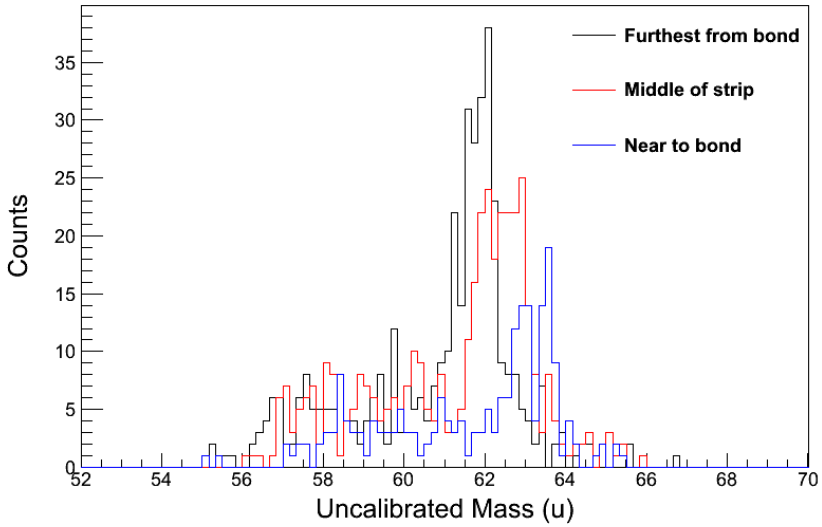

Figure 6.18: Mass plots for events from strip 4C found within the near to bond region (blue), middle of strip region (red) , and furthest from bond region (black) . A slight shift can be seen between each of these mass plots, which can be attributed to a difference in diamond ToF measurements caused by the time taken for signals to reach the bonding wire on the diamond strip. This shift was corrected for by fitting the ^{63}Co mass peak, extracting the centroid value, and then using this to create offsets so that each peak lined up with the peak from the middle of strip region.

6.5.4 Mass Calculations

The diamond ToF mass calculations were made using a similar method to the plastic ToF mass calculations. The only difference between the two methods was the calculation used to find the β value. The diamond ToF was measured between the diamond start detector and stop scintillator, and did not have a significant percentage of its flight path before the secondary target that had to be accounted for, unlike the flight path for the plastic ToF. This made the calculation of β_{dia} more simple.

Each β_{dia} value was calculated on an event by event basis using equation 4.4. The diamond ToF, t_{dia}, in this equation used only the intended signals that had passed through the stop scintillator multiplicity gate, and included a constant ToF calibration offset that was calculated with the help of the LISE++ simulation program. Mass offsets were applied to the outcome of the mass calculation and varied depending upon the strip and region of the event's interaction point. A second offset was then included to correct for cable length differences between signals from each strip, and align the mass calculations from strip 4C with those from strip 2A.

Both the mass calculations made with the diamond ToF, and those made with the plastic ToF used the same total energy measurements as, for both cases, the fragment spent the majority of its flight path travelling between the secondary target and the stop scintillator. Only CsI and DSSSD measurements from the most central LYCCA-0 wall module were taken into account to keep the analysis of both ToF options consistent and ensure that poor calibration between the wall modules did not have adverse affects on the resolution of the mass calculations.

6.5.4.1 Isotope Identification Plots

The diamond ToF was plotted against E_{res} so that a visual comparison could be made between the performance of the diamond ToF and the plastic ToF. The diamond ToF vs. E_{res} histograms for Co and Fe fragments shown in Figure 6.19 (top and bottom respectively) used outgoing Z gates from both the dE vs. E_{res} and dE vs. β_{dia} plots, and only events that received a signal from all LYCCA-0 detectors were considered. The maximum-multiplicity gate on the stop scintillator was also applied, along with the less restrictive gate on incoming ^{63}Co fragments from the FRS to optimise the visual appearance of the histograms. Not all of the correction offsets could be applied to these histograms, as most of them involved correcting the outcome of the mass calculations, rather than the diamond ToF itself. As a result, only events from one strip were used to create the diamond ToF vs. E_{res} plots so that the resolution of the plots was not compromised by poorly calibrated strips. There was, however, no way of including the strip position corrections into these histograms.

When comparing the diamond ToF vs. E_{res} histograms in Figure 6.19 with those from the plastic ToF analysis shown in Figure 6.9, it is instantly clear that isotopes are much more distinguishable in the latter. As the energy measurements used for both of these plots, E_{res}, is exactly the same, this indicates that the difference in quality of the two plots must arise from the resolution of the ToF measurements. Since the plastic ToF evidently has the better timing resolution, and the stop scintillator was used for the plastic ToF measurement and the diamond ToF measurement, it seems reasonable to assume that the main contributor to the resolution of the diamond ToF was the diamond detector.

Although one can get a good idea of the comparative timing resolutions of the plastic scintillators and the diamond detector from the ToF vs. E_{res} plots, calculating a quantitative resolution for each timing detector allows for a more accurate

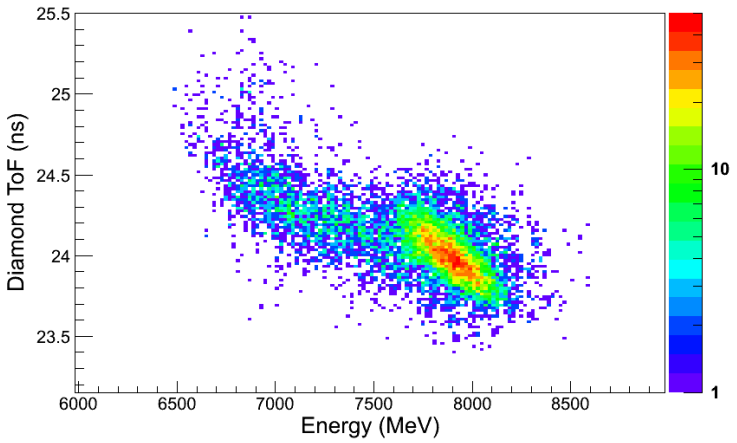

(a) Z = 27

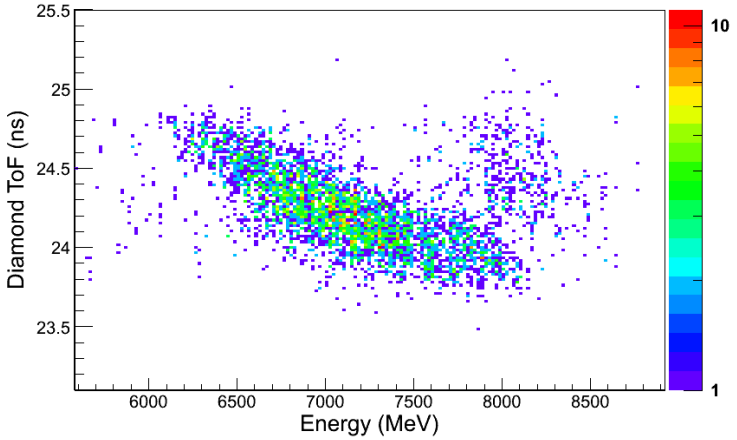

(b) Z = 26

Figure 6.19: Diamond ToF vs. E_{res} plots for (a) Co fragments and (b) Fe fragments. It is not possible to distinguish between neighbouring isotopes in either of these plots.

comparison to be made.

6.6 Mass Resolution

6.6.1 Mass Resolution for Plastic ToF

The calibrated measurements for Fe fragments were used to find the mass resolution of the plastic ToF mass calculations. As Figure 6.20 shows, a fit made up of six Gaussian peaks was applied to the mass plot so that the standard deviation, x_i, and the corresponding error, σ_i, of each mass peak could be extracted. These values can

be found in Table 6.1. A final mass resolution value was then calculated by taking a weighted mean, μ, of the Gaussian widths using the following equation:

$$\mu = \frac{\sum \frac{x_i}{\sigma_i^2}}{\sum \frac{1}{\sigma_i^2}} \tag{6.6}$$

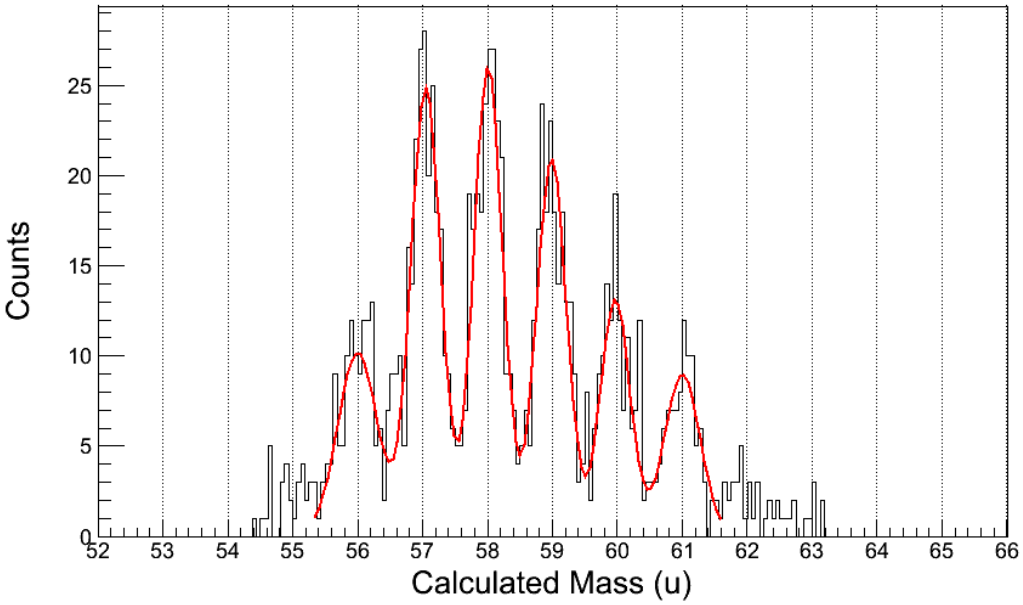

Figure 6.20: Calibrated mass plot showing the different Fe isotopes found in the beam. A fit consisting of six Gaussian peaks applied to the data, and the resulting standard deviations and corresponding errors from each mass peak were extracted to calculate the final mass resolution of the mass calculation with the plastic ToF.

Mass Peak (u)	**Standard Deviation (u)**	**Error (u)**
56	0.276	0.037
57	0.228	0.028
58	0.231	0.018
59	0.221	0.017
60	0.229	0.020
61	0.308	0.038

Table 6.1: Standard deviations and their corresponding errors extracted from the Gaussian fits to the six most prominent peaks found in the mass plot for Fe fragments. The final mass resolution was obtained by taking the weighted mean of these values.

The weighted mean of the standard deviation values was found to be 0.234 ± 0.009 u. Converting this into a FWHM (full width at half maximum) by multiplying by 2.35 gives a final mass resolution of **0.55 ± 0.02 u**. This result indicates that both the timing resolution of the plastic scintillators, as well as the energy resolution of the energy detectors must be better than the sought after resolutions of 100 ps and 1 % required to obtain unambiguous fragment identification. This also provides a proof-of-principle for the fragment identification capabilities of the LYCCA-0 detector system.

6.6.2 Mass Resolution for Diamond ToF

To ensure consistency, the resolution of the diamond ToF mass calculations was also found by fitting Gaussian peaks to the calibrated Fe fragment mass plot. Calibration of the diamond ToF mass calculations proved to be more demanding than calibrating the mass plots created using the plastic ToF because very few of the mass peaks were distinguishable, which increased the difficulty of finding the centroid values of the uncalibrated mass peaks.

Mass peaks for the ^{63}Co, ^{56}Fe and ^{59}Fe fragments were the most discernible from all of the diamond ToF mass plots created, and as a result, the centroids of these three peaks were used for the mass calibration. The ^{56}Fe and ^{59}Fe mass peaks were identified as such by comparing the shape of the diamond Z = 26 mass plot with that of the calibrated plastic ToF Z = 26 mass plot. As each event was measured by both ToF options simultaneously, the distribution of fragments in each mass plot should be the same. This is not an ideal method for calibration, and could not be used if the diamond ToF was the only ToF option present in the final LYCCA detector setup. The calibration offset and gain was found using the same linear fit procedure outlined in Section 6.4.4.

The final calibrated mass plots for Co and Fe fragments can be found in Figure 6.21. The particle gates used when creating these plots were the same as those employed when making the plastic ToF mass calculations to ensure consistency throughout the analysis, the only difference being that the Z selection was made using dE vs. β_{dia} histograms rather than dE vs. β_{pl}. All of the corrections to the diamond ToF and mass calculations mentioned above were applied in order to get the best possible mass resolution from the calculations. It should be noted here that the strip position correction seemed to make very little difference to the appearance of the resultant mass plots because the resolution of the diamond detector was

clearly worse than the 60 ps variation that the strip position offsets corrected for. Nevertheless, a description of the correction procedure was still included in this thesis as it may become important when working on any future development of the diamond detector.

Once the diamond ToF mass plots had been calibrated, an attempt was made to fit six Gaussian peaks to the plot. It was found that a convincing fit could only be made by first fitting the mass peaks found at 56 u and 59 u, and then restricting the centroid positions of the other peaks to the expected masses of 57 u, 58 u, 60 u and 61 u. The individual fits made to the ^{56}Fe and ^{59}Fe mass peaks are shown in black in Figure 6.22, along with the overall fit that is shown in red. The final mass resolution for the diamond ToF mass calculations was determined by calculating the weighted mean of the standard deviation from the Gaussian fits made to the ^{56}Fe and ^{59}Fe mass peaks. Details of these measurements are listed in Table 6.2.

Mass Peak (u)	**Standard Deviation (u)**	**Error (u)**
56	0.502	0.093
59	0.597	0.106

Table 6.2: Standard deviations and their corresponding errors extracted from the Gaussian fits made to the two most distinguishable peaks found in the diamond ToF mass plot for Fe fragments. The final mass resolution was obtained by taking the weighted mean of these values.

The outcome of the weighted mean value was found to be 0.54 ± 0.07 u, which corresponds to a FWHM mass resolution for the diamond ToF mass calculations of **1.27± 0.16 u**. Not only is this resolution significantly worse than the resolution obtained from the plastic ToF mass calculations, but it is also larger than 1 u, which defines the limit at which neighbouring fragment peaks become indistinguishable from one another. This result agrees with the observations from both the Co and Fe mass plots, as well as the E_{res} vs. diamond ToF histograms, and strongly suggests that the timing resolution of the diamond start detector must be worse than the desired timing resolution of 100 ps.

6.7 Extracting the Timing Resolution

The timing resolution for the plastic scintillators and the diamond start detector were extracted from the resolution of the mass calculation using the partial differential equations given in Section 4.5. In order to calculate $\partial A(\beta)$, the contribution to

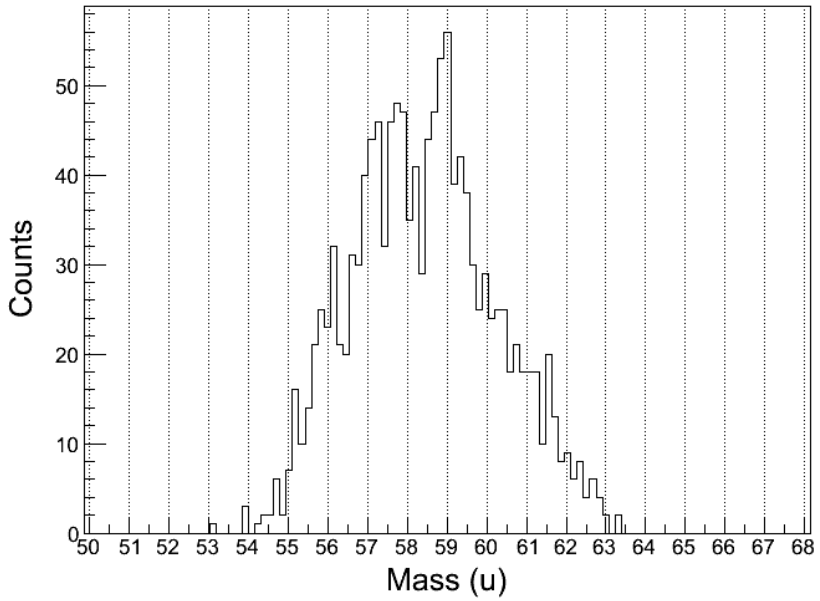

(a) Z = 27

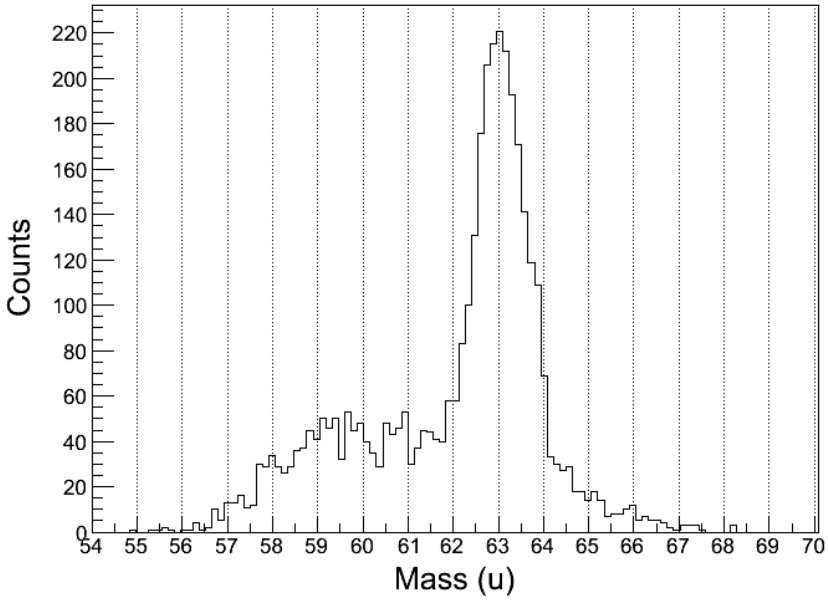

(b) Z = 26

Figure 6.21: Calibrated mass plots showing the different (a) Co fragments and (b) Fe isotopes found in the beam calculated using the diamond ToF. Only the three most distinguishable mass peaks (^{63}Co, ^{56}Fe and ^{59}Fe) could be used to find the calibration offset and gain.

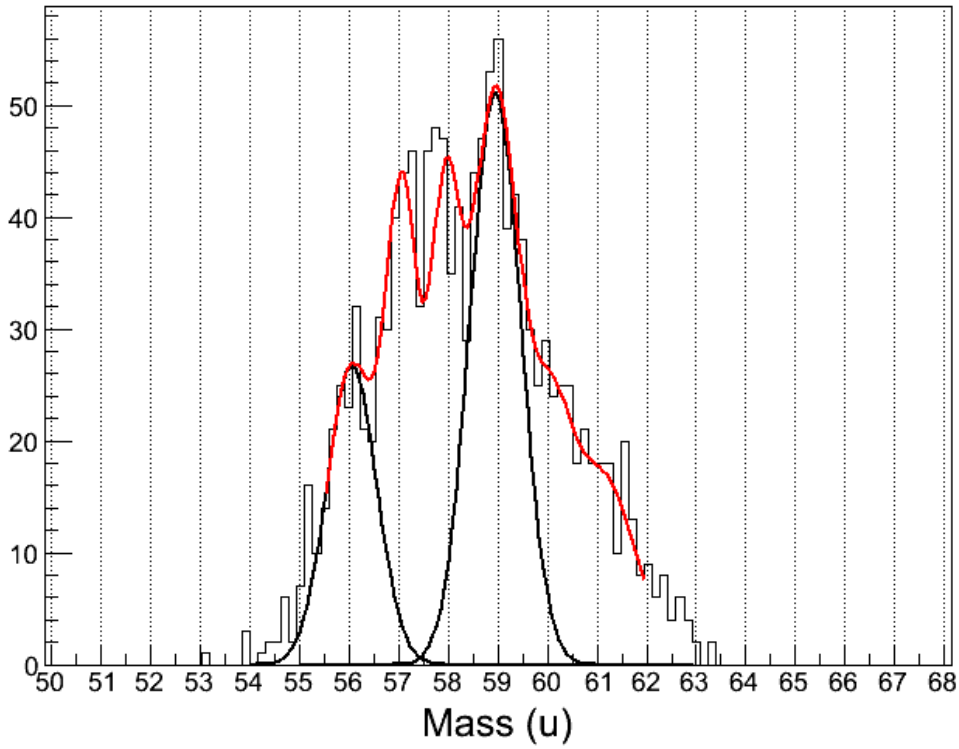

Figure 6.22: Calibrated mass plot for the Fe fragments that shows the Gaussian fits applied to the ^{56}Fe and ^{59}Fe mass peaks (black) and the overall fit made to six of the mass peaks (red).

the mass resolution from the resolution of the β measurement, the contribution from the energy resolution must first be acquired. This involves measuring the energy resolution of the CsI and wall DSSSD detectors.

6.7.1 Measuring Energy Resolution

Data from the calibration run with the least amount of matter in the beam line were used to measure the energy resolution of the CsI detectors and the wall DSSSDs in order to get as little energy spread in the ^{64}Ni secondary beam as possible. A 0-0-0 setting (thickness of production target-F2 degrader-F4 degrader) would have been ideal for this purpose, however data files for this setting appeared to be corrupted, so the next best setting of 0-4-0 was used instead.

Incoming ^{64}Ni and outgoing Z = 28 gates were placed upon the data, as well as the necessity for all LYCCA detectors to record an event, and that any event recorded by the plastic scintillators required the maximum multiplicity on both de-

tectors. This reduced spurious events in the energy detectors and got rid of any fragments other than Ni, which helped to lessen the spread of the energy measurements. E_{res} vs plastic ToF plots were then viewed to see whether a large number Ni fragments other than the secondary beam were being produced. The vast majority of fragments were found to be ^{64}Ni.

CsI energy from all 9 crystals of the most central LYCCA-0 wall module was added to the energy loss data from the wall DSSSD of the same module, and then plotted onto a histogram so that a measurement of the energy resolution could be made. A Gaussian fit was made to the energy distribution and the energy resolution was determined from the FWHM of this fit. One should assume that the peak seen in this distribution represents a single species of fragments with the minimum possible energy spread available from this data set. The energy distribution and Gaussian fit is shown in Figure 6.23. The energy resolution was then converted into a percentage by dividing the FWHM by the centroid of the energy peak, and then multiplying by 100. This percentage energy resolution was found to be **0.69 ± 0.02** %.

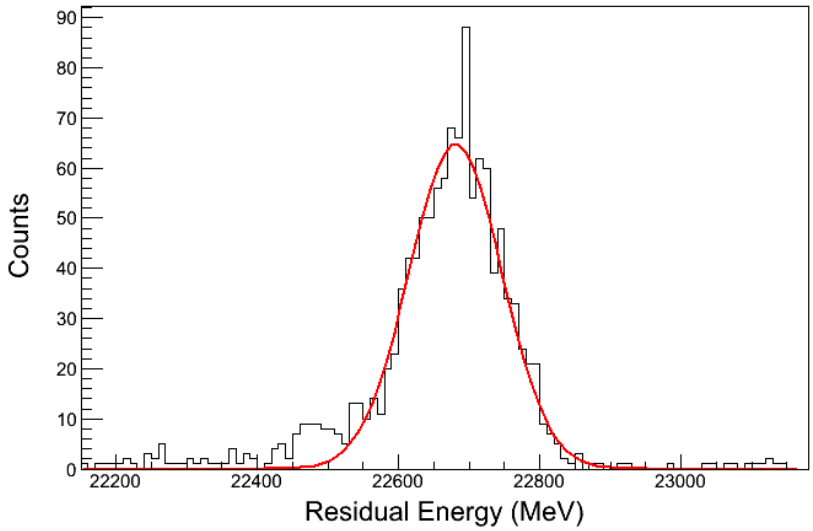

Figure 6.23: The energy distribution and Gaussian fit used to find the energy resolution of the combined CsI and wall DSSSD energy measurement. The resolution was found to be 0.69 ± 0.02 %.

In reality, this energy resolution measurement probably includes a small contribution from the energy and momentum spread of the beam, even though an attempt has been made to minimise this, and therefore, 0.69 % should be thought of as an upper limit to the energy resolution of the combined CsI and wall DSSSD energy measurements.

6.7.2 Calculating Timing Resolution

Once the energy resolution was known, the individual contributions to the overall mass resolution from the energy and β measurements ($\partial A(E)$ and $\partial A(\beta)$) were calculated using equations 4.6 and 4.8 respectively. Equation 4.7 was then used to find the resolution of the β measurements, which could then be converted into a timing resolution using equation 4.9. See Section 4.5 for more details.

Values of E = 8000 MeV and $\beta = 0.5$ were used in these equations, as these were found to be the approximate average measurements used in the mass calculations. A value of A = 58 was also used when finding the timing resolution of both the plastic ToF and the diamond ToF, because this mass was found to be roughly at the centre of the Fe fragment mass plots used in the mass resolution measurements.

The timing resolution of the plastic scintillators had to be determined before the timing resolution of the diamond detector could be found. A ToF of $t_{pl} = 28.5$ ns was assumed for the calculation of the plastic scintillator timing resolution, which was found by measuring the position of the peak in the plastic ToF distribution. The length of the flight path was given by the distance between the start and stop scintillator, which was found to be $d_{pl} = 4.31$ m.

A value of $\partial t_{pl} = 71.8 \pm 3.5$ ps (FWHM) was obtained for the plastic ToF. If one makes that reasonable assumption that both start and stop scintillator behave in a similar way and contribute equally to the resolution of the plastic ToF, the resolution of each scintillator can be found by dividing ∂t_{pl} by $\sqrt{2}$. This gives a timing resolution for each scintillator of **50.8 ± 2.4 ps** (FWHM).

The resolution of the diamond ToF mass calculations was then used to find the timing resolution of the diamond ToF. The same average values of E, β and A were inserted into the partial differential equations given in Section 4.5 so that a direct comparison could be made between the resolution of the diamond ToF and the plastic ToF. The diamond ToF and flight path length were assumed to be $t_{dia} = 24.22$ ns and $d_{dia} = 3.58$ m respectively. These differed from the values used to calculate the resolution of the plastic ToF because the diamond detector was placed downstream of the start scintillator.

The timing resolution for the diamond ToF was found to be $\partial t_{dia} = 199.6 \pm 26.5$ ps. The resolution of the diamond detector alone can be calculated from this value by subtracting the timing resolution of the stop scintillator in quadrature. This gives a resolution for the diamond detector of **193.0 ± 25.6 ps**.

A summary of the values used to calculate the timing resolutions for both

diamond and plastic ToF options is given in Table 6.3.

Property	**Value for plastic ToF**	**Value for diamond ToF**
∂A	0.52 u	1.19 u
∂E	0.69 %	0.69 %
A	58 u	58 u
E	8000 MeV	8000 MeV
β	0.50	0.50
t	28.50 ns	24.2 ns
d	4.31 m	3.58 m
$\boldsymbol{\partial t}$	**71.8 ps**	**199.6 ps**

Table 6.3: Summary of the values used to calculate the timing resolutions of the plastic ToF and the diamond ToF.

The timing resolution result for the diamond detector was nearly double that of the result from the optimisation experiment at Texas A & M University. This was a surprising outcome, as there was very little difference in the electronic setup and the fabrication of the diamond detector between the two experiments. Possible reasons behind this discouraging result are given in the subsequent chapter, along with the implications of the analysis displayed in this chapter.

CHAPTER 7

Interpretation of Results

A diamond timing resolution of 193 ps (FWHM) was extracted from the data taken at the first LYCCA-0 commissioning experiment at GSI. When comparing this result with the timing resolution of 104 ps achieved by an earlier diamond detector prototype at Texas A & M University, it becomes clear that one or more components of the detector setup at GSI must have caused the degradation that is seen in the timing resolution.

This Chapter discusses the main differences between the experimental setup at TAMU and GSI, how these differences could contribute to the discrepancy seen between the timing resolution results, and how the diamond detector may have performed without these contributions.

7.1 Explanations for Poor Resolution

Possibly the most obvious difference between the two setups is the energy and species of the secondary beams used in each experiment. The 33.5 MeV/u ^{40}Ar deposited an average energy of 670 MeV in the front and back diamond detector, whereas the ^{63}Co beam at GSI deposited 380 MeV of energy in the diamond start detector, around half the energy of the TAMU experiment. As a result, the amount of charge collected by the diamond detectors at the two experiments was significantly different.

If one considers Equation 2.8, which is repeated below for convenience, it can be seen that the time variation associated with the noise on the detector signal is inversely proportional to the amount of charge collected by the diamond detector. It therefore seems reasonable to suggest that the difference in charge collection may have contributed toward the disparity in timing resolutions.

$$\sigma_t = \frac{\sqrt{kT \cdot (C_D + C_p)}}{2.28 \cdot Q_{col} \cdot BW_A}$$

Continuing in this vein, the only other component of Equation 2.8 that changed between the TAMU and LYCCA-0 commissioning experiments is C_p. As identical diamond wafers, contact segmentation and preamplifiers were used at both experiments, C_D and BW_A must remain unchanged. There is a possibility that the temperature at which the diamond detector operated may have been different, however, as there was no measurement of this value at either experiment, and any deviation would probably be quite small, one must assume that this component also remained unchanged.

Although not considered at the time, the length of cable present between the diamond detector and the preamplifiers contributes a large amount of parasitic capacitance to the detector system. The length of cable used for each signal during the TAMU experiment amounted to a total of 1 m, whereas 2.5 m of cable had to be used during the commissioning experiment, as the presence of the surrounding RISING gamma array meant that the preamplifiers had to be placed a large distance away from the beam line, above the gamma detectors.

The high frequency RG-316 coaxial cable used in both experiments added a capacitance of 95 pF/m [67] to the full detector system, which generated parasitic capacitances of 95 pF and 237.5 pF for the TAMU and commissioning experiments respectively.

7.2 Extrapolation

7.2.1 Commissioning Result in TAMU Conditions

To observe how the reduction in charge collection and the additional 137.5 pF of capacitance affected the commissioning experiment result, the timing resolution obtained at GSI was extrapolated using equation 2.8 so that the charge collection and parasitic capacitance conditions from TAMU could be imposed upon the GSI result.

A comparison could then be made between the original TAMU timing resolution and the newly calculated GSI timing resolution under TAMU experimental conditions. A value for Q_{coll} for the TAMU experiment was found as a fraction of the charge collection at GSI, Q_{GSI}, by taking the ratio of the average energy deposition in the diamond detector at both experiments, therefore assuming a linear relationship between energy loss and charge collection. The resulting extrapolation estimated that the diamond start detector used at GSI would have produced a timing resolution of 72 ps (FWHM) under the experimental conditions of TAMU.

Comparing the newly extrapolated GSI timing resolution with the original TAMU timing resolution of 104 ps suggests that the more recent diamond detector prototype may have performed better than its predecessor. This seems reasonable, as improvements had been made to both the PCB and the contact and bonding wire fabrication to ensure that the diamond detector was more stable, which should have improved the regularity of the signals from the diamond detector. It should be noted however that the extrapolation using equation 2.8 only considers the timing jitter on the signal, and does not take account of any signal walk that will have also contributed to the timing resolution of the diamond detectors.

7.2.2 Commissioning Result with Zero Cable Length

Using the extrapolation method described above, it is also possible to model the behaviour of the detectors without the presence of parasitic capacitance. From this, an indication of the timing resolution that may be obtainable by placing the preamplifiers directly onto the PCB of detector can be deduced.

The timing resolution expected with zero cable length between detector and preamplifier under the experimental conditions of TAMU was estimated by replacing $C_p = 95$ pF with $C_p = 0$ pF and using a charge collection value of $Q_{coll} = 1.76 Q_{GSI}$. A timing resolution of 26 ps was obtained, an improvement of 78 ps from the original timing resolution result achieved at TAMU, which emphasises the importance of minimising the parasitic capacitances associated with the diamond detector.

Assuming a parasitic capacitance of $C_p = 0$ pF and a charge collection of $Q_{coll} = Q_{GSI}$, a timing resolution of 46 ps (FHWM) was obtained for a diamond detector with neighbouring preamplifiers under the experimental conditions of the LYCCA-0 commissioning experiment. Comparing this with the timing resolution of 50.8 ps achieved by each plastic scintillator during the commissioning experiment shows that, if the setup of the diamond detectors could be altered to incorporate

the preamplifiers onto the PCB of the detector, they could produce similar, if not better, mass identification than the plastic scintillators.

Unfortunately, placing all of the electrical components needed to create a wide bandwidth preamplifier that is ideal for processing the fast diamond timing signal requires a large amount of space, especially for a large area diamond detector that has to be segmented a number of times. The size of the target chamber inside which the LYCCA-0 start detector is placed is limited by the surrounding gamma array, be it the RISING array that was used in the commissioning experiment, or the AGATA array that will be used in future LYCCA experiments. As a result, it is not possible to place the required preamplifier electronics onto the detector PCB and still fit the detector inside the target chamber, which means that the sub 50 ps timing resolution is unattainable for the diamond detectors using the current, necessary arrangement of the LYCCA detectors.

7.3 Final Outcome

The analysis presented on Chapter 6 shows that the ToF measurements from the fast plastic scintillators can be used to distinguish between neighbouring isotopes in the A$\sim$60 region, unlike the timing measurements from the diamond detector. With this in mind, it is clear that the plastic scintillators are currently the best timing option for future LYCCA-0 experiments, and probably any future LYCCA experiments.

As a result of the above conclusion, work began on the development of a new, smaller plastic start scintillator that was able to fit behind the secondary target, within the target chamber. Placing the start scintillator much closer to the target improves the accuracy of the β measurement, as an assumption about the velocity of the beam between the start scintillator and the target no longer has to be made. This should also improve the accuracy of the Doppler correction that is made to the gamma measurements, and should produce cleaner gamma spectra.

The plastic sheet of the new start scintillator measures 77 mm in diameter, and is able to fit 12 PMTs around its circumference. Inevitably, reducing the size of the scintillator reduces the number of measurements that can be made simultaneously by the detector, which will be detrimental to the timing resolution. However, downsizing the scintillator also allows a different type of scintillating plastic sheet to be used (quenched BC-422Q), which is known to perform better than the BC-420 plastic sheet used in the original start scintillator. Simulations made by Hoischen

[12, 65] have shown that the combination of quenched plastic sheet surrounded by 12 PMTs is able to achieve timing resolutions similar to those measured for the larger start scintillator with 32 PMTs.

The implementation of a smaller start scintillator should, therefore, only enhance the performance of the LYCCA-0 array as a whole by aiding the identification of beam fragments in a similar manner as the larger start scintillator prototype, whilst also improving the precision to which the beam velocity after the secondary target can be measured.

CHAPTER 8

Conclusion

The work presented in this thesis set out to determine which of the two timing options proposed was best for future experiments with LYCCA, as well as undertaking an in-depth analysis of the performance of LYCCA-0 during the first commissioning experiment. Data from this experiment were used to measure mass and energy resolutions, from which values for the timing resolution of the fast plastic scintillators and the diamond start detector could be directly compared. This analysis, along with the analysis of the optimisation experiments, also sought to investigate whether it was feasible to build large-area diamond detectors and maintain a good timing resolution, and how one should go about developing such a detector. The analysis of data from the optimisation experiments demonstrated that the timing resolution of the diamond detector was dependent upon both the design of the detector itself, as well as the electronics used to process the signals from the detector.

The optimisation experiment undertaken at TAMU aimed to test the significance of energy deposition and applied bias on the timing resolution of the detector, as well as investigating whether LEDs or CFDs worked best with the diamond detectors. An attempt was also made to discover whether using an ohmic Au contact was an advantage over using a Schottky Al contact, however, poor quality signals from one of the diamond wafers with an Al contact meant that this comparison could not be made.

Results from the discriminator testing demonstrated that timing resolution

measurements acquired using LEDs were consistently better than those that used CFDs, and as a result, leading edge was the discrimination method chosen for all other experiments with the diamond detectors.

Both the energy deposition in the detector and the bias applied across the detector strip were found to have an effect on the timing resolution measurement. The general trend of the timing resolution measurements taken at different bias settings demonstrated that increasing the bias improved the timing resolution of the diamond detectors, indicating that saturation velocity had not been reached at the maximum bias of 600 V. Comparing the timing resolution measurements taken with the ^{40}Ar and ^{20}Ne beams showed that increasing the amount of energy deposited in the diamond wafers also had the same effect, with better resolution measurements being achieved using the ^{40}Ar beam that had the largest energy loss in each detector.

An encouraging timing resolution of 104 ps (FWHM) was achieved during the TAMU optimisation experiment, and problems encountered during the experiment such as preamplifier breakdown and poor signals from one of the diamond wafers suggested that a sub-100-ps resolution could be obtained by making improvements to the fabrication quality of the detector.

The optimisation experiment which took place at the Nuffield Cyclotron at the University of Birmingham sought to investigate how the waveform characteristics of the signal from the diamond detector, such as the rise time and the pulse height, were affected by the capacitance of the detector, and what influence these had on its timing resolution. The performance and characteristics of signals from diamond detectors with Au contacts were also compared with those diamond detectors fabricated with DLC contacts.

Analysis from this optimisation experiment revealed that, whilst there was little correlation between the applied bias and the rise time of the signals, increasing the capacitance of the detector caused the rise time to increase. It was also found that the rise time of the signals was independent of signal's pulse height. These results demonstrated that the rise time of a signal is only affected by the capacitance of the detector, and the amount of charge induced on the detector contacts, which determines the pulse height of the signal and is influenced by the applied bias, has no impact on a signal's rise time.

Investigations into the signal jitter at the Birmingham optimisation experiment found that the amount of jitter measured on the signal decreased with decreasing capacitance and increasing pulse height. This result was explained in terms of

the gradient of the rising edge of the detector signal, with an increase in gradient leading to a reduction of the time variation on the signal. Both reducing the rise time by decreasing the capacitance of the detector, and increasing the pulse height of the signal cause the gradient to increase, and hence, the signal jitter is found to be lower. The timing resolution measurements acquired at Birmingham also support this reasoning, as the timing resolution of the detectors was found to improve with decreasing capacitance. These resolution measurements also demonstrated that DLC contacts consistently produced a better timing resolution than Au contacts, which is thought to be due to larger currents induced on the DLC contact.

The results from the optimisation experiments described above conclude that, in order produce a diamond detector with the best possible timing resolution, the detector must have DLC contacts, and these contacts must be highly segmented to reduce the reduce the capacitance and generate a signal with a fast rise time and minimal timing jitter. However, creating highly segmented detectors introduces difficulties in signal extraction as large number of cables and electronics channels will be required, which may not be feasible at the current LYCCA setup at GSI, nor at the future FAIR setup. A compromise between the timing resolution of any future large-area diamond detector and the feasibility of detector segmentation is therefore necessary.

Analysis of the LYCCA-0 commissioning experiment demonstrated that, not only could LYCCA-0 differentiate between species of fragments with a Z resolution of $\Delta Z = 0.57 \pm 0.01$ (FWHM), but fragments within the same species were also clearly distinguishable using the plastic ToF measurements with a mass resolution of $\Delta A = 0.55 \pm 0.03$ u (FWHM). Taking the energy resolution into account, measured to be 0.69 ± 0.02 % (FWHM), a timing resolution of $\partial t_{pl} = 50.8 \pm 3.1$ ps (FWHM) was achieved for each scintillator. This result confirms that LYCCA-0 can uniquely identify fragments on an event-by-event basis, and is working to the specifications required of it, at least for masses around A=60.

Similar mass measurements taken with the diamond ToF were able to obtain a mass resolution of $\Delta A = 1.27 \pm 0.16$ u. Again, taking the energy resolution into account, as well as the timing resolution of the stop scintillator, a timing resolution of $\partial t_{dia} = 193$ ps (FWHM) was extracted for the diamond start detector. This resolution was worse than expected, and the discrepancy between this result and the timing resolution achieved during the TAMU optimisation experiment has been attributed to the additional parasitic capacitances generated by long cables between the detector and the preamplifiers, as well as the lower energy deposition in the

detector during the commissioning experiment.

The commissioning experiment results summarised above conclude that whilst it is currently unfeasible to produce large-area diamond detectors with the desired 50 ps timing resolution, fast plastic scintillators are able to achieve such a resolution and are therefore the best option for the final LYCCA array. As a result of this, work has begun on the development and fabrication of a smaller plastic scintillator that will be placed within the LYCCA target chamber. Positioning the scintillator close to the secondary target should improve the accuracy of the β_{pl} measurement however, reducing the size of the scintillator, and hence the number of PMTs that surround it, may worsen the timing resolution of the scintillator. It may be necessary to undertake in-depth analysis similar to that presented in this thesis to to be sure that similar fragment discrimination can be achieved using the new design.

The work in this thesis conclusively shows that fragments can be isotopically differentiated, however, the analysis is limited to fragments around A=60. The mass resolution of LYCCA will worsen as the mass of the fragments increase, and further investigation is required to determine the point at which LYCCA is unable to distinguish between fragments of similar mass.

References

[1] P Golubev *et al.* *Nuclear Instruments and Methods A*, 723:55–66, 2013.

[2] D Bazin *et al.* *Nuclear Instruments and Methods B*, 204:629–633, 2003.

[3] *HISPEC/DESPEC Executive Summary.* http://personal.ph.surrey.ac.uk/~phs1zp/Documents.html.

[4] H J Wollersheim *et al.* *Nuclear Instruments and Methods A*, 537:637–657, 2005.

[5] Z Podolyak *et al.* Technical Proposal for the Design, Construction, Commissioning and Operation of the HISPEC/DESPEC experiment at the Low-Energy Branch of the Super-FRS facility. Technical report.

[6] Z Podolyak. *Acta Physica Polonica B*, 41:493–503, 2010.

[7] H Geissel *et al.* *Nuclear Instruments and Methods B*, 204:71–85, 2003.

[8] S Akkoyun *et al.* *Nuclear Instruments and Methods A*, 668:26–58, 2012.

[9] D Rudolph *et al.* LYCCA - the Lund-York-Cologne CAlorimeter: Identification of reaction products in HISPEC-DESPEC@NuSTAR. Technical report, Technical Report, V1.2, June 2008.

[10] Z Podolyak. *Nuclear Instruments and Methods B*, 266:4589–4594, 2008.

[11] R Lozeva *et al.* *Nuclear Instruments and Methods A*, 562:298–305, 2006.

[12] R Hoischen. *Isotope-Selective Spectroscopy: Fast Timing R & D and fp-shell Mirror Isomers.* PhD thesis, Lund University, 2011.

[13] M J Taylor *et al.* *Nuclear Instruments and Methods A*, 606:589–597, 2009.

[14] L Fernandez-Hernando *et al. Nuclear Instruments and Methods A*, 552:183–188, 2005.

[15] C M Buttar *et al. Nuclear Instruments and Methods A*, 392:281–284, 1997.

[16] E Berdermann *et al. Nuclear Physics B*, 78:533–539, 1999.

[17] E Berdermann *et al. Diamond and Related Materials*, 10:1770–1777, 2001.

[18] E Berdermann *et al. Diamond and Related Materials*, 19:358–367, 2010.

[19] M Ciobanu *et al. IEEE Transactions on Nuclear Science*, 58:2073–2083, 2011.

[20] A Stolz *et al. Diamond and Related Materials*, 15:807–810, 2006.

[21] P A Tipler. *Physics for Engineers and Scientists: 4th Edition.* W H Freeman and Company/Worth Publishers, 1999.

[22] www.e6cvd.com/cvd.

[23] C Kittel. *Introduction to Solid State: 8th Edition.* John Wiley and Sons Inc, 2005.

[24] S M Sze. *Physics of Semiconductor Devices: 2nd Edition.* John Wiley and Sons Inc, 1981.

[25] D A Fraser. *The Physics of Semiconductor Devices.* Oxford University Press, 1977.

[26] A K Singh. *Electronic Devices and Integrated Circuits.* Prentice-Hall of India Private Limited, 2008.

[27] J Isberg *et al. Science*, 297:1670–1672, 2002.

[28] J Hammersberg *et al. Diamond and Realated Materials*, 10:574–579, 2001.

[29] K S Krane. *Introductory Nuclear Physics.* John Wiley and Sons Inc, 1988.

[30] G F Knoll. *Radiation Detection and Measurement: 4th Edition.* John Wiley and Sons Inc, 2010.

[31] A Lohstroh *et al. Journal of Applied Physics*, 101:063711, 2007.

[32] P W May. *Philosophical Transactions of the Royal Society A*, 358:473–495, 2000.

[33] J C Madaleno J J Gracio, Q H Fan. *Journal of Physics D: Applied Physics*, 43:374017, 2010.

[34] F Schirru *et al.* *Journal of Instrumentation*, 7:P05005, 2012.

[35] A Denisenko *et al.* *Diamond and Related Materials*, 9:1138–1142, 2000.

[36] H Okushi D Takeuchi, S Yamanaka. *Diamond and Related Materials*, 11:355–358, 2002.

[37] J A Spies *et al.* *Solar Energy Materials and Solar Cells*, 93:1296–1308, 2009.

[38] M M El-Gomati G H Jayakody, T R C Wells. *Journal of Electron Spectroscopy and Related Phenomena*, 143:233–239, 2005.

[39] A Galbriati. Contacts on diamond. *US Patent 8119253*, 2012.

[40] M Pomorski *et al.* *Physica Status Solidi A*, 203(12):3152–3160, 2006.

[41] H Pernegger *et al.* *Journal of Applied Physics*, 97:073704, 2005.

[42] Wang L *et al.* *Chinese Physics B*, 17(10):3644–3648, 2008.

[43] P Moritz *et al.* *Diamond and Related Materials*, 10:1765–1769, 2001.

[44] Ortec. *Preamplifier Introduction.* www.ortec-online.com/download/Preamplifier-Introduction.pdf.

[45] W R Leo. *Techniques for Nuclear and Particle Physics Experiments: A How-To Approach.* Springer-Verlag, 1994.

[46] K Shigaki *et al.* *Nuclear Instruments and Methods A*, 438:282–301, 1999.

[47] R E Tribble *et al.* *Nuclear Physics A*, 701:278c–281c, 2002.

[48] R H Burch R E Tribble and C A Cagliardi. *Nuclear Instruments and Methods A*, 285:441–446, 1989.

[49] C M Folden III *et al.* *Nuclear Instruments and Methods A*, 678:1–7, 2012.

[50] http://www-linux.gsi.de/~weick/atima.

[51] http://www.caen.it/csite/CaenProd.jsp?idmod=789&parent=11.

[52] Ortec. *Fast-Timing Discriminator Introduction*. http://www.ortec-online.com/download/Fast-Timing-Discriminator-Introduction.pdf.

[53] R C Weast. *Handbook of Chemistry and Physics: 58th Edition*. CRC Press, 1977.

[54] A Grill. *Thin solid Films*, 355-356:189–193, 1999.

[55] G Guastalla *et al.* *Physical Review Letters*, 110:172501, 2013.

[56] B Kindler *et al.* *Nuclear Instruments and Methods A*, 480:160–165, 2002.

[57] H Geissel *et al.* *Nuclear Instruments and Methods B*, 70:286–297, 1992.

[58] http://www-w2k.gsi.de/frs/technical/FRSsetup/detectors/music.asp.

[59] B Voss *et al.* *Nuclear Instruments and Methods A*, 364:150–158, 1995.

[60] R Janik *et al.* *Nuclear Instruments and Methods A*, 640:54–57, 2011.

[61] J Kurcewicz *et al.* *Physics Letters B*, 717:371–375, 2012.

[62] A Wendt. *Isospin Symmetry in the sd Shell: Coulomb Excitation of 33-Ar at Relativistic Energies and the new Lund-York-Cologne-Calorimeter*. PhD thesis, University of Cologne, 2012.

[63] O B Tarasov and D Bazin. *Nuclear Instruments and Methods B*, 266:4657–4664, 2008.

[64] J Taprogge. *First In-Beam Measurements with the dE-E-ToF LYCCA-Array at Relativistic Energies*. Master's thesis, University of Cologne, 2011.

[65] R Hoischen *et al.* *Nuclear Instruments and Methods A*, 654:354–360, 2011.

[66] http://www.detectors.saint-gobain.com/Plastic-Scintillator.aspx.

[67] ProPower. *ProPower RG-316 Coaxial Cable Data Sheet*. http://uk.farnell.com/pro-power/rg316/cable-coax-rg316-100m/dp/2064897.